Thesis MSc Mechanical Engineering

Differences in corrosion behaviour of cunifer welds

Combined with the protective properties of SDMC treatment

Ruitenberg, Annemarie

Abstract

Copper-nickel alloys are used for pipe systems that come into contact with seawater. These alloys are known under the group name cunifer alloys. In this research cunifer alloy CuNi10Fe (with 10 percent nickel) was investigated. The weld filler was a cunifer alloy with 30 percent nickel (CuNi30Fe). While generally there should be little corrosion problems, some will occur. In this research more information was acquired about the corrosion properties of a copper-nickel alloy used by Damen Schelde Naval Shipbuilding in the case of welding. The corrosion properties were investigated in different zones over the weld, i.e. the weld zone, heat affected zone, and base material. The differences in terms of corrosion performance between welding with backing gas and without backing gas were studied. The alloy can be protected against corrosion by a self-assembling monolayer of sodium diethyldithiocarbamate. The influence on the corrosion properties of this layer was also investigated. Potentiodynamic measurements, surface analysis and Kelvin probe measurements were used. The unprotected weld zone of a weld welded without backing gas resulted in a significantly higher corrosion rate in the sulphide containing solution. Welding without backing gas caused a porous surface to form on the inside of the pipes. This is not beneficial for the corrosion properties on the long run. The protection with sodium diethyldithiocarbamate decreased the corrosion rate to levels also obtained in the solution without sulphides for the samples welded without backing gas.

2

Summary

<u>SCOPE</u>

Copper-nickel alloys are used in seawater containing pipe systems of ships made by Damen Schelde Naval Shipbuilding (DSNS). These alloys are known under the group name cunifer alloys. In this research welds in cunifer alloy CuNi10Fe (with 10 percent nickel) were investigated. The weld filler was a cunifer alloy with 30 percent nickel (CuNi30Fe). The influence of welding without backing gas was researched, as well as the influence of a sodium diethyldithiocarbamate (SDMC) coating.

<u>EXPERIMENTAL DETAILS</u>

CuNi10Fe pipe segments were welded together with CuNi30Fe weld filler using gas tungsten arc welding. Half of the pipes were welded using argon backing gas; the other half was welded without backing gas. The pipes were then cut into quarters after which half of the samples were treated with SDMC.

Samples were taken to investigate the microstructure over the cross section of the weld and surrounding area of the samples welded with and without backing gas. The samples were etched and investigated under an optical microscope to determine the grain areas and microstructure over the weld. Before etching these samples were placed in a scanning electron microscope (SEM) and the composition was determined using Energy Dispersive Spectroscopy (EDS).

The potential of the surface layer was investigated using a Scanning Kelvin Probe (SKP). For this experiment samples were cut from pipe segments welded with and without backing gas, and protected and unprotected by SDMC. The SKP measurements were taken over the surface from the centre of the weld to the base material. Up to 40 mm away from the weld a visual heat affected zone (HAZ) could be seen for all pipe segments.

From the pipe segments also samples were taken to be tested by immersion in electrolyte. Two types of electrolyte were used. The first was demi-water with 3.4 wt% NaCl dissolved in it. The second one was the same but contained also 1200 mg sulphides. Samples were placed in the solutions and regularly photographed.

Electrochemical polarization tests were used to determine the current density differences between the different zones. Measurements were taken from the base metal, the visual HAZ and the weld zone, as well as measurements over all three zones together. A calomel reference electrode and graphite counter electrode were used in all measurements. Polarization started at -0.5 V below the measured OCP with a scan rate of 0.1 mV per second. To determine the behaviour of the passive layer polarization continued up to 0.4 V vs SCE. Again two types of electrolyte were used of the same composition as for the immersion tests.

<u>RESULTS</u>

Visually welds without backing gas had a porous surface with black burn residue. Complete penetration was not always achieved. Welds with backing gas showed a regular surface with a slight metallic shine. After the application of SDMC the surface turned dark brown, but the treatment was easily damaged by scratching or grinding.

The microstructure of the HAZ and base material showed a consistent grain area distribution and twinning bands, such as often found in copper containing alloys. The grain area distribution plots are

similar for the HAZ and base areas, with an exception of one sample. The welds both show a cellular-dendritic structure with segregation in the top layer of copper and nickel rich areas.

Figure 1 displays the SKP measurements of the surface potential from the centre of the weld (left in the graph) to the base material (right in the graph). Differences were observed in the Volta potential depending on the surface and the sample. The sample welded with backing gas, without SDMC protection (B, red line in the graph) displays a more or less constant surface potential over the length of the specimen. Welded without backing gas (NB, orange) the sample shows higher potentials which gradually changes to more negative potentials towards the base material. Adding the treatment (BS, dark blue and NBS, light blue) also led to a change in the surface potential. The surface potential for both treated samples changes to more negative potentials, until it reaches the same value (-150 to -200 mV) as for the B sample after about 45 mm. The visual HAZ was present up to 40 mm away from the centre of the weld. The untreated sample NB eventually also declined to the same value as found for the other three samples.

Immersion tests were performed in 3.4 wt% NaCl and in sulphide containing 3.4 wt% NaCl. For the samples in 3.4 wt% NaCl differences can be seen in corrosion thickness for the different zones. For the samples welded with backing gas, unprotected by SDMC, the HAZ exhibited a thick corrosion layer flanked by a zone with almost no visual corrosion products. For both samples protected with SDMC orange spots appeared in the HAZ. The orange spots adhered well to the surface when scratched. In the immersion tests where the samples were entered into sulphide containing 3.4 wt% NaCl corrosion products started to appear after 2 days of immersion. The electrolyte wherein the samples welded without backing gas were present turned green already after two days. This is an indication of dissolved corrosion products. A metallic shine appeared on all samples, especially in the HAZ.

The electrochemical polarization curves showed a passivation potential of 0 V vs SCE. Up to 0.4 V vs SCE the passive layer did not break. On samples in sulphide containing 3.4 wt% NaCl the passive layer still showed an increase in current density, indicating a less protective passive layer. For all
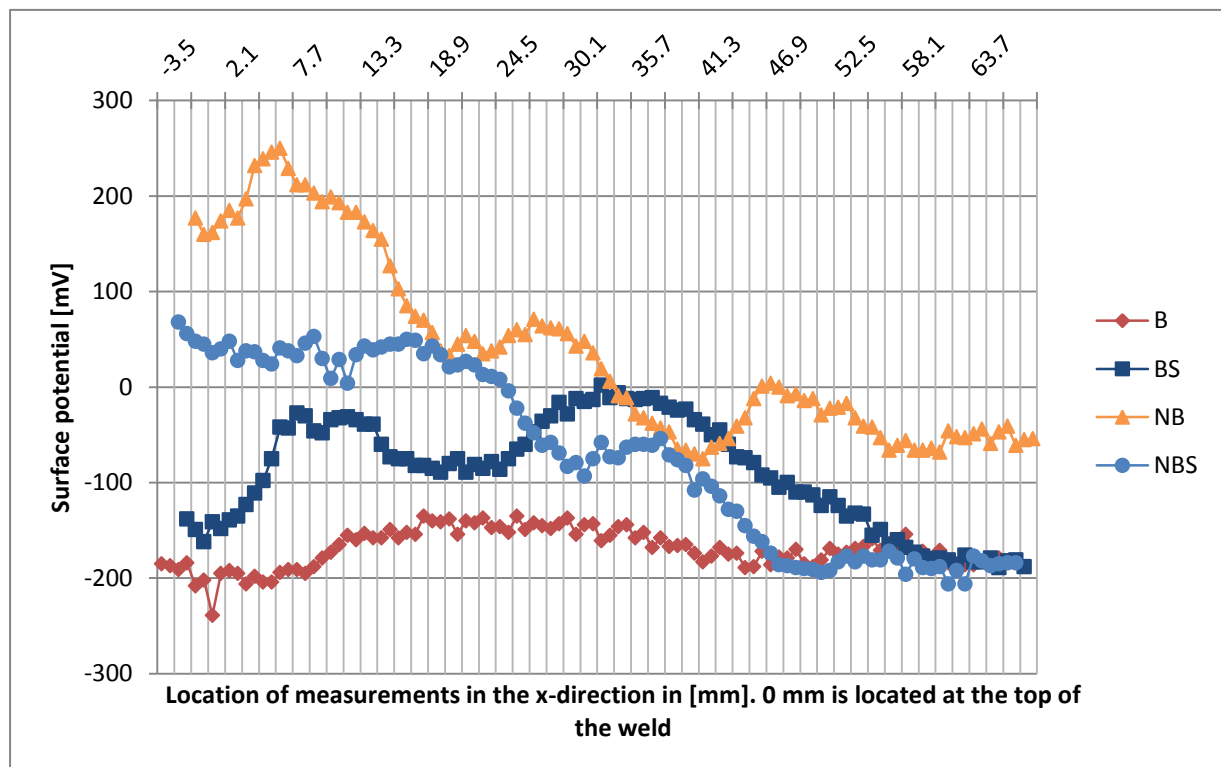

Figure 1: Surface potential of the four different potentials from the weld area to the base material. B is the sample welded with backing gas, without SDMC. BS has the SDMC treatment. NB is the sample welded without backing gas, without SDMC. NBS is also welded without backing gas but also has had the SDMC treatment. All samples eventually exhibit the same potential in the base material (-150 to -200 mV). The visual HAZ was present up to 40 mm from the centre of the weld.

samples the E_{corr} was measured between -0.18 and -0.27 V vs SCE. The abbreviations used for the different zones are explained in Table 1. The average current densities (i_{corr}) of the different zones tested in 3.4 wt% NaCl are shown in Figure 2. Overall it can be observed that from base material to weld the current density increases. Differences between the four types of samples are not significant.

Table 1: List of experiment designations for the polarization tests

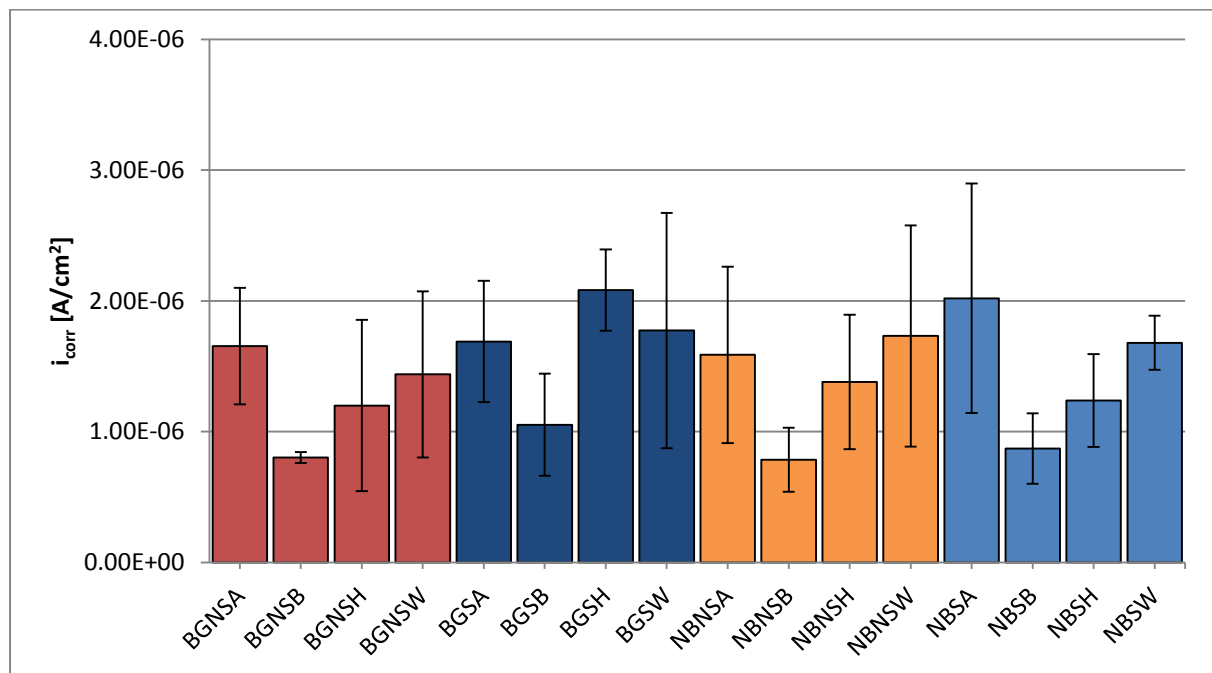|	Backing gas/No backing gas	Treatment	Region
BGNSA	Backing gas	No SDMC	Whole region
BGNSB	Backing gas	No SDMC	Base material
BGNSH	Backing gas	No SDMC	HAZ
BGNSW	Backing gas	No SDMC	Weld zone
BGSA	Backing gas	SDMC	Whole region
BGSB	Backing gas	SDMC	Base material
BGSH	Backing gas	SDMC	HAZ
BGSW	Backing gas	SDMC	Weld zone
NBNSA	No backing gas	No SDMC	Whole region
NBNSB	No backing gas	No SDMC	Base material
NBNSH	No backing gas	No SDMC	HAZ
NBNSW	No backing gas	No SDMC	Weld zone
NBSA	No backing gas	SDMC	Whole region
NBSB	No backing gas	SDMC	Base material
NBSH	No backing gas	SDMC	HAZ
NBSW	No backing gas	SDMC	Weld zone
BGNSP	Backing gas	No SDMC	Polished
NBNSP	No backing gas	No SDMC	Polished

Figure 2: i_{corr} values per experiment type in 3.4 wt% NaCl. The values are the average of four repetitions over different pipe segments with the standard deviation shown in black bars. The current density increases from base material to weld, but significant differences between the different kind of samples were not found.

Differences were found when comparing the results of unpolished, uncleaned samples with freshly polished and cleaned samples which are shown in Figure 3. Polished samples exhibited a higher current density for the same regions compared to the unpolished samples (red dots). As with the results from the surface potential measurements this indicates that the surface layer plays a big role in the corrosion process. This emphasises the importance of testing the samples with a surface condition as close as possible to the real conditions.
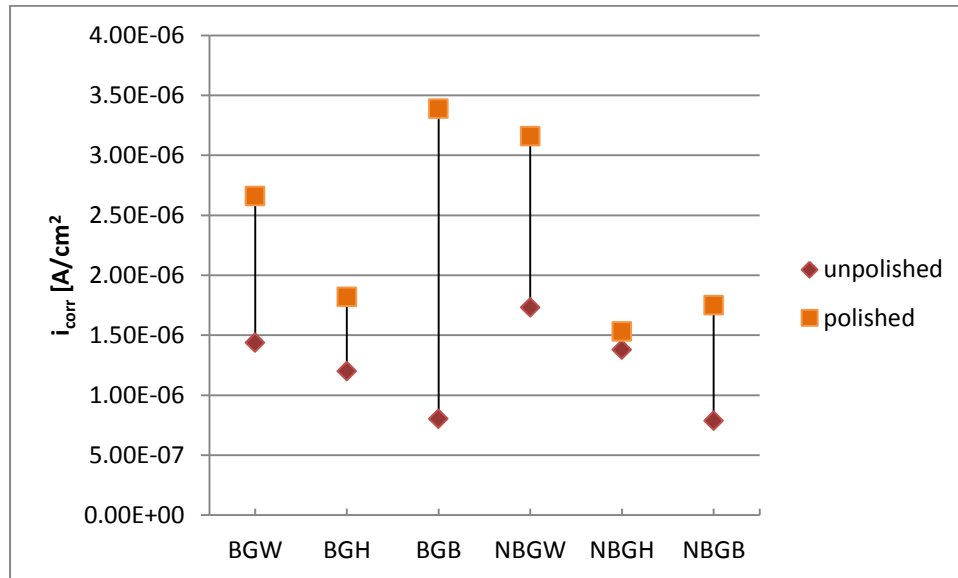
Figure 3: i$_{corr}$ values compared between unpolished and polished samples. The polished samples exhibited higher corrosion rates.

The results for the samples tested in sulphide containing 3.4 wt% NaCl are shown in Figure 4. The current densities for the samples welded without backing gas, and without SDMC protection (orange in the graph) show current densities which are an order of magnitude higher than for the other samples. The base material has a low current density (average of 7.11×10^{-7} A/cm^2), which is in the same range as for the other samples.
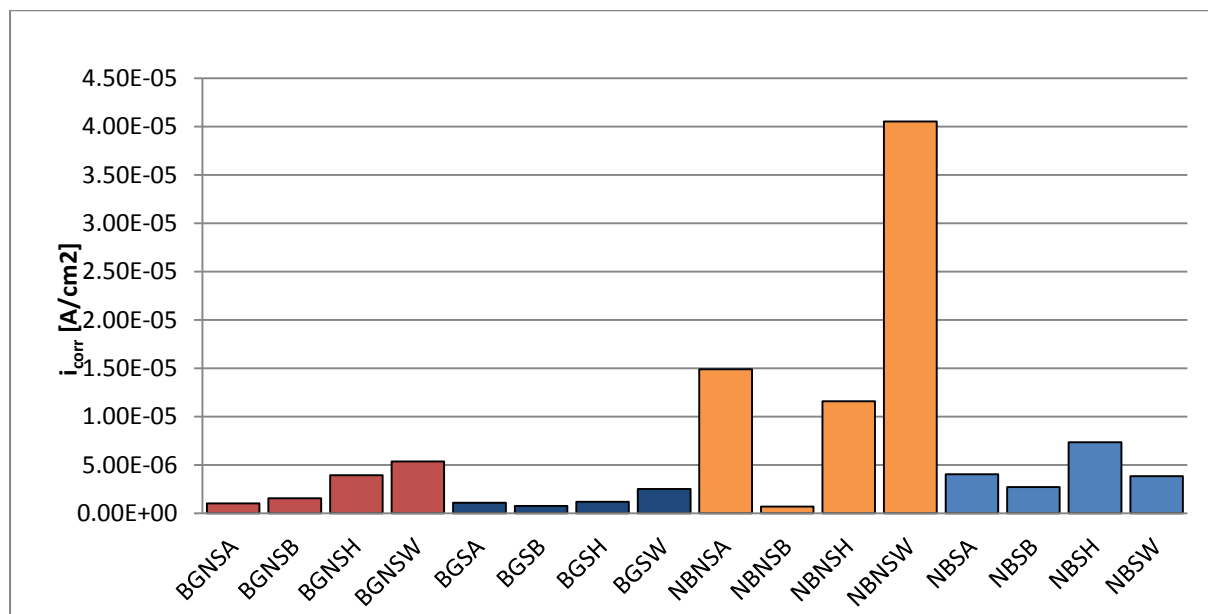

Figure 4: i$_{corr}$ values per experiment type in sulphide containing 3.4 wt% NaCl. The values are the average of four repetitions over different pipe segments. The sample welded without backing gas (orange) exhibits the highest current density; however with SDMC protection this high current density is not seen.

DISCUSSION

The found microstructures and grain areas do not explain the differences found in the current densities over the different zones. Large differences however are found in the surface potentials where the potential is variable and higher in the visual HAZ region (the first 40 mm from the centre of the weld) for the protected samples and the sample welded without backing gas. In the base material the surface potential for all samples decreases to the same value eventually. The change in surface potential for the unprotected sample welded without backing gas can be explained by the oxidation of the surface during welding. This surface was not protected by a shielding gas, but reached high temperatures. The differences in the surface potential led to the decision to not polish or clean the surface so the most realistic current density could be measured.

The current densities for the samples in 3.4 wt% NaCl did not differ significantly for the different samples. It can be seen that the lowest current densities are found for the base material polarization only, while the highest can be found for the weld metal. The overall current density is comparable to this weld zone current density. The highest corrosion rate in the weld metal is due to the difference in material, with the weld being CuNi30Fe and the base material CuNi10Fe. CuNi30Fe without a protective corrosion layer corrodes faster when no sulphides are present than CuNi10Fe (Powell & Michels, 2000).

For the tests with sulphide containing 3.4 wt% NaCl differences can be found in the different zones and the different samples. The sample welded without backing gas exhibits the highest current density, most likely due to its irregular surface. The sample protected by SDMC, but also welded without backing gas, exhibits lower current densities, indicating that the protection with SDMC lowers the corrosion rate in sulphide containing electrolyte. It therefore provides an efficient protection against corrosion.

Differences in corrosion rate occur over time and between artificial and real seawater as well as for standing and moving electrolyte. The Cu_2O and $Cu_2Cl(OH)_3$ corrosion layers formed in the immersion tests is likely to form, however different oxides may form in time if other elements are present in the real solution.

CONCLUSIONS

Welding without backing gas in the presence of sulphide containing water is showed to have significantly higher corrosion rates compared to the welds welded with backing gas. The crevices and pores present on the weld surface can harbour sulphide generating bacteria which increases the corrosion rate further.

The protective layer formed on cunifer alloys consists first of a layer of Cu_2O which in natural seawater grows for up to 3 months. With sulphides present this layer is less protective, which causes the higher corrosion rates to continue to be present during the exposure to sulphide containing water.

The sodium diethyldithiocarbamate forms a protective layer on the cunifer alloy that protects against corrosion by restricting access to the metal surface. The layer is fragile, but it is shown that in sulphide containing water the treatment reduces the corrosion rate.

Scope

Copper-nickel alloys are often used for seawater pipe systems. These alloys are generally known under the group name cunifer alloys, in this research cunifer alloys will be used to denote copper-nickel alloys with added iron. The systems cunifer alloys are used for include cooling systems with continuous flow, but also firefighting systems where the water stands still for prolonged periods of time. Despite their normally excellent behaviour in seawater environments problems do occur from time to time. Common problems are erosion corrosion due to high flow velocities and accelerated attack due to sulphides. Damen Schelde Naval Shipbuilding (DSNS) uses a cunifer alloy with 10 percent nickel, designated here as CuNi10Fe for the seawater pipe systems. These pipe systems are protected against corrosion using a sodium diethyldithiocarbamate (SDMC) coating applied by VECOM. Parts of the pipe system are welded together, mostly in the pipe shop, using argon backing gas. In some cases it can occur that a weld that needs to be made on the vessel (field weld) is welded without backing gas. It is expected that this welding without backing gas influences the corrosion behaviour. Backing gas is applied to prevent oxidation of the surface. This research aims to clarify the consequences of welding without backing gas on the corrosion characteristics. Another objective is to evaluate the role sodium diethyldithiocarbamate as corrosion inhibitor, also in combination with welds in cunifer alloys.

Chapter 1 includes background information about welding and corrosion of cunifer alloys. To obtain more information about the consequences of welding without backing gas and applying the SDMC treatment the electrochemical characterization of samples welded with and without backing gas (and with and without SDMC treatment) was performed. The methods used are described in chapter 2, and the results are shown in chapter 3. Surface analysis was performed to be able to explain differences in corrosion characteristics and also shown in chapter 3. The results are discussed in chapter 4, which discusses the influence of welding without backing gas and the consequences of applying a SDMC coating. This is followed by the conclusions of this study.

Table of Contents

11

Chapter 1: Background

1.1 Cunifer alloys

Cunifer alloys consist mainly of copper with added nickel (commonly 10 or 30 percent) and some iron (commonly between 1 and 2 percent). This combination led to the group-name cunifer. There are different names for this material in research but here CuNi10Fe will be used when material with the nominal composition from KME (Osna10) as shown in Table 2 is meant. There are other standards that give different limitations for the composition of CuNi10Fe as given in Table 2, but due to earlier problems with these composition ranges at Damen Schelde Naval Shipbuilding (DSNS) only KME Osna10 is currently used. These materials show high resistance to corrosion by seawater and therefore are commonly used in seawater pipes for cooling, firefighting systems and bilge water pipes in ships. Copper and nickel have atomic radii that closely match and similar lattice parameters (Schleich & Powell, 2007). Copper and nickel atoms only differ about 2.5% in volume and both exhibit a face-centred cubic structure (ASM International, 2004). They are completely soluble in solid and liquid state, meaning that all cunifer alloys have a single-phase structure as can be seen in Figure 5 (Copper Development Association, 1964). Figure 5 shows the phase diagram of copper and nickel, with the percentage of nickel in the alloy on the x-axis. The region below the liquidus, at lower temperatures, shows in what phases the alloy will solidify. This figure shows that in the case of cunifer alloys there is only one phase structure, independent of the percentage of nickel in the alloy.

The high amount of copper in the alloy gives it its anti-fouling properties since marine fouling generally does not reside well in the presence of copper ions (Gilbert, 1978). The addition of nickel improves strength and durability. It increases the resistance against corrosion, erosion and cavitation
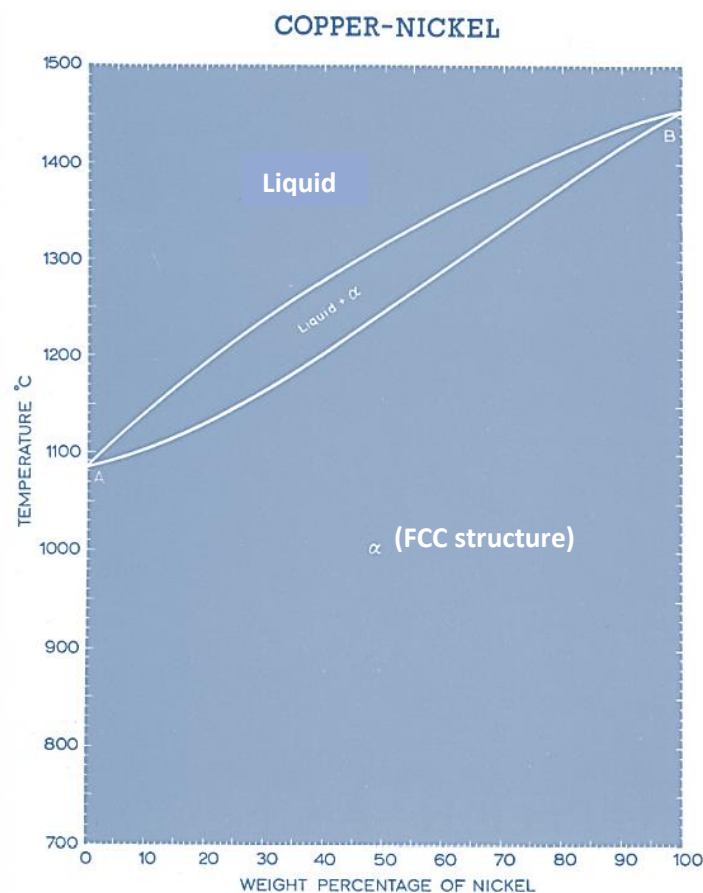
Figure 5: Phase diagram of copper and nickel. All combinations give a single phase structure. A wide solidification range can be seen between the liquid and the solid material. (Copper Development Association, 1964)

(Copper Development Association, 1982). Cunifer alloys are not susceptible to chloride or sulphide stress corrosion cracking or hydrogen or ammonia cracking.

Cunifer alloys have good uniform and localised corrosion resistances, depended on the addition of small amounts of Fe. Especially in combination with seawater the corrosion resistance is high (Popplewell, Hart, & Ford, 1973). They concluded that iron in solution doped the Cu_2O oxide film with Fe ions that resulted in improved corrosion resistance. Collected data from the British Non-Ferrous Metals Research Association laboratories and several research facilities in the USA revealed the optimum iron content in relation to corrosion to be between 1 and 2% (Parvizi, Aladjem, & Castle, 1988). Nickel increases the corrosion resistance of copper even more when combined with iron (North & Pryor, 1970).

Table 2: Comparison of chemical composition as specified by various standards for tubing material. DSNS orders according to KME standard. (Deutsches Kupferinstitut, 2005) (Schleich & Powell, 2007) [wt%]

	Cu	Ni	Fe	Mn	C	Co	P	Pb	S	Sn	Zn
DIN EN 2.0872	86.0-89.7	9.0-11.0	1.0-2.0	0.5-1.0	<0.05	<0.1	<0.02	<0.02	<0.05	<0.03	<0.5
DIN EN 2.1972	REM	9.0-11.0	1.5-1.8	0.5-1	<0.05		<0.02	<0.01	<0.005		<0.05
ISO CuNi10Fe1MN	REM	9.0-11.0	1.0-2.0	0.5-1.0	<0.05	<0.05	<0.02	<0.02	<0.02	<0.03	<0.5
KME Osna10	REM	10.0-11.0	1.50-1.80	0.6-1.0	<0.02	<0.1	<0.02	<0.01	<0.005	<0.03	<0.05

In this research two cunifer alloys are of importance. CuNi10Fe, the pipe material and CuNi30Fe, used for the welds. Where CuNi10Fe contains around 10 wt% Ni, the weld filler material contains 30 wt% Ni. The solubility limit for iron is higher for CuNi10Fe than for CuNi30Fe (Kear, Barker, Stokes, & Walsh, 2004). According to research at LaQue Corrosion Services CuNi10Fe performs better in quiet seawater but CuNi30Fe performs better when seawater is flowing. However after 14 years CuNi10Fe corroded less than CuNi30Fe in flowing seawater, but both corrosion rates had then already dropped tenfold due to the creation of a protective oxide layer (Powell & Michels, 2000). CuNi30Fe has higher potentials than CuNi10Fe for the first few days of immersion in aerated 3% sodium chloride solution (Giuliani & Bombara, 1970). After about 10 days the potential suddenly dropped and became lower than the potential obtained for CuNi10Fe.

Cunifer alloys have limited resistance against erosion due to rapid flowing seawater and cavitation. This area has been researched extensively to acquire design limits. Research indicated that the methods of erosion in saline water are complex and seemed more dependent on the Reynolds Number than only pure on mechanical erosion (Hodgkiess & Vassiliou, 2005). They argue that design limits of around 2-4 m/s for cunifer alloys commonly used are conservative and that there is evidence that higher velocities of 12-15 m/s are acceptable for limited periods of time. Therefore the design limits are usually maintained at a maximum of 3.5 m/s. Higher flow velocities are often also unwanted because of the increased power costs since larger capacity pumps etc. are needed (Parvizi, Aladjem, & Castle, 1988) while excessive root penetrations from welds and sudden changes of direction increase the probability of erosion-corrosion (Schleich & Powell, 2007). On the other end a minimum flow velocity of 1 m/s is desired in flowing seawater pipe systems to avoid sediment build up and the growth of sulphide producing bacteria.

1.2 Welding of cunifer alloys

Cunifer alloys are commonly welded using gas tungsten arc welding (GTAW). This process is schematically shown in Figure 6. The process is named after the tungsten electrode which does not melt into the weld pool. The electrode can be pure tungsten, but more commonly additions of 1 to 4% of thorium oxide are used.
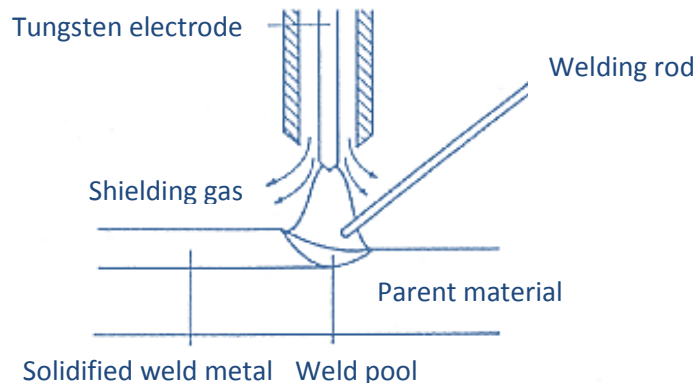

Figure 6: schematic drawing of GTAW process (Ouden & Hermans, 2009). The tungsten electrode can be seen to make an arc between the parent material and the electrode. The welding rod is used to add weld metal to the weld pool.

Lately this is however replaced by lanthanum oxide or cerium oxide because of the radioactivity of thorium. The arc forms between this electrode and the workpiece. A power source connected to the electrode is managed by a foot pedal that controls the current. Current control prevents drawing high currents in the case of short-circuiting (resulting in a lot of generated heat). The weld filler is added by a separate weld rod by hand. The process therefore requires coordination between both the electrode and the welding rod to achieve a weld. Automation of the process is normally not recommended. This is due to a lack of deoxidants in the composition of the material which increase the risk of porosity in the welds. Welding by hand offers continues control and adjustments when necessary are easily made (TWI global). The electrode should never touch the weld metal during welding to prevent contamination. The separate weld rod material is UTP A 387 filler material. Direct current (DC) is used with currents between 90-150 A and potentials between 13 and 16 V. The electrode is usually connected to the negative pole since two-thirds of the heat is present at the anode (workpiece in that case) and only one-third at the cathode (electrode). This will help to prevent the tungsten electrode to melt and contaminate the workpiece. The heat input will then be between 0.42 and 1.73 kJ/mm with a propagation speed between 5 and 10 cm/min (Bekkers, 2009). UTP A 387 has a composition as shown in Table 3. The nickel content of the weld filler is approx. 30 percent, higher than in the base metal (approx. 10%). This will ensure welds with an increase in the mechanical properties, but differences in the melting temperatures of the base metal and filler could lead to cracking when the material is welded under stress. The melting range of this alloy is between 1180 and 1240 ^{0}C (UTP, 2010), the melting range of CuNi10Fe is between 1100 and 1145 ^{0}C. These temperatures are close together so problems with cracking due to different melting temperatures are not expected.

The shielding gas prevents oxygen to contaminate the weld, but however effective it is, it is still necessary to add deoxidants with a high affinity for oxygen. One such a deoxidant is titanium. It is therefore added to the filler material as can be seen in Table 3. Nitrogen also causes porosities in the weld, therefore it is recommended to use argon as shielding and backing gas for copper and copper alloys such as cunifer alloys (TWI global, 1991).

14

Table 3: Chemical analysis from deposited material (%) (UTP, 2010)

C	Mn	Ni	Cu	Ti	Fe
<0.05	0.8	30.0	Balance	<0.05	0.6

It is however possible to weld using nitrogen as shielding gas, but the arc length is much longer and need to be maintained at 12 mm. Fewer than that will result in craters and turbulence, and thus porosity, in the weld, more will extinguish the arc. The heat input for GTAW with nitrogen is also higher, up to about three to four times as much as for argon in the case of pure copper.
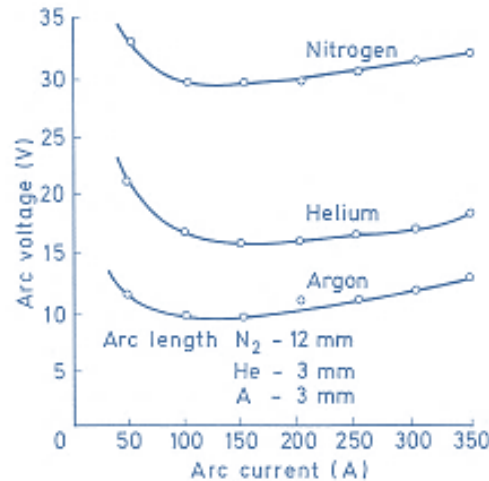

Figure 7: Arc characteristics of argon; helium and nitrogen shielded GTAW processes for pure copper (Dawson, 1973). Welding with nitrogen requires a long arc length of about 12 mm and results in a higher heat input compared to argon or helium. In this research argon is used as shielding and backing gas.

The differences in the resulting arc voltages for nitrogen, argon and helium are shown in Figure 7, depending on the arc current. The heat input is linearly depended on both the arc voltage and the arc current. The heat input for alloys is generally lower, but the difference between argon and nitrogen remains. Higher arc voltages give also higher heat inputs, if speed and arc current remain the same. Gas flow rates using nitrogen need to be considerably higher than in argon to accommodate the longer arc length (Dawson, 1973). The shielding and backing gas used in this research is therefore argon gas.

A weld leads to differences in composition and microstructure in the material due to the cycle of heating and cooling as a result of the welding process and adding filler material. A weld area can be divided in a fusion zone with a cast-like dendritic structure and a small unmixed zone where the base material melted but solidified quickly; a heat-affected zone (HAZ) where the base material has experienced temperatures high enough to produce microstructural changes, but where the material was not melted; and the unaffected base metal, an area where the metal is metallurgically unchanged (Davis, 2006).
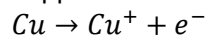
Residual stresses in copper containing alloys can lead to higher corrosion rates due to microcracking of the protective corrosion layer (Drach, et al., 2013). Segregation of elements can lead to differences in corrosion products. These segregations can occur as a result of welding, where elements are pushed away from the solidifying metal (Savage, Nippes, & Miller, 1976). Nickel rich areas such as can be found in weld areas are covered with Cu_2O corrosion products that are not as attached as the layer is on copper rich areas. Especially in the presence of fluid flow this can expose fresh metal surface after the corrosion layer is stripped away (Little, Wagner, & Jacobus, 1988). A field test of CuNi10Fe showed pits on areas richer in Fe and Ni after 8 years of immersion (Drach, et al., 2013).

Due to practical problems it is sometimes not possible to weld with backing gas. This could cause a different structure to form at the inside surface of the pipe since cunifer alloys are prone to oxidation (Lathi & Lukkari, 2002). There are indications that it may have an influence on the corrosion properties of the CuNi10Fe pipe. Therefore in this research the corrosion properties of welds in CuNi10Fe are studied when welded without backing gas.
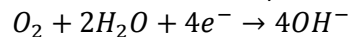
1.3 Corrosion of cunifer alloys

Corrosion is usually defined as an attack on a metallic material by a reaction with its environment. In this case wet corrosion in seawater will be investigated. Wet corrosion refers to the metal corrosion that takes place in a wet/aqueous environment (Zarras & Stenger-Smith, 2014). The corrosion process is an electrochemical reaction consisting of two processes namely an oxidation reaction and a reduction reaction. When a metal comes into contact with a corrosive environment the metal will start to oxidize.

The anodic (oxidation) general reaction of copper will be:
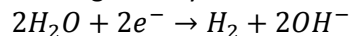$$Cu \rightarrow Cu^+ + e^-$$
In this reaction the metal forms thus an ion and electrons are released. The cathodic (reduction) reactions that can occur in neutral solutions are:
Reduction of dissolved oxygen (common in aerated water):
$$O_2 + 2H_2O + 4e^- \rightarrow 4OH^-$$
When there is no oxygen the reaction that generally occurs:
$$2H_2O + 2e^- \rightarrow H_2 + 2OH^-$$

In the reduction reaction the electrons need to come into contact with the oxygen (Ashby, Shercliff, & Cebon, 2014). This process is depicted in Figure 8 where the metal, consisting of Cu and Ni is shown right with a dense Cu_2O layer on top of it (doped with Ni and Fe ions (North & Pryor, 1970)). The aqueous solution is shown in the right, where among the seawater also oxygen can be found. The metal surface here is called the electrode; the seawater, that is ionically conductive, is called the electrolyte.

This Cu_2O layer incorporates nickel and iron which decreases the ionic conductivity (Ni^{2+} and Fe^{2+} ion incorporation in the corrosion layer creates more positive holes) thus making it more difficult for the electrons to diffuse out (Parvizi, Aladjem, & Castle, 1988). The structure of pure copper oxide is a cubic structure of which the unit cell is shown in Figure 9 in which four copper atoms are shown and two oxygen atoms. The Pilling-Bedworth ratio for Cu with its oxide is between 1.64-1.71, indicating outward growth of the oxide. The oxide thus forms on top of the metal surface (Evans, 1981), (Birks, Meijer, & Petit, 2006). The Cu^+ can be replaced by Ni^{2+}, creating a positive hole in the structure. On top of the Cu2O layer different corrosion products can form, depending on the solution the CuNi10Fe is in (Syrret, 1981). Kinetic investigations showed that ions and electrons such as Cu^+, Ni^{++} and Fe^{++} form at the alloy/oxide interface after which they migrate through the Cu_2O layer (Kato, Ateya, Castle, & Pickering, 1980). At the top of this layer the reduction of oxide occurs and the cations either dissolve in the seawater or form the porous outer oxide layer.
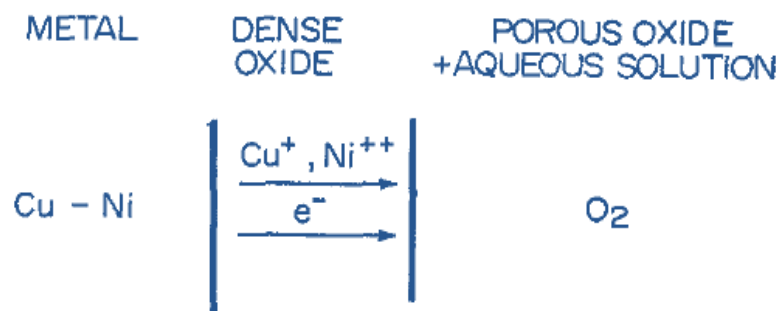
Figure 9: Schematic drawing of the transport process in the reaction product of cunifer alloys during open-circuit corrosion (Kato, Ateya, Castle, & Pickering, 1980). The electrons from the oxidation reaction of copper have to transport through the dense oxide layer to the oxygen in the electrolyte.
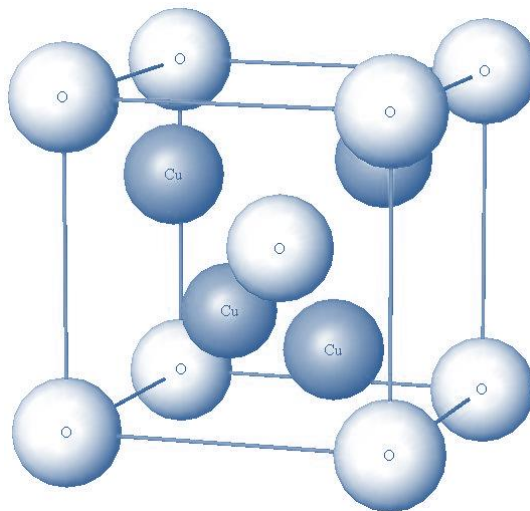
Figure 8: Cu2O structure (space group Pn3m) (OHBA laboratory, 2014). Oxide atoms can be seen on the corners of the unit cell, with copper atoms in between. The unit cell consists of 4 copper atoms and 2 oxygen atoms.

After polarization tests on CuNi30Fe a film that was mainly dark green and most likely consisted of $Cu_2Cl(OH)_3$ was seen (Wood, Hutton, & Schiffrin, 1990). Data was collected that was obtained from 39 exposure sites (Krätschmer, Odnevall Wallinder, & Leygraf, 2002). In all sites the corrosion layer consisted mostly of Cu_2O. $Cu_2Cl(OH)_3$ was commonly found on copper kept in chloride-rich environments. They proposed that $Cu_2Cl(OH)_3$ was formed from the dissolution of Cu_2O into copper ions that react with chloride ions, just as concluded in other research (on copper alloys) (Metikoš-Hukovic, Babic, & Škugor, 2011) (Wallinder, et al., 2014).

The Pourbaix diagram is used to determine the stable stages of the metal depending on the pH value. Such a diagram is valid for a certain temperature range and in the case of solutions also for a certain dissolved concentration. In the case of copper in chlorine solution (0.2 mol/l) and at the temperature of 25 ^{0}C the Pourbaix diagram is calculated (Beverskog & Puigdomenech, 1998). Their Pourbaix diagram is shown in Figure 10, at pH 7 a dotted line is drawn, the solutions used in this research are neutral solutions of pH 7. The concentration of chlorine used in this research is 3.4 gr/l of NaCl, which coincides with 0.058 mol/l of dissolved chlorine. This is thus lower than used in the diagram. For potentials above -0.2 V (SCE) (around -0.44 V (SHE)) the stable forms are then $CuCl_2^-$ and Cu_2O at higher pH values. The release of the soluble $CuCl_2^-$ will lead to an increase in the pH, especially close to the surface. An added reason is the reduction reaction in which H_2O converts to OH^-. Increase in the concentration of OH^- leads to a more alkaline solution. Here then it is expected

that Cu_2O forms and deposits on the surface. A Pourbaix diagram however does not say anything about the kinematics of the reactions, only which species form if the reaction occurs. An increase in temperature accelerates the corrosion rate (Wang, Beccaria, & G.Poggi, 1994), (Tuthill, Todd, & Oldfield, 1997). Another influence on the corrosion rate and corrosion products is the influence of dissolves sulphides.
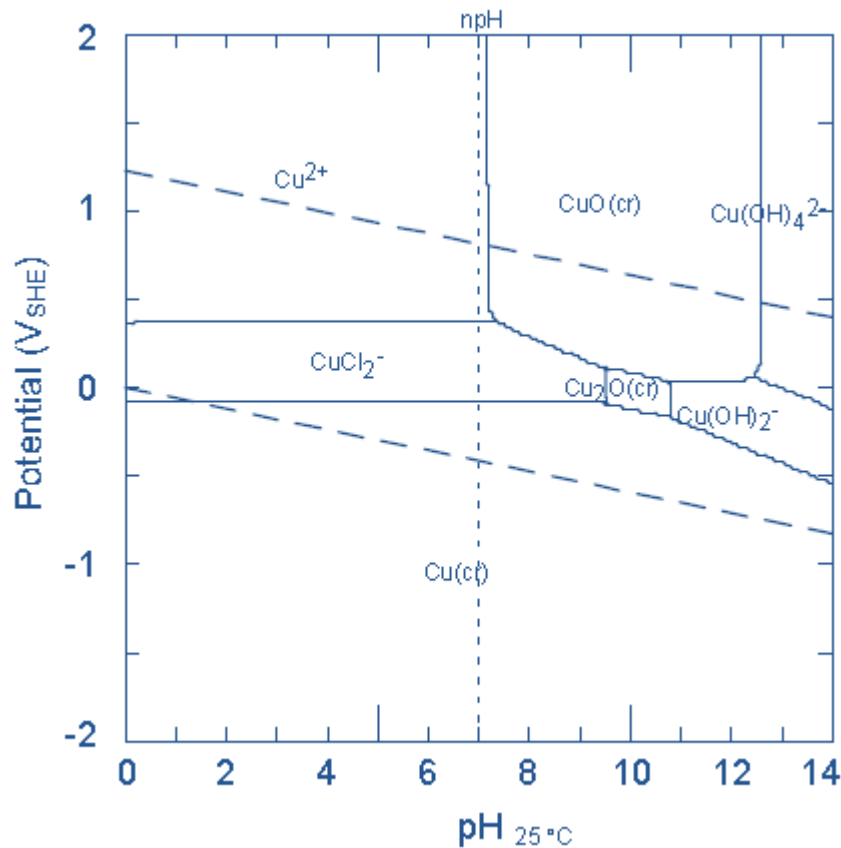

Figure 10: Pourbaix diagram for copper in chlorine containing water at 25 ^{0}C. A concentration of 0.2 mol/l of dissolved chlorine was used (Beverskog & Puigdomenech, 1998). At neutral pH $CuCl_2^-$ is the most stable phase, when the electrolyte at the metal surface becomes more alkaline Cu_2O will be most stable.

1.4 Influence of sulphides on the corrosion properties of cunifer alloys

Sulphides dissolved in the water accelerate the corrosion rate (Francis, Effect of pollutants on corrosion of copper alloys in sea water, 1985) (Eiselstein, Syrett, Wing, & Caligiuri, 1983). Sulphide contamination is identified as a corrosion enhancer in many researches. As stated by Rowlands failures of cunifer pipelines were found in sulphide contaminated seawater (Rowlands, 1965). These incidents also appeared in blind end pipes, giving reason to believe that failure due to impingement or erosion was not the case here. Sulphide can enter the seawater in many ways. Often it originates from rotting vegetation (Al-Haji & Reda, 1993) or from industrial/agricultural waste discharge in rivers that flow into the sea. Rivers meet the sea at harbours and combined with the stagnating water conditions often found in several areas in a harbour explain the commonly found sulphide contamination in harbour areas. Ships being build are present in harbour water for a prolonged amount of time.

Schrader investigated the effect of sulphides in seawater on CuNi10Fe (Schrader, 1982). He concluded that when present in the water the sulphide ions are incorporated in the corrosion film. The depth profiling showed correlation between sulphur and iron, suggesting that a big portion of

the sulphur present is in the form of ferrous sulphide. It is then postulated that this sulphide interferes with the formation of the protective layer, increasing the corrosion rate. In other research a corrosion mechanism where the formation of sulphides occurred through the reaction of copper and nickel ions to produce deposited Cu_2S and NiS was proposed (El Domaity & Alhajji, 1997). These are brittle, non-adherent corrosion products which offer no protection to the base material. The electrochemical tests performed however were over a relatively short period so no significant corrosion product layer could form.
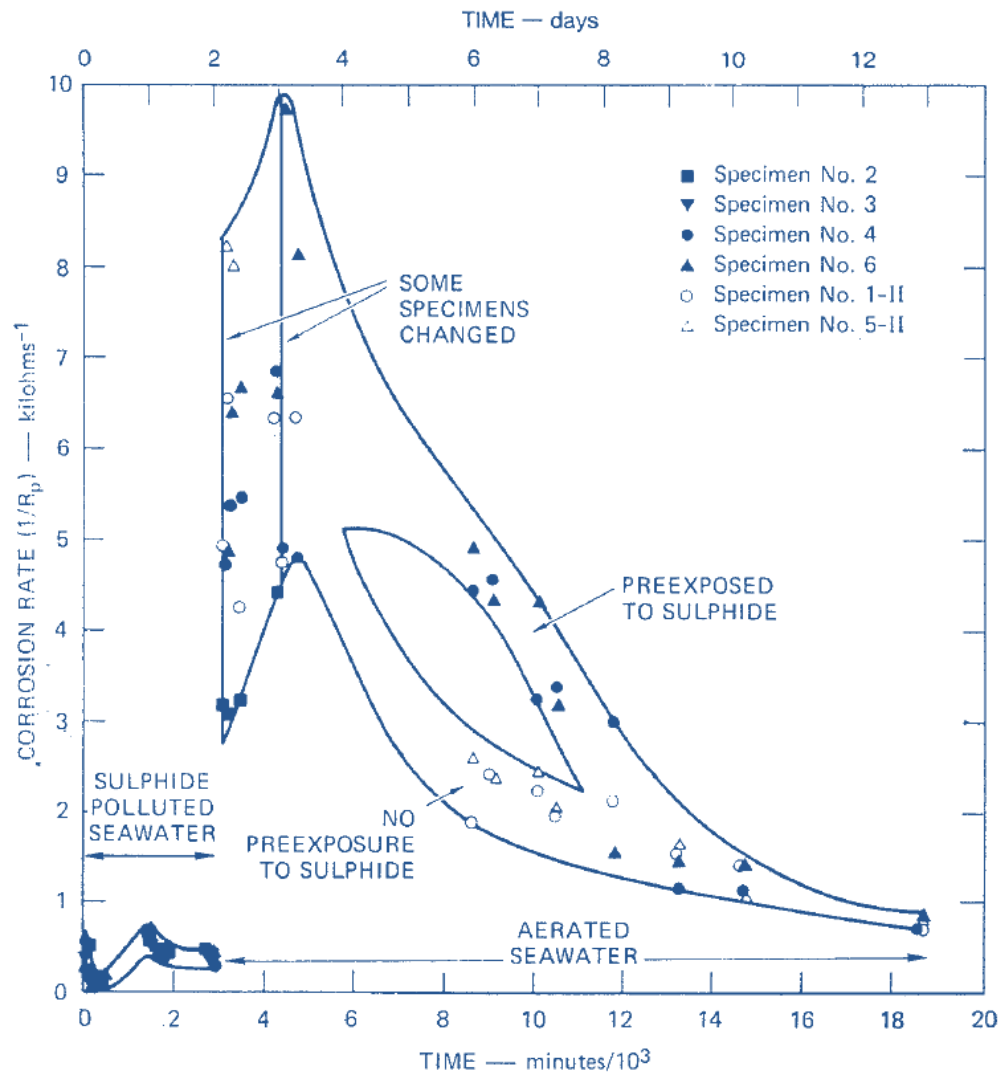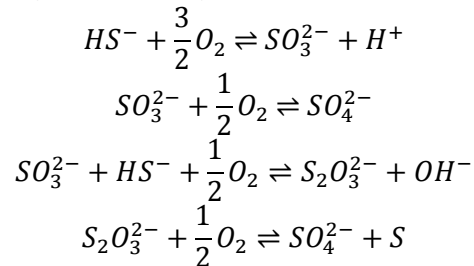
Figure 11: Corrosion rates for CuNi10Fe in flowing seawater that was de-aerated and sulphide polluted for 2 days; then aerated and unpolluted for the following 11 days (Syrret, 1981). CuNi10Fe first exposed to sulphide containing solutions exhibits higher corrosion rates in clean seawater afterwards compared to samples not pre-exposed to sulphide.

The exposure to sulphide polluted water results in a porous oxide layer instead of the protective Cu_2O that would form in clean seawater. When the material is next brought back into clean seawater, the protective Cu_2O layer will start to form again, but the relatively high corrosion rates are maintained for at least several days in the unpolluted water. The effect of oxygen and sulphide combination was researched (Syrret, 1981). The samples pre-exposed to sulphides exhibited higher corrosion rates in clean seawater than the samples that were not pre-exposed as can be seen in Figure 11. Here the corrosion rate is plotted against the time it is immersed in a solution. The samples pre-exposed to sulphides are shown with dark blue filled points while the samples that were not pre-exposed are shown with unfilled points. The difference between the samples in corrosion rate is most evident between 4000 and 10000 minutes (3 days to a week).

Often the pipe system will be present in contaminated waters. Measurements done in the harbour of Vlissingen show that 1200 mg/l SO_4^{2-} is present in the water (Scheldestromen, 2012). Concentrations found in literature vary widely. 0.41-1.6 g/m3 of HS⁻ was used in research (Eiselstein, Syrett, Wing, & Caligiuri, 1983), others however decided upon 0.01 g/m3 HS⁻ (Sanchez & Schiffrin, 1982). Already at this low concentration a negative effect on the corrosion rate was discovered (Gudas & Hack, 1979) and the same concentration was used in more research (Schrader, 1982). When entering a sulphide containing salt in water a series of reactions take place. As discussed by Millero the overall reactions are (Millero, 1986):

$$HS^- + \frac{3}{2}O_2 \rightleftharpoons SO_3^{2-} + H^+$$
$$SO_3^{2-} + \frac{1}{2}O_2 \rightleftharpoons SO_4^{2-}$$
$$SO_3^{2-} + HS^- + \frac{1}{2}O_2 \rightleftharpoons S_2O_3^{2-} + OH^-$$
$$S_2O_3^{2-} + \frac{1}{2}O_2 \rightleftharpoons SO_4^{2-} + S$$

These reactions link HS⁻ as used in literature to SO_4^{2-} as measured by water board Scheldestromen. For tests it is decided to use the contamination in Vlissingen as a guide for the amount of sulphides in the test solutions.

Both alloys are generally considered to be less susceptible to stress corrosion cracking (SCC) compared to other copper-based alloys, especially in seawater environments. However in ammonia, sulphide or nitrate environments cases of SCC are reported. In ammonia and sulphide environments an increase in Ni content increased the resistance against SCC (Agarwal & Bapat, 2009). SCC for CuNi10Fe in sulphide containing seawater within the range of 100-1000 ppm was reported (El Domaity & Alhajji, 1997). Earlier research by DSNS led to measurements made by the water board Scheldestromen. In the vicinity of the harbour in Vlissingen the concentration of sulphate is around 1200 ppm, which rapidly decreases closer to open sea. Above 1000 ppm Domaity and Alhajji indicated that the corrosion of CuNi10Fe is too fast for SCC to happen. SCC is not further investigated in this research, the focus lies on the influence of sulphides in concentrations as found in practice on the corrosion rates of the weld areas.

1.5 Corrosion protection of cunifer alloys

As stated before cunifer alloys do not perform as desired in regards to its corrosion properties when sulphides are present. To protect the material in case of sulphide contaminations several options are possible. Coatings are often applied. In the last several decades these coatings transformed from simple barriers against the environment to more specialized organic and inorganic coatings (Zarras & Stenger-Smith, 2014).

In pipe systems such as regarded in this research it is desired to apply a protection that can either withstand bending and welding of the pipe segments or a coating that assembles itself after the pipe system is installed on the vessel. Self-assembling coatings can be very thin and flexible. They produce very densely packed films that block electron transfer or the transport of corrosive species to the underlying metal (Zarras & Stenger-Smith, 2014). A self-assembled coating on cunifer alloys is sodium diethyldithiocarbamate (SDMC). Where other coatings are harmful or toxic to the environment derivatives of dithiocarbamate such as SDMC are preferred (Liao, et al., 2011).

Compounds containing a dithiocarbamate part form a bond with virtually all transition elements with at least two atoms (chelate) (Jian, et al., 1999). This is also the case for SDMC and copper which thus form such a chelate. The chemical adsorption on the surface of copper was researched by Liao et al. (Liao, et al., 2011). Both anodic and cathodic current densities decreased for SDMC protected

samples of copper. It is proposed that the protection method of SDMC works by inhibiting the leaching of Cu+ at the solid/liquid interface (Martinez & Metikos-Hukovic, 2006). The research by Liao et al. showed that the sulphur atoms are the main active sites that result in absorption on the copper surface (Liao, et al., 2011). The SDMC compound prevents the dissolution of copper and hinders cathodic oxygen reduction. Bonding takes place with the two sulphur atoms that are part of the molecule (Aljinovic, Gudic, & Smith, 2000). This is shown in Figure 12 (a). This is backed up by analysis of the surface which showed that the main active sites are the sulphur atoms, which result in absorption on the copper surface (Liao, et al., 2011).
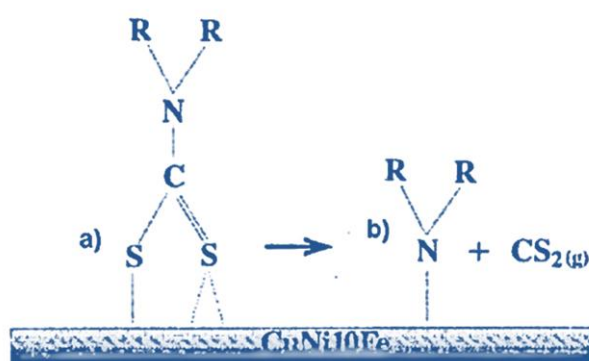

Figure 12: By Aljinovic et al. proposed protective layer structure (a) and decomposition of the SDMC molecule after anodic polarization at +100 mV (b) (Aljinovic, Gudic, & Smith, 2000). The structure forms a chelate with transition elements such as copper.

Adsorption of the organic SDMC molecule to the surface can be classified in different types of bonding depending on the type of forces that are exhibited. Physisorption is due to electrostatic attractive forces between ions or dipoles and the electrically charged surface of the metal. Chemisorption is due to the interaction between the unshared electron pairs (π electrons) and the metal to create a coordinate type of bond (covalent bond where both electrons come from the same atom) (Bentiss, et al., 2009). Sulphur as present in SDMC is a likely candidate for the latter type of adsorption. For a solution of different concentrations of SDMC (0.1 to 1 mmol L^{-1}) applied for 12 hours on a copper surface to create a self-assembled monolayer Liao et al. determined that the adsorption mechanism of SDMC to copper is typical chemisorption (Liao, et al., 2011).

SDMC is unstable and likely to decompose in acetone and alcohol (Gothelf, 2000). Rinsing with ethanol is therefore not advisable to prevent the dissolution of the SDMC layer, just as scratching or hard handling. The application process starts with a solution of SDMC entering into the pipe system where it will circulate and stand for 24 hours. This will lead to a brown/red layer on the inner side of the cunifer pipes where later seawater flows through (Jian, et al., 1999). This layer will protect the cunifer alloy as stated by VECOM by forming a passive and protective sulphur complex with the cunifer alloy surface (VECOM, 2005). This will result in an increase of the corrosion resistance.

The general chemical formula is $C_5H_{10}NS_2Na$ and it dissolves readily in water. The molecular structure can be seen in Figure 13. Protection is offered by restraining the access to the cunifer surface by the tail ends of the SDMC molecule (the ethyl groups), thereby restricting the reduction reaction of oxygen. The monolayer of SDMC molecules is gradually removed when fresh seawater enters the pipe system.
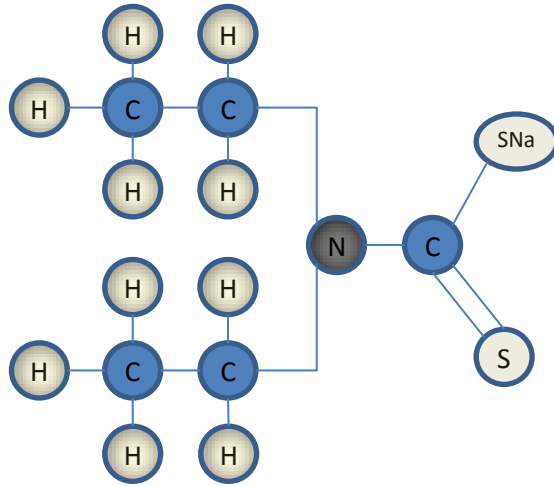

Figure 13: Molecular structure of sodium diethyldithiocarbamate (SDMC). The two sulphur atoms on the left will form a bond with the copper atoms on the metal surface. The ethyl groups (right) hinder access to the surface.

Chapter 2: Experimental details

The CuNi10Fe pipe used in this research originates from KME Germany GmbH & Co. KG and was a seamlessly drawn tube with inner diameter 267.0 mm and wall thickness 3.0 mm. The mechanical properties are summarized in Table 4. The chemical composition is shown in Table 5.

Table 4: mechanical properties from analysis at KME Germany

Werkstoff number	2.1972.11
$R_{p\,0,2}$	160 MPa
R_m	335 MPa
elongation	43%
Brinell hardness	77 HBW
Delivery condition	Annealed, seamlessly drawn

Table 5: chemical composition in wt% of the pipe where the samples originated from (KME Germany GmbH & Co. KG, 2010).

Cu	Ni	Fe	Mn	C	Pb	S	Zn	P	Zr
86.98	10.29	1.61	0.80	0.0004	0.004	0.004	0.008	0.0033	0.01

Figure 14: 100 mm rings were cut from 6 m long CuNi10Fe pipe.

For the corrosion experiments the specimens needed to be welded first. 64 corrosion specimens were needed and some more to perform surface analysis and as back-up. All specimens came from a 6 m long CuNi10Fe pipe from KME. The pipe inner diameter was 267.0 mm with 3.0 mm thick wall (outer Ø 273.0 mm). This size was chosen because it is most advantageous to choose a pipe where on the inner wall most easily a container can be placed where NaCl solution and electrodes can be put to perform the polarization tests. For this the flattest inner surface is best, and this is achieved by using a bigger diameter pipe. This pipe is the biggest pipe that is used for the pipe systems and therefore was readily available. Another advantage is that a piece of pipe is large enough to accommodate 4 sample surfaces. Each sample will be made from a 100 mm long pipe segment welded to another 100 mm long pipe segment. This pipe segment will then be cut in half and then in half again to create the four samples. This is schematically shown in Figure 15.
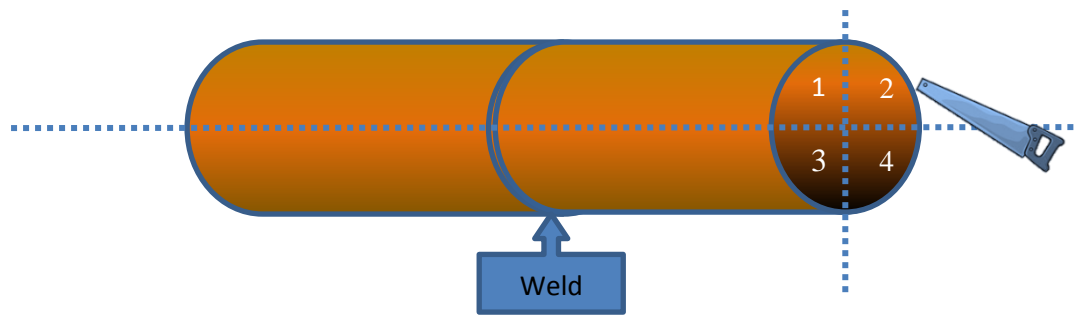
Figure 15: Schematic drawing of sample creation. Two rings were welded together followed by cutting them in four quarters.

2.1 Welding procedure

The first step was to cut 100 mm long pipe segments from the 6 m long pipe (Figure 14). This was done using a mechanical saw. 40 pipe segments were so created. Edges and surfaces were left as they were until welding. The 40 pipe segments were joined using 20 welds. The so created 200 mm long pipes were designated with letters A till T. 10 of the welds (A till H, S and T) were welded with use of argon backing gas. The other 10 welds (I till R) were welded without backing gas so oxygen was present at the inner side of the pipe. Before welding the edges of the pipe segments to be welded were chamfered using an abrasion disk and the inner and outer surface near the weld was grinded. Pipe segments to be welded without backing gas were then put on top of each other and tack welded. The pipe was then tilted and welded, position 1G/PA. Tack welds were cut away when met.

The welding method used was TIG welding in combination with filler wire UTP A 387 with wire diameter 2.4 mm, see previous. Three different charges of filler wire were used. The composition of these wires can be found in Table 8. The shielding gas was argon. TIG welding was performed using DC current with the electrode at negative polarity (workpiece positive). This will result in most heat present at the workpiece, instead of at the electrode. The machine used was a Kemppi MasterTig 3000MLS, the electrode used was WL20 from Wolfram Industrie mbH. The electrode was 2.4 mm in diameter and originally 175 mm long. It is free from thorium oxide. For the pipe segments welded with backing gas the same configuration was used except that the ends were covered with wooden plates as shown in Figure 16. One end had a hole to release the air inside the pipe, at the other end a nozzle was entered into the pipe out of which argon flowed. The argon flow was on for at least 5 minutes before welding was started to ensure all oxygen had flown out of the inside of the pipe segments by the argon flow.

Set-up for welding with backing gas
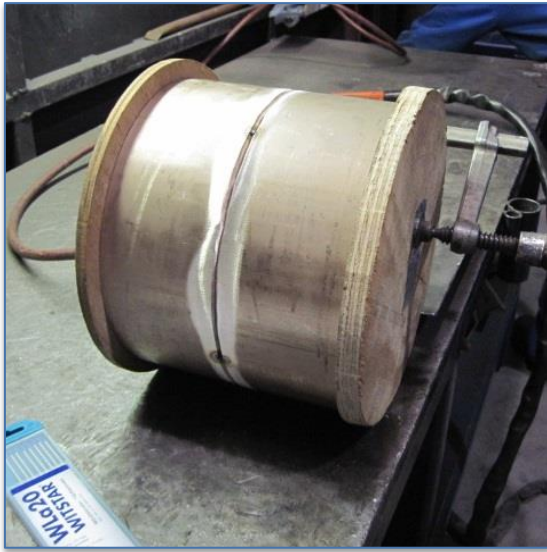
Detail of argon backing gas entering the pipe

Welding of pipe without backing gas

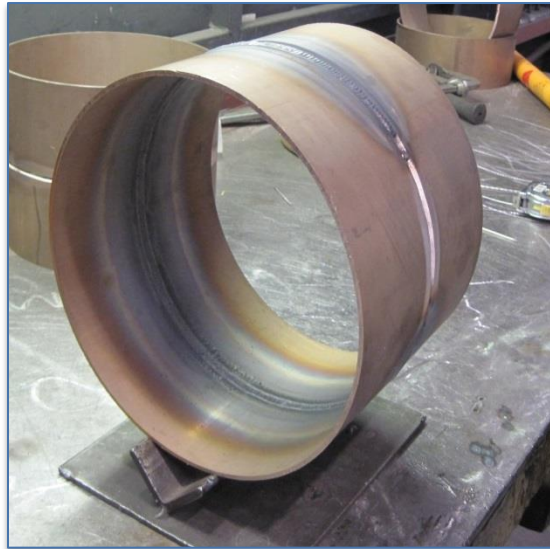*Set-up for welding without backing gas*

25

Figure 16: photos of actual situation while welding with and without backing gas
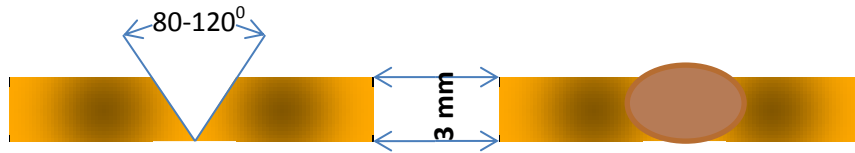
Figure 17: Schematic drawing of weld configuration (side view). Left the two ends of pipe before welding with a v-groove of 80-120 degrees. Right is the weld itself, a single pass was sufficient.

Table 6: Welding parameters for each pipe. Pipes in the white lines will be protected with SDMC treatment.

Pipe	Current [A]	Voltage [V]	Heat input [kJ/mm]	Charge nr weld filler	Flow backing gas [L/min]	Remarks	Welder
A	100	11	0.50	101524	10		JP
B	110	12	0.60	101524	10	Angle of v-groove increased (80 to 90/100^0)	JP
C	90	10.2	0.49	101524	10		JP
D	90	10.5	0.50	101584	12	Flow increased, no visible difference in weld	JP
E	108	11	0.73	100567	10		M
F	115	11.2	0.66	100567	10	M preferred slightly smaller angle for the v-groove (80^0)	M
G	100	12.1	0.93	100567	10	Wide angle, slower and more material needed	M
H	100	10.5	0.72	100567	10		M
I	111	11.3	0.50	101524	0	First weld	JP
J	110	11.7	0.44	101524	0		JP
K	95	10.3	0.46	101584	0		JP
L	115	11.1	0.61	100567	0		M
M	102	10.4	0.55	100567	0		M
N	115	11.4	0.63	100567	0		M
O	115	11.2	0.66	100567	0		M
P	95	10.3	0.61	100567	0		M
Q	114	11.5	0.70	100567	0		M
R	100	10.5	0.63	100567	0		M
S	114	11.5	0.69	100567	10		M
T	109	11	0.61	100567	10		M

Tack welds were made first to ensure the positioning of the pipe. CuNi10Fe has a high coefficient of thermal expansion (relative to the more common carbon steel) and this will lead to greater distortions when welding. This was also experienced while welding where at first approximately 6 tacks were used per pipe segment, but later more tacks were preferred by the welder. Tack welds were cut with an abrasion disk and the edges cleaned when the actual weld reached the tack. This also happened with the start of the weld when the end of the weld came into place to close the circle.

The heat input is the principal parameter of the welding heat source. For a continuous heat source such as during welding the heat flow is usually nominated as q [J/s]. For seam welding this heat flow can be defined as the heat input q_w [kJ/mm] using the formula:

$$q_W = \frac{\eta VI}{v}$$

With q_w the heat input in kJ/mm, η the process efficiency, V the voltage in volts, I the current in amperes and v the propagation speed in mm/s (Radaj, 1992). The influence of the heat source on the temperature of the surrounding material is in seam welding dominated by the heat input per unit length of the weld, combined with the plate thickness. For the process efficiency 60% is chosen. For GTA welding with the electrode negative the advised efficiency lies between 50 and 80% (Ouden & Hermans, 2009), 60% is also used for calculating the heat input for the welding procedure specifications in practice at DSNS. The propagation speed is measured by timing a part of the weld, after which the distance done is measured. This was done for each weld since the speed varied somewhat for each pipe. Table 6 states the parameters that were obtained during welding. Current and voltage were taken as a mean over the whole weld. The heat input and welding speed were calculated and are shown in Table 7. The flow of backing gas was 10 l/min for the first 3 welds, later it was decided to increase this to 12 l/min to see if this would improve the burn through of the welds. This was not the case, and in subsequent welds it was returned to 10 l/min. Since little air already influences the inner side of the weld it is normally recommended to use a flow rate and wait time such that at least 5 volume changes have occurred before the start of welding (TWI global). With a pipe inner diameter of 267 mm and a length of 200 mm the volume of a pipe segment is 11 l. With a flow of 10 l/min this was left on for more than 5.5 minutes before welding started.

$$\pi l r^2 * 1000 = \pi * 0.2 \, m * (0.1335 \, m)^2 * 1000 = 11.19 \, litre$$

With l the length of the pipe and r the inner radius of the pipe. Both are in meters to obtain a result in m³ which is then multiplied by 1000 to obtain litres.

Because of the thickness of the pipe (3 mm where commonly for the smaller pipes 2 mm is found) proper penetration was not properly achieved everywhere. This is something that would happen also when welding in the field, which then often goes unnoticed. It was therefore decided to leave the welds as is.

Table 7: Heat input and welding speed per pipe segment. For the heat input an efficiency of 60 percent was used.

	I [A]	V [V]	t [s]	L [mm]	Heat input [kJ/mm]	v [mm/s]
A	100	11	110	145	0.50	1.32
B	110	12	110	145	0.60	1.32
C	90	10.2	102	115	0.49	1.13
D	90	10.5	102	115	0.50	1.13
E	108	11	202	196	0.73	0.97
F	115	11.2	150	175	0.66	1.17
G	100	12.1	218	171	0.93	0.78
H	100	10.5	194	170	0.72	0.88
I	111	11.3	86	130	0.50	1.51
J	110	11.7	80	140	0.44	1.75
K	95	10.3	94	120	0.46	1.28
L	115	11.1	158	200	0.61	1.27
M	102	10.4	172	198	0.55	1.15
N	115	11.4	157	195	0.63	1.24
O	115	11.2	120	140	0.66	1.17
P	95	10.3	188	180	0.61	0.96
Q	114	11.5	173	195	0.70	1.13
R	100	10.5	193	192	0.63	0.99
S	114	11.5	203	233	0.69	1.15
T	109	11	204	240	0.61	1.18

Table 8: Composition of the weld filler materials (wt%). UTP A 387 was used which has nominal composition of 30% Ni, in contrast to the pipe material which consists of around 10% Ni. (Voestapline, 2014) (Voestalpine, 2014) (Voestalpine, 2013)

Charge nr.	C	Si	Mn	P	S	Ni	Cu	Ti	Fe	Pb
100567	0.03	0.02	0.7	<0.01	<0.01	30.6	67.6	0.3	0.6	<0.01
101584	0.03	0.06	0.8	<0.01	<0.01	30.6	67.5	0.3	0.6	<0.01
101524	0.03	0.04	0.8	<0.01	<0.01	30.7	67.4	0.3	0.6	<0.01

2.2 Preparation of the samples

After welding the samples were cut in 4 quarters using a mechanical saw. Each sample was marked with the letter of the pipe segment it originated from, followed by numbers to indicate the experiments that were to be performed. Each type of test was repeated four times. To achieve a better distribution of the tests each repetition was taken from a different pipe segment. Also for each test pipe segments welded by both welders were used so any differences herein could be seen. This most likely caused a larger distribution in the obtained results, but this also better reflected the practical situation where different welders are used and circumstances change and therefore is less likely to show a false accuracy.

Table 9 lists the tests that are performed and the sample numbers for those tests. Because of the fragility of the SDMC layer the samples were first cut and then send to VECOM to apply the treatment. The edges were burred so the samples can be handled with fewer risks. The corrosion tests will be performed in the middle of the samples, away from the burred edges, where there is a risk of cold work. There were 16 different tests to be performed on pipes A to P. Pipe segments O to T were used for surface analysis and back-up. Pipe segments A to H and S and T were welded with backing gas, I to R without backing gas.

The 16 pipe segments used for corrosion tests were cut in four pieces, creating 64 samples. 32 of these samples (16 welded with and 16 without backing gas) received the SDMC treatment by VECOM. On the samples corrosion tests were done on four zones, the whole region to determine an overall corrosion rate, the weld zone to determine the corrosion rate of the weld material, the heat affected zone, and the base metal. The total division of tests is shown in Table 9.

Table 9: Designation of polarization tests. Different pipe segments are used for every test to gain more diversity in the test results. Testing is done between samples with and without backing gas, with and without SDMC treatment, all over different regions.

Nr			zone		Nr			zone
A.1.1	BACKING GAS	NO SDMC	WHOLE REGION POLARIZATION		A.9.1	BACKING GAS	NO SDMC	HAZ POLARIZATION
C.1.2					C.9.2			
E.1.3					E.9.3			
G.1.4					G.9.4			
B.2.1	BACKING GAS	SDMC	WHOLE REGION POLARIZATION		B.10.1	BACKING GAS	SDMC	HAZ POLARIZATION
D.2.2					D.10.2			
F.2.3					F.10.3			
H.2.4					H.10.4			
I.3.1	NO BACKING GAS	NO SDMC	WHOLE REGION POLARIZATION		I.11.1	NO BACKING GAS	NO SDMC	HAZ POLARIZATION
K.3.2					K.11.2			
M.3.3					M.11.3			
O.3.4					O.11.3			
J.4.1	NO BACKING GAS	SDMC	WHOLE REGION POLARIZATION		J.12.1	NO BACKING GAS	SDMC	HAZ POLARIZATION
L.4.2					L.12.2			
N.4.3					N.12.3			
P.4.4					P.12.4			
A.5.1	BACKING GAS	NO SDMC	WELD ZONE POLARIZATION		A.13.1	BACKING GAS	NO SDMC	BASE METAL POLARIZATION
C.5.2					C.13.2			
E.5.3					E.13.3			
G.5.4					G.13.4			
B.6.1	BACKING GAS	SDMC	WELD ZONE POLARIZATION		B.14.1	BACKING GAS	SDMC	BASE METAL POLARIZATION
D.6.2					D.14.2			
F.6.3					F.14.3			
H.6.4					H.14.4			
I.7.1	NO BACKING GAS	NO SDMC	WELD ZONE POLARIZATION		I.15.1	NO BACKING GAS	NO SDMC	BASE METAL POLARIZATION
K.7.2					K.15.2			
M.7.3					M.15.3			
O.7.4					O.15.4			
J.8.1	NO BACKING GAS	SDMC	WELD ZONE POLARIZATION		J.16.1	NO BACKING GAS	SDMC	BASE METAL POLARIZATION
L.8.2					L.16.2			
N.8.3					N.16.3			
P.8.4					P.16.4			
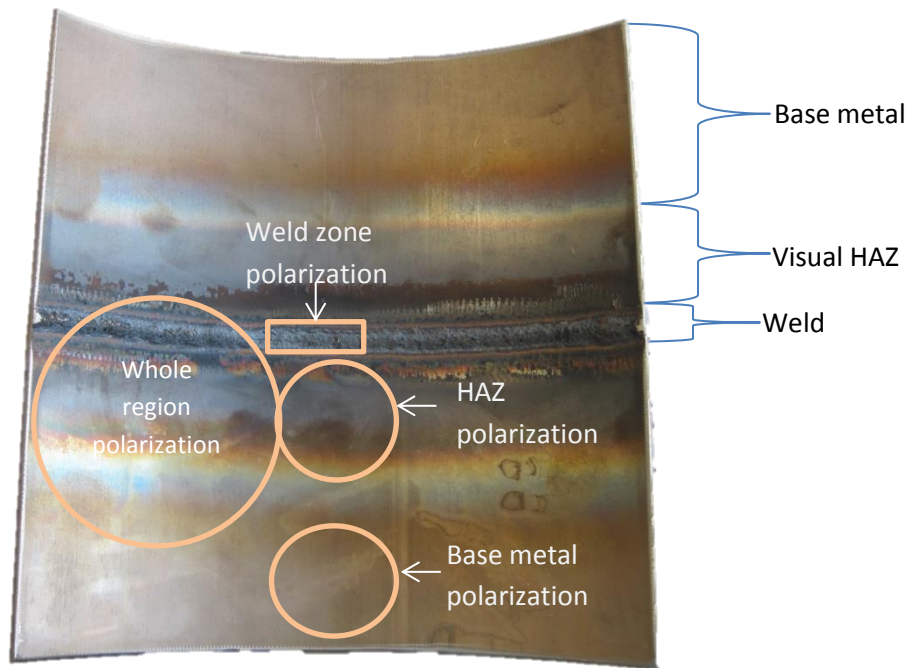
Figure 18: Overview of regions and polarization zones as given in Table 9. The regions are indicated in orange. These regions were used for polarization tests. The different zones can be seen on the right.

The different zones mentioned in Table 9 are illustrated in Figure 18. The orange circled areas are representations of the polarization areas. The extent of the different zones on a sample is showed right with accolades.

2.3 Application of the SDMC protection

Sodium diethyldithiocarbamate was applied to the welded samples which were designated to be protected. The SDMC layer is not resistant against scratching or hard handling. In practice it would be applied by flushing the pipe system after completion. The pipes are then all placed in the vessel with sufficient air vents. A retour is added from one end of the pipe system to another (the inlet of seawater and the exit). Herein is then a solution of SDMC and demi-water added from containers and recirculated through the system. The solution has a pH value between 7.0 and 8.0. After a period of circulation the pumps will stop so the solution comes to rest. In this period the SDMC has time to adhere to the surface of the cunifer pipes. The whole process will take up to 24 hours to ensure proper adhesion (VECOM, 2010). After this time the solution of SDMC is removed from the pipes and the pipes are rinsed with demi-water. Because of the fragility it was decided to first cut the pipe segments into quarters and then dipping the quarters in a SDMC bath. The same method is sometimes used for separate pipes that need to be treated. The treatment was performed by VECOM at their facilities in Maassluis. The Vecom Cunifer Passivation Liquid that was used contained the SDMC. The samples were entered into the bath for 24 hours. The solution had a pH between 7.0 and 8.0. After 24 hours the samples were removed from the bath and rinsed with demi-water.

The samples were placed in dripping trays for transport. This resulted in half a ring on the samples where the tray damaged the SDMC coating (see Figure 19). This area was not used for further testing.

31

Ring

Figure 19: Pipe segment R3 (welded without backing gas). At the bottom the damaged area can be seen. This is a result of placing the segments in a dripping tray.

2.4 Surface analysis

2.4.1 Etching of the samples

To determine the microstructural differences between the different zones as determined before cross sections are investigated under an optical microscope. From pipe segments Q and S strips 10 mm wide were cut with a belt saw. Segment Q is a pipe segment welded without backing gas and S a segment welded with backing gas. Both samples were not coated with SDMC. SDMC samples were not looked at in this section since the coating is only a molecule layer thick and easily removed, a cross section would not show the coating. The strips were taken such that all areas (weld, HAZ, base) were represented. These strips were then cut into three sections using a diamond cutting machine with coolant. The sections were approximately 3 cm long to be able to fit in the sample holders. The resulting samples are shown in Figure 20. The HAZ starts directly next to the weld. A very small region can be seen in section 3.2 where the microstructure of the CuNi10Fe is notably different compared to the normal structure. On the surface a larger region can be seen where on the surface discoloration can be found. Following the terminology of Little, Wagner, and Jacobus this discoloration is named the visual HAZ (Little, Wagner, & Jacobus, 1988). The sections as divided for surface analysis are designated as follows:
- Weld area (including the microstructural HAZ and part of the visual HAZ)
- HAZ (remaining part of the visual HAZ)
- Base material

Figure 20: Cut samples for surface analysis. From top to bottom: base, visual HAZ, weld area. Left the samples without backing gas, right the samples welded with backing gas. The surface to be examined is the side of the top of the samples shown here.

With the cut edge down the sections were placed in a mould with springs to keep them standing up. The mould was then filled with resin. The resin hardened in half an hour after which 2 mm of the bottom (where the cut edge was present) was sanded off with wet sand paper grade 80. This was followed with sanding with grades 180, 320, 800, 1200 and 2000. The samples were rinsed with ethanol between steps. After rinsing and drying the samples were then polished on a polishing cloth with an emulsion of 3 μm abrasion liquid. The final polishing step consisted of polishing with a 1 μm abrasion liquid. The polished samples were then rinsed with ethanol and dried in warm air. In between steps and after the final polishing the samples were kept in a desiccator to keep moisture away from the surface.

To be able to see the microstructure the samples needed to be etched. Following ASTM standards (ASTM, 2000) several options are available to etch CuNi10Fe. Earlier research made use of ASTM E407 no. 34 etchant (Schielab, 2012). This etchant is also used in this research. Etchant no. 34 is made of 5 g $FeCl_3$ (SIGMA-ALDRICH, 2015), 50 ml HCl (SIGMA-ALDRICH, 2015) and 100 ml demi-water. The sample is then immersed in the solution with plastic tweezers. To determine the immersion time needed for the best results immersion started with 1 second. The sample was then rinsed with demi-water and dried. The result was checked under a microscope. This was followed by immersion of 2 more seconds and the same rinsing and checking routine was used. The results were checked after every 2 seconds of immersion and an immersion time of 10-11 seconds was

determined best for these samples in this solution. All samples were then immersed for 10 seconds and checked.

2.4.2 Optical microscopy

The etched samples were first investigated using an Olympus BX60M microscope. Etch effect just as seen in earlier research appeared as dark lines on the surface (Berg, Kievits, & Lange, 1968). Different immersion times in the etchant were tried, but with this microscope no clear image was acquired. It was then tried to examine the samples under a Keyence VHX-5000 microscope. This microscope was able to light the sample differently such that the lines did not appear so strong. This microscope was then used to obtain the final results. The microscope used a lens with 250x magnification, and this magnification was used for all images, except for the weld overviews where a lens of 30x magnification was used.

Several images were taken of each section. The most representable image was printed with a scale bar. The grains were then traced and retraced on the back to gain a black and white image. This black and white image was then scanned and used in the software package ImageJ to calculate the number and area of the traced grains. This gives an indication of the grain areas found in each section.

2.4.3 Scanning electron microscopy (SEM)

To further investigate the structure of the samples a scanning electron microscope (SEM) was used. It is further used to determine the composition at selected areas with Energy Dispersive Spectroscopy (EDS). The same samples that were used for analysis under an optical microscope were first used after polishing to investigate in a SEM. The SEM used was a JEOL JSM 6500F with EDS technique. The EDS was used to determine the chemical composition at certain areas such as the top of the weld.
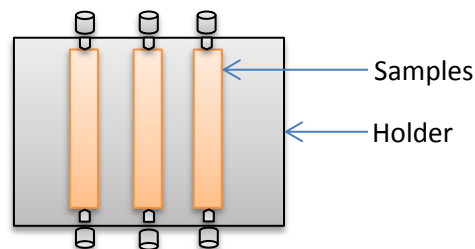
Figure 21: Schematic of sample placement on the sample holder placed in the SEM.

The samples were prepared by ultrasonic cleaning in ethanol for 2 minutes. The samples were then dried in a nitrogen gas stream and placed in a sample holder. There was room for 3 samples in the sample holder. The samples were placed with the side to be investigated facing up and secured with screws. This configuration is shown in Figure 21. The samples were placed with the polished side up to examine that area. They were kept in place with screws. The sample holder was then placed in the SEM.

The acceleration voltage used was 15 kV, with a medium current of the probe of $2*10^{-11}$ A. The secondary electron detector was on and the backscatter electron detector was present. The backscatter electrons (BSE) give more information about chemical phase differences while the secondary electron imaging shows more the topographic features. Since the goal here was to find differences in chemical structure the samples were primarily investigated with BSE. The backscattered electrons are electrons that hit atoms inside the sample and were reflected back. Therefore they come from deeper in the sample than the secondary electrons that are emitted from atoms on the top surface. This leads to the BSE image having a lower resolution than the SEI image.

The analysis depth using secondary electrons is around 5 nm. For backscatter analysis the depth is increased to around 400 nm.

To identify the elemental composition de EDS detector is inserted. The EDS detector can detect X-rays emitted by atoms in the sample when they are hit by the electron beam as a result of shell transitions. Measuring the energy of these X-rays can give information about the atom it originates from. The depth of this analysis usually falls between 1 and 2 µm. EDS measurements were taken from points or areas specified on a BSE image acquired beforehand.

2.4.4 Scanning Kelvin Probe (SKP)

Figure 22: Scanning Kelvin Probe. Left the step motors are visible to move the table and probe. Inside the chamber the sample and probe are present. The chamber is kept at a constant humidity.

Scanning Kelvin Probe (SKP) was used to measure the surface potential of the sample, which is related to the work function. The work function Φ is defined here as the minimum work that is required to extract an electron from the sample to just outside the sample. An electrochemical reaction such as the oxidation reaction of a metal also involves the extraction of an electron from within the metal. However caution should be taken when comparing the SKP results with corrosion results since in SKP no electrolyte is present and the circumstances are different (Rohwerder & Turcu, 2007). Here a Kelvin probe was used from KP Technology with automatic humidity control. When this machine is calibrated (in this case with a Cu/Cu^{2+} reference electrode) the Volta potential ψ.

The SKP consists of a metallic probe electrically connected to the sample and a power source. The probe vibrates close over the surface. This separation will make the probe and the sample act as a capacitor, which has a dependency on the separating distance. This distance varies with the modulation of the probe. To get accurate results it is important to keep the distance between probe and surface as close and steady as possible, but the samples contained a protruding weld area. Over the weld area the probe was guided to maintain the same distance (mean distance around which the probe vibrated) between sample surface and probe. The samples consisted of 10 mm wide strips, 100 mm long. 4 samples were tested, with and without backing gas and with and without SDMC treatment. The potential gradient (inversely proportional to the distance above the surface, dimensionless) was kept for all samples at 299. Measurements started at the weld and went down to the base material for 70 mm. Every 700 µm the work function was recorded.
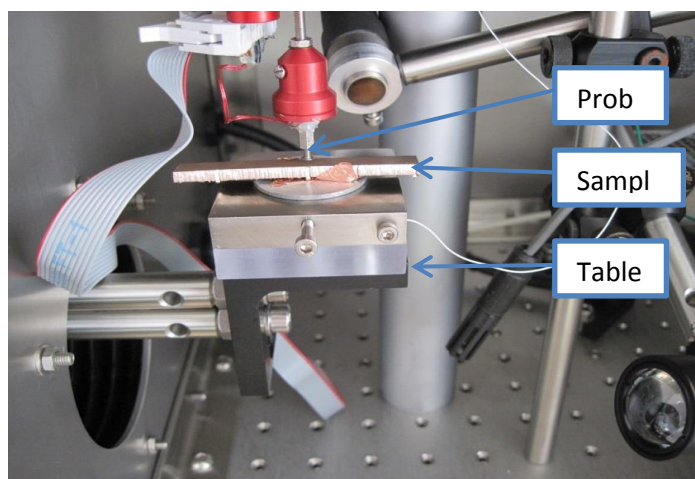
Figure 23: Probe and sample inside chamber of the SKP. This sample did not contain a weld to test the set-up. All measurements were performed on the samples with weld. To scan the surface the sample table was moved via step motors outside the chamber.

2.5 Immersion of the samples

To see how the material behaves naturally in the test solution tests were performed were small samples were kept in the solution at room temperature and the process was visually monitored. For this purpose small samples from pipe segments Q, R, S, and T were cut (using a belt saw) of approximately 4.5 by 6 cm. The pieces were cut so that the long edge of the piece aligned with the weld area up to the base area. The samples were then covered with (green) tape at the back side and edges. This was done to prevent unwanted effects of the cut sides and the back side. Plastic containers were used to contain the samples and the solution.

Two types of solution were used to represent the two environments of interest. The first solution consisted of demi-water with 3.4% NaCl added. This artificial seawater approximated clean seawater as found in deep sea areas. This was achieved by dissolving 34 grams of NaCl in a litre of demi-water. The second solution also contained 34 grams of NaCl, but also 2.92 grams of $Na_2S_2O_5$. The added sulphur recreates the sulphide contamination present in harbours and coastal waters. As stated before, this contamination should influence the corrosion characteristics significantly. Since HS^- and $SO4^{2-}$ are in balance (Millero, 1986), and from literature it is known that addition of 1.2 ppm Na_2S gives the desired concentration of HS^- (and thus of $SO4^{2-}$), the desired amount of $Na_2S_2O_5$ can be calculated. With the molecular weight of Na_2S of 78.04 g/mol and the desired 1.2 g/l of contamination calculation leads to $1.54*10^{-2}$ mol Na_2S per litre. To obtain the same amount of moles of $Na_2S_2O_5$ the molecular weight is needed. The compound is acquired from SIGMA, which gives the molecular weight as 190.11 g/mol (SIGMA-ALDRICH, 2015). Combined with the $1.54*10^{-2}$ mol needed it is determined that 2.92 g/l of $Na_2S_2O_5$ needs to be added to 1 litre of demi-water to obtain the desired contamination.

The samples in 3.4 wt% NaCl were placed in the solution for 5 weeks. Every two weeks the solution was replaced since by then a significant amount had evaporated, which influences the concentration of dissolved NaCl. Every sample was placed in 500 ml of solution in a separate container. Photographs were taken to monitor the progress. The first set of samples in the sulphide containing 3.4 wt% NaCl was left in the solution for 1 week. The results led to a second set of samples also placed in sulphide containing 3.4 wt% NaCl. This set was placed in the solution for four days.

2.6 Electrochemical polarization tests

For an electrochemical process the rate of reaction can be expressed by Faraday's law:

$$m = \frac{Ita}{nF}$$

With *m* the mass that has reacted in grams; *I* the current in A; *t* the time in s; *a* the atomic weight of the material that reacts; *n* the number of electrons that is transferred; and *F* the Faraday constant which is 96500 C/mol. This can be converted to a corrosion rate r which then is defined as the reacted mass (m) divided by time (t) times surface (A).

$$r = \frac{m}{tA} = \frac{ia}{nF}$$

This then leads to *i* which is defined as the current density I/A. The reaction rate is therefore linear depended on the current density. The current density cannot be calculated but can be measured via polarization tests. If an overvoltage is applied (polarization) on an electrochemical cell the current density will change due to accelerated electrochemical reactions.
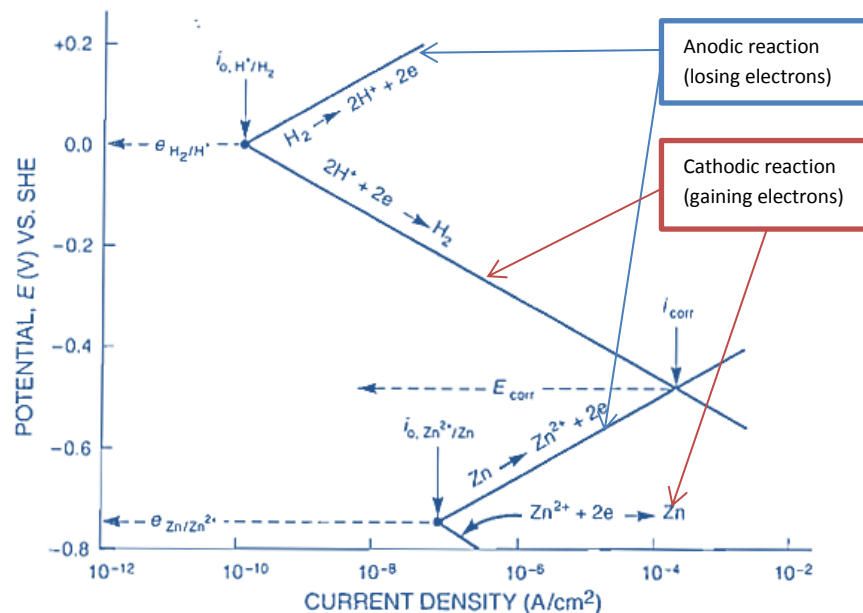
Figure 24: Anodic and cathodic reactions for both half cells in the electrochemical cell of a zinc-hydrogen electrochemical cell (Jones, 1995)

For a half cell reaction polarization in positive direction favours one direction of the reaction, while polarization in negative direction leads to the reverse direction. This then leads to a Tafel plot were the polarization potential is plotted against the current density as measured. This can be done for both half-cell reactions that form the electrochemical cell. The reactions are shown in Figure 24 with as an example the reactions for hydrogen and zinc. If the direction of reaction leads to a release or losing of electrons this reaction is called anodic, while if the direction of reaction is the opposite where electrons are gained it is called cathodic.

However these reactions cannot occur independently. Therefore the reactions that will occur are at the cross point that is reached by extending the cathodic part of the upper set of reactions and the anodic part of the lower set of reactions. The straight lines drawn here are dependent on the fastest step in the reaction. If the reaction is however very fast there can occur a depletion of the species needed for the reaction on the surface. This will lead to a deviation of the straight line. This usually only occurs for the cathodic reaction (involving oxygen) since the anodic reaction usually involves metal atoms of which there is an abundance.

An example of measuring the polarization curves is shown in Figure 25. For high potential and high current densities the measurements will line up with the theoretical values as can be seen in the figure (Jones, 1995). From these measurements the current density (i_{corr}) and the joint corrosion potential (E_{corr}) can be determined by extending the regions that overlap (called Tafel regions) with the true values. The i_{corr} determines the corrosion rate, the rate of corrosion, E_{corr} is the potential of natural corrosion. The E_{corr} values are used to compare the nobility of different metals in similar situations. Protection methods can alter i_{corr} or E_{corr} for a certain set-up, depending on their protection mechanism. Protection methods such as sacrificial anodes alter the E_{corr}, preferentially making the metal to be protected nobler, while protection methods that hinder access to the surface alter the i_{corr}, lowering the corrosion rate.

At very high over-potentials sometimes passivation behaviour shows in the polarization curves. Above a passive potential E_{pp} the corrosion rate decreases significantly. This behaviour is shown in Figure 26. Here the curve is shown for higher potentials. The anodic reaction is drawn. At Epp the passive layer starts. Even higher, above the passive zone, the layer starts to break and the over-potential is high enough so that the corrosion rate increases again.
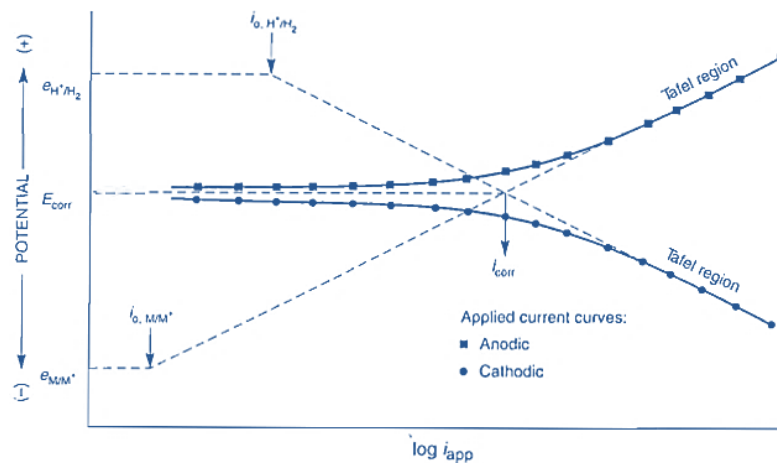
Figure 25: Simulated experimental polarization curves (Jones, 1995). For high potential and high current densities the measurements will line up with the theoretical values. The joint corrosion potential and current density can be determined by extending the overlapping regions.
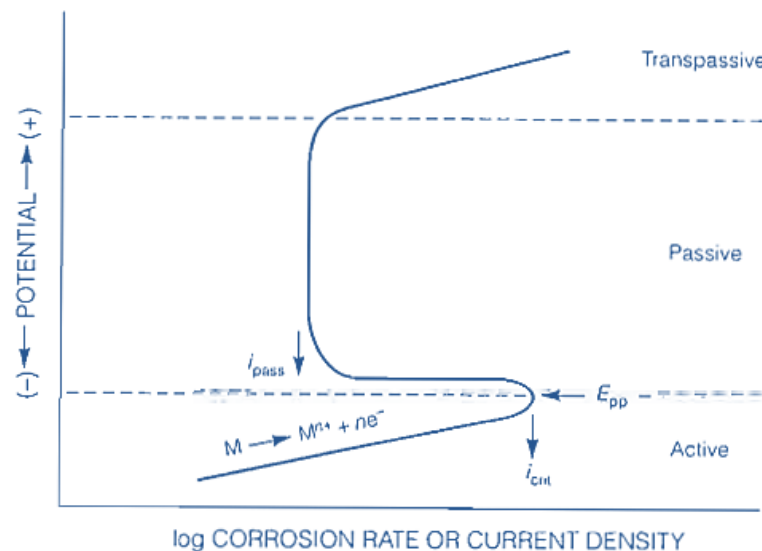
Figure 26: Schematic active-passive polarization behaviour. Above Epp the corrosion rate decreases significantly after which it stays constant up to the transpassive state, where the passive layer breaks and the material is once again in an active state. (Jones, 1995)

To compare the different samples polarization tests were performed. For these tests three potentiostats were used. The first was a Schlumberger SI1286 with software Corrware 3.3a. The other machines were both Autolab machines with software NOVA 1.9.16 and NOVA 1.10.1.9 respectively. For the polarization tests of the weld, visual HAZ, and base zones a small cylinder with inner diameter 35 mm was used to contain the electrolyte. For the tests over all three zones a cylinder with inner diameter 60 mm was more suitable. On the (curved) surface of the sample first a layer of lacquer was applied. This was done to prevent crevice corrosion. A crevice could be formed between the surface layer and the silicon used to bind the cylinder to the sample. The lacquer prevented accelerated corrosion in this area. The smaller cylinders had a notch wherein a rubber O-ring fitted. This O-ring secured the water-tightness of the seal between the cylinder and the surface.

The reference electrode and counter electrode were suspended in the cylinder. As reference electrode three calomel electrodes were used (one for each set-up). A calomel electrode consists of mercury in contact with a KCl solution. The mercury and solution are contained in a glass tube wherein the solution is saturated with Hg_2Cl_2 (Vetter, 1967). The electrodes were stored between tests in a saturated KCl solution to ensure that the solution inside the electrode remained saturated with Hg_2Cl_2. The electrodes were checked regularly to ensure consistent results. For the counter electrode three graphite rods were used. Together with the working electrode (the sample) these three electrodes were connected to the potentiostat. For the first two hours the open circuit potential (OCP) was measured. For this set-up no over-potential was applied, and the natural occurring corrosion potential was measured over time. As soon as a steady situation occurred the polarization test was started.

A day after the cylinders were glued to the samples the electrodes were suspended in the cylinder and the electrolyte was added. Water-tightness was checked and then the OCP measurement started. After two hours the polarization test started.

Calomel reference electrode

Graphite counter electrode

CuNi10Fe working electrode (sample)
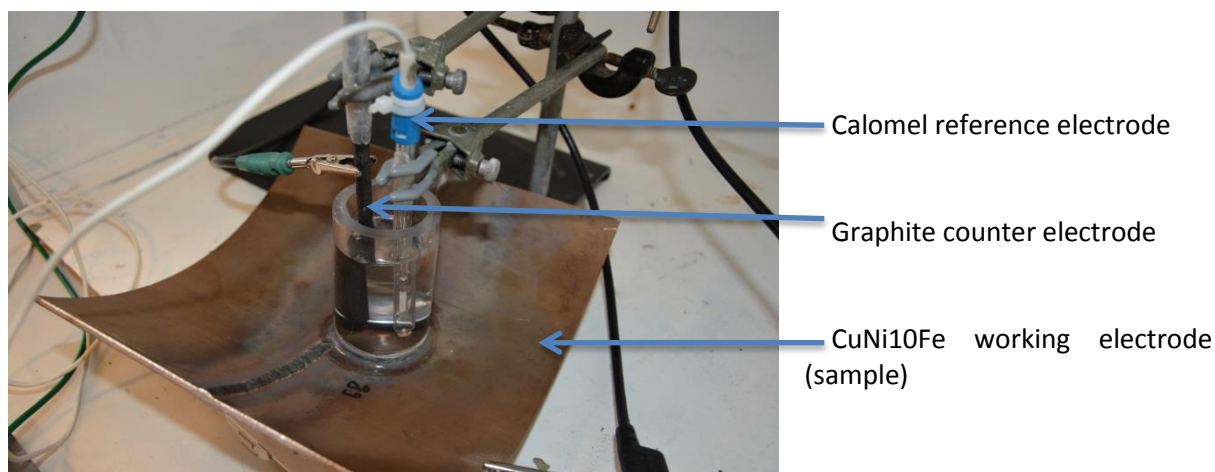
Figure 27: Electrodes used for polarization tests. The sample is connected to the potentiostat via a crocodile clip on a sanded (for good electrical connection) part of the sample. Reference and counter electrode are suspended in the cylinder.

Polarization commenced at -0.5 V versus the measured OCP. The scan rate was 0.1 mV per second. This is a higher scan rate than often used (1 mV or more per second) to make sure every measurement is in an equilibrium state before measuring. This is important since there is not a lot of difference to be expected between the different areas.

During the increase in voltage the current was measured. For the measurements on the Schlumberger machine the increase continued until 0.4 V above the reference (0 V difference between measurement and calomel reference electrode). This value was chosen to be able to see if and when the passive layer breaks. This was not possible to reach with the Autolab machines where

an overload occurred at 0.2 V above the reference. This did not hinder the measurements since the corrosion potential and current are determined below that potential and the behaviour of the passive layer could already be seen in using the measurements with the Schlumberger machine.

After the polarization measurement the electrodes were removed and rinsed with demi-water. The calomel reference electrode was returned in a saturated KCl solution to keep intact. The electrolyte had a pH of 12-14 after polarization and was discarded of accordingly. The cylinder was removed from the sample and the surface rinsed with demi-water. The surface was then dried in an air stream. To find the current density from the measurements it is important to know the surface area that was corroded. For this purpose the area was photographed with a scale next to it and the area of corrosion was determined using ImageJ software (National Institutes of Health, 1997). The average of three area measurements was then used to calculate the current density.

Two situations were recreated, without sulphide contamination and with. For the situation without sulphide contamination the electrolyte consisted of 34 grams of NaCl per litre demi-water, similar to the solution used for the standing tests. For these samples it took two hours to come to a steady state because of the choice not to polish or clean the sample surfaces. This was done to prevent the disruption of the surface layers (SDMC and oxidation) and test the samples as they are in practice. The pH of the solution before placing it in the container is pH 7. For the sulphide containing situation the electrolyte used consisted of 34 grams of NaCl dissolved in 1 litre demi-water and 2.92 grams of $Na_2S_2O_5$. This solution corroded the surface faster and already after 10 minutes a stable OCP could be seen. This shortened test times significantly.

The samples used for testing in sulphide containing 3.4 wt% NaCl are stated in Table 10. The sample numbers refer to the previous tests. There was enough clean and unused surface area left after the previous tests to place a cylinder on a different area of the sample for these tests. However, due to time restraints these tests were repeated only once for each type of sample. The results of the tests in 3.4 wt% NaCl stated above matched enough to justify this decision.
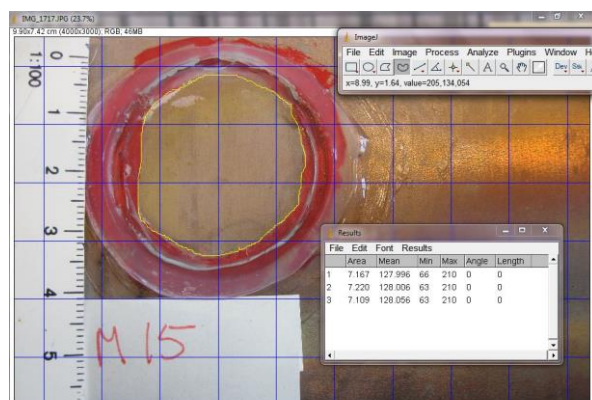
Figure 28: ImageJ software used to calculate the area of corrosion. The area is surrounded by lacquer and the remnants of the silicon seal between surface and cylinder. For each surface three measurements were taken and the average was used for calculations.

Table 10: Sample numbers used for polarization tests with sulphide containing 3.4 wt% NaCl.

Nr			Zone
C13S	BACKING GAS	NO SDMC	WHOLE REGION
E9S			
F14S	BACKING GAS	SDMC	WHOLE REGION
B14S			
O11S	NO BACKING GAS	NO SDMC	WHOLE REGION
I11S			
P16S	NO BACKING GAS	SDMC	WHOLE REGION
L12S			
E13S	BACKING GAS	NO SDMC	WELD ZONE
A9S			
H14S	BACKING GAS	SDMC	WELD ZONE
D2S			
I15S	NO BACKING GAS	NO SDMC	WELD ZONE
K15S			
N16S	NO BACKING GAS	SDMC	WELD ZONE
P12S			
A13S	BACKING GAS	NO SDMC	HAZ
L8S			
D14S	BACKING GAS	SDMC	HAZ
T1S			
O15S	NO BACKING GAS	NO SDMC	HAZ
O3S			
J16S	NO BACKING GAS	SDMC	HAZ
R3S			
E5S	BACKING GAS	NO SDMC	BASE METAL
C9S			
H6S	BACKING GAS	SDMC	BASE METAL
J4S			
O7S	NO BACKING GAS	NO SDMC	BASE METAL
K7S			
P8S	NO BACKING GAS	SDMC	BASE METAL
N8S			

Chapter 3: Results

3.1 Visual inspection of the samples

After welding differences between samples welded with and without backing gas were evident. Photographs of the welds were taken and shown in Figure 30, Figure 31, Figure 32, and Figure 33. In the weld area the weld welded with backing gas is relatively smooth and has a metallic shine. Next to the weld a discoloured zone is present. This discoloration is present in the metal itself. This discoloration is also visible in the welds welded without backing gas, but here that area is also covered with a black residue. This black layer easily comes off and underneath the same discoloration is seen as for the weld with backing gas. The weld itself for the samples without backing gas is not smooth. Craters and bulges are present as well as bad penetration in some areas. The weld itself is approximately 6 mm wide. Discoloration of the surface occurred usually within 40 mm away from the centre of the weld.

The samples coated with SDMC inhibitor appeared darker in colour. Most of the loose black layer at the samples welded without backing gas was gone by then and thus did not interfere in the adhesion of the SDMC. However the pores and cavities in the irregular welds without backing gas were less dark in colour then the surrounding areas. The pores are shown in Figure 29 where blue circles indicate their location.

The samples were not polished or cleaned; the electrochemical tests were performed on the samples in their original state.

6 mm

Figure 29: Weld without backing gas (pipe segment N). Shiny craters are visible (blue circles) which are lighter in colour than the surrounding material.

Figure 30: Weld with backing gas (pipe segment F). Weld surface is smooth and has a light shine to it.

Figure 31: Weld without backing gas (pipe segment I). The weld did not penetrate through the thickness of the pipe as can be seen at the line/edge running through it.
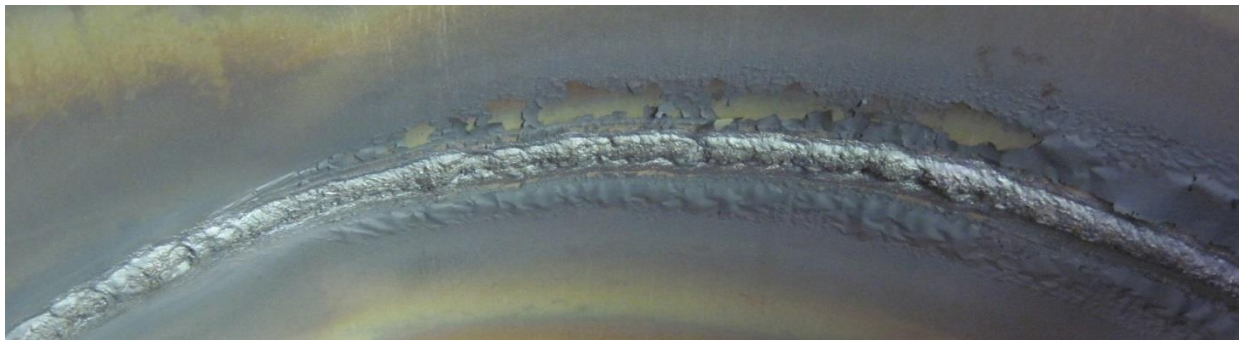
Figure 32: Weld without backing gas (pipe segment R). Very loosely adherent black layer can be seen at the HAZ. Weld surface is very rough.

Figure 33: Weld without backing gas (pipe segment N). Pores are visible in the weld area. Most of the black layer already came loose.

3.2 Characterisation of the microstructure over the welded zone

Cross sections of the welds were investigated using optical microscopy to determine the microstructure of the different regions over the sample.

Overviews of the welds are shown in Figure 34, left with backing gas and right without backing gas. No cracks were visible and only one pass was used for these welds. Both images show the inside of the pipe on the top side of the image. For the weld welded without backing gas here the irregularities are visible that form the pores when looking at the top of the weld.
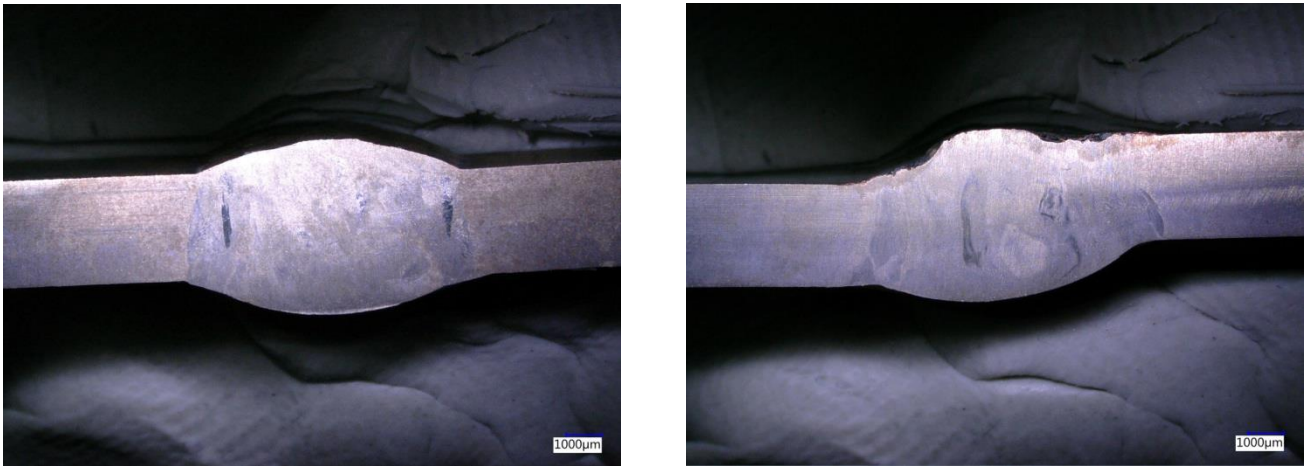
Figure 34: Overview of welds. Left the weld welded with backing gas; right the weld welded without backing gas. Magnification 20x. On the top of the sample the inside of the pipe can be seen. Right the rough surface of the backside of the weld without backing gas can be seen.

Microscope images were made from all sections. Figure 35 shows an image of the base section welded without backing gas. These kinds of images were used to determine grain areas. Twinning bands can be seen in several grains. The microstructure looks very different in the weld, as shown in Figure 36 where a cellular-dendritic structure can be seen. This is the weld section, also of the sample welded without backing gas. The pores that were shown before on the surface of these welds can also be recognized here in the cross section. Figure 37 shows again the weld section, but this time of the sample welded with backing gas. The image shows the microstructural HAZ were the weld material meets the base material. On the left side the grain structure can be seen similar to Figure 35 while on the right the more cellular-dendritic structure is shown, similar to Figure 36. A broader overview can be seen in Figure 39 and Figure 38. This is the result of stitched images (images taken after each other, put together using software on the microscope). In the overview the weld region is visible on the right side. The transformation from the cellular-dendritic structure to a more rounded grain structure can be seen in the middle area of the images. From the microstructural HAZ (very close to the weld area) to the base material (towards the left side of the images) the grain sizes can be seen. No obvious changes were found.

Figure 35: Sample welded without backing gas, base material section. Etched for 10s. Twinning bands can be seen.
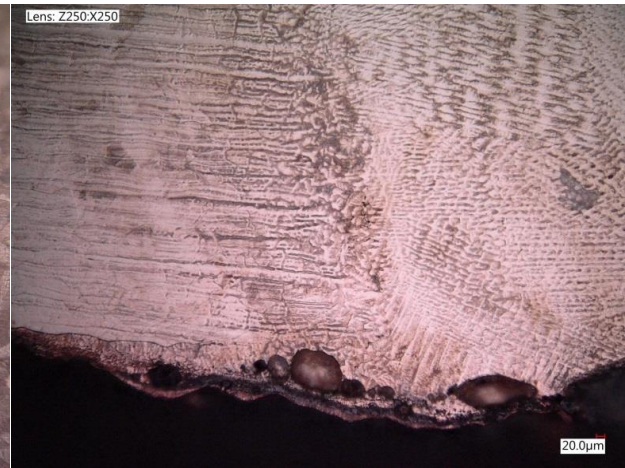
Figure 36: Sample welded without backing gas, top of weld (bottom in the image). Etched for 10s. Micro-segregation can be seen in the weld as well as the pores at the back side of the weld.

Figure 37: Sample welded with backing gas, HAZ on weld section. Etched for 10s. The weld zone on the right goes over in the HAZ on the left.
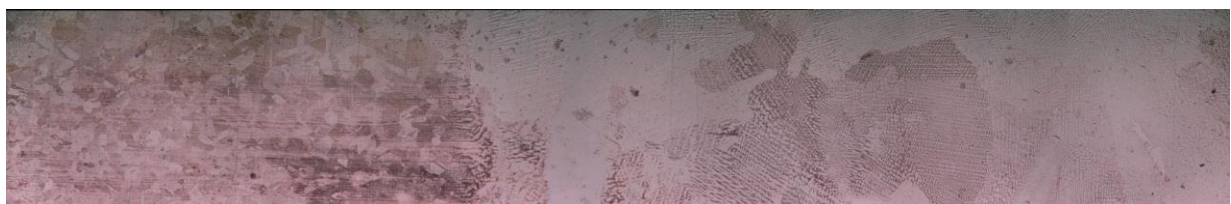
Figure 39: Overview of stitched images starting at the right with the weld zone and continuing into the base material. Same sample as Figure 44.

Figure 38: Overview of stitched images starting at the right with weld zone and continuing into the base material. Sample welded without backing gas. In comparison with Figure 47 there is fewer weld material shown.

Since the samples were cut in three areas to be able to fit in the microscopes it is important to note the designation of each part. As stated before the area here listed as weld (W) consists of the weld and microstructural HAZ, as well as part of the visual HAZ. For the determination of the grain areas only the HAZ is counted since the weld showed a fully cellular-dendritic structure. The area designated with H consists of the visual HAZ and the base material (B) consists of the material found furthest away from the weld. The sections are then designated as follows:

- Base material welded with backing gas (BB)
- Visual HAZ welded with backing gas (HB)
- Weld and part of visual HAZ (for grain area determination only HAZ) welded with backing gas (WB)
- Base material welded without backing gas (BNB)
- Visual HAZ welded without backing gas (HNB)
- Weld and part of visual HAZ (for grain area determination only HAZ) welded without backing gas (WNB)

Besides the weld zone, which shows a cellular-dendritic cast structure, the material consists of a uniformly distributed sizing of crystals with an average grain size area of around 2000 μm^2 as can be seen in Table 11. The grain area frequency plots shown in Figure 40 to Figure 45 show the distribution of grains of certain areas. The standard deviation is large, this happens because of the large spreading in grain areas as can be seen in the frequency plots. Grain areas of 0 to 99 μm^2 are most found in all samples. The grain areas are counted on a cross section, so therefore sliced grains are counted.

Table 11: Average grain areas and standard deviation of the different sections.

	Mean [μm^2]	σ		Mean [μm^2]	σ
BB	1883.792	2043.715	BNB	2732.471	2144.297
HB	4694.365	3784.258	HNB	2452.205	1812.057
WB	1834.033	1411.817	WNB	2108.771	1573.282
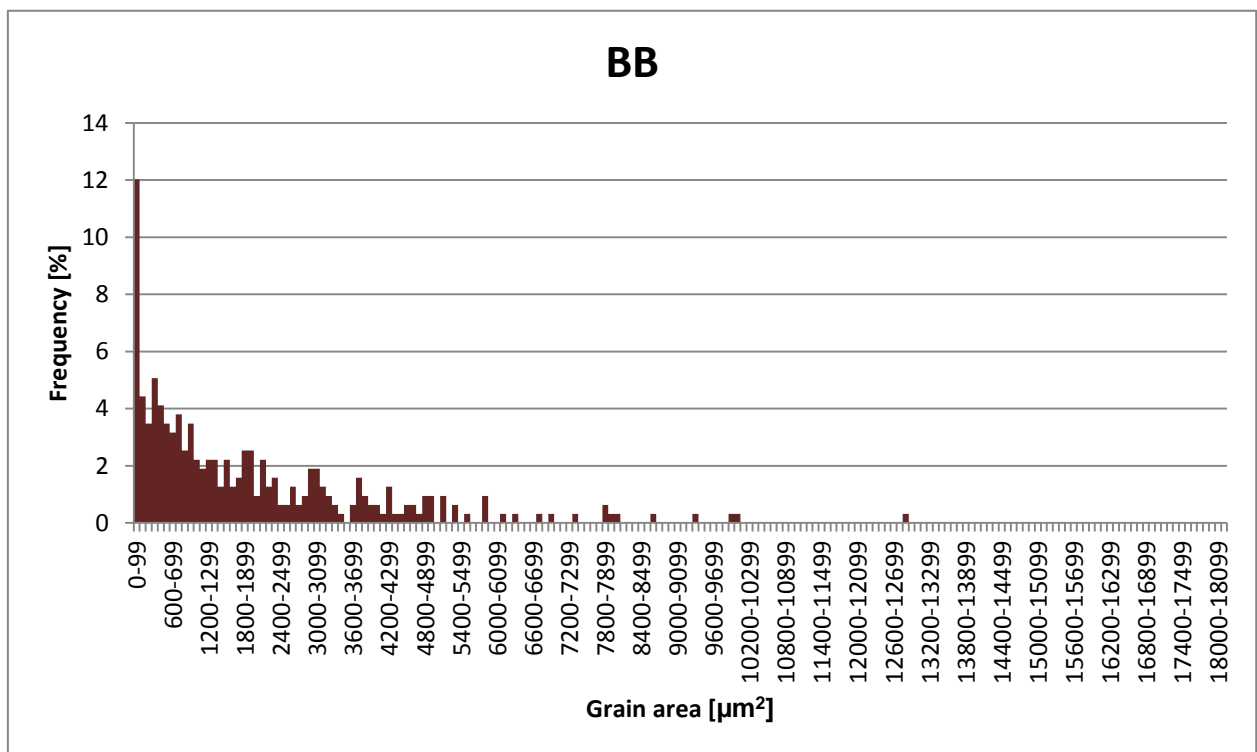
Figure 40: Distribution of grains in sample BB in percentage.
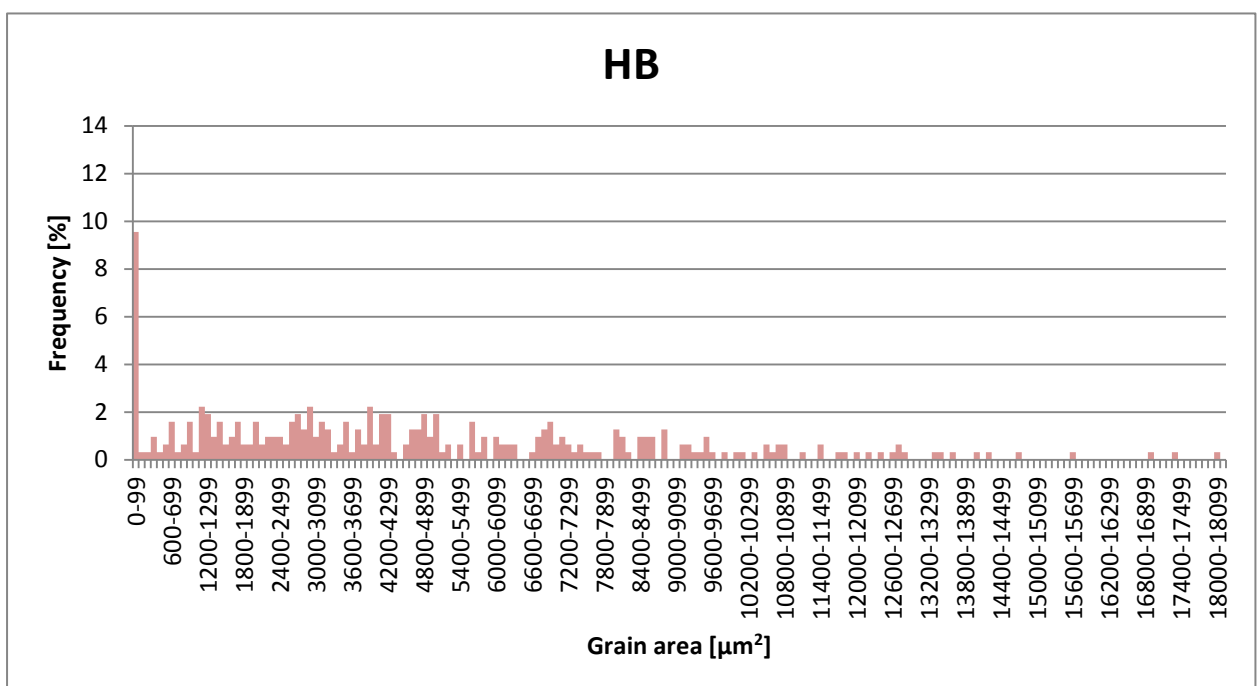
Figure 41: Distribution of grains in sample HB in percentage.
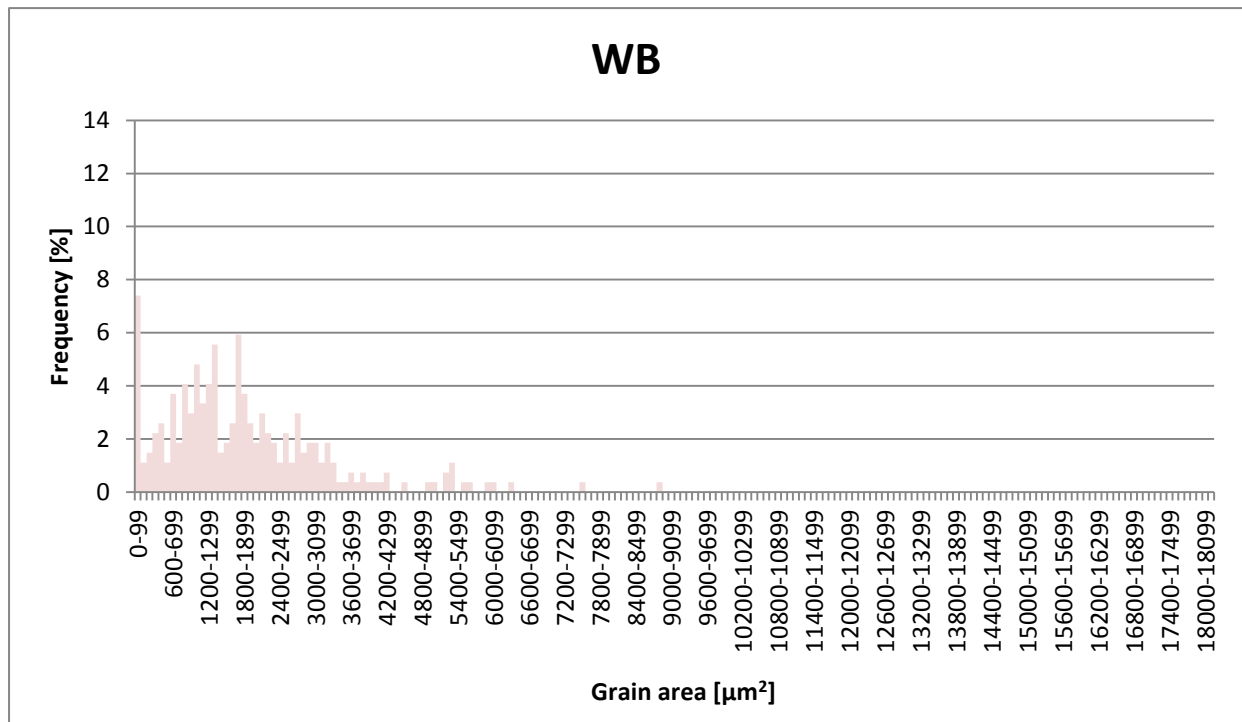
Figure 42: Distribution of grains in sample WB in percentage.
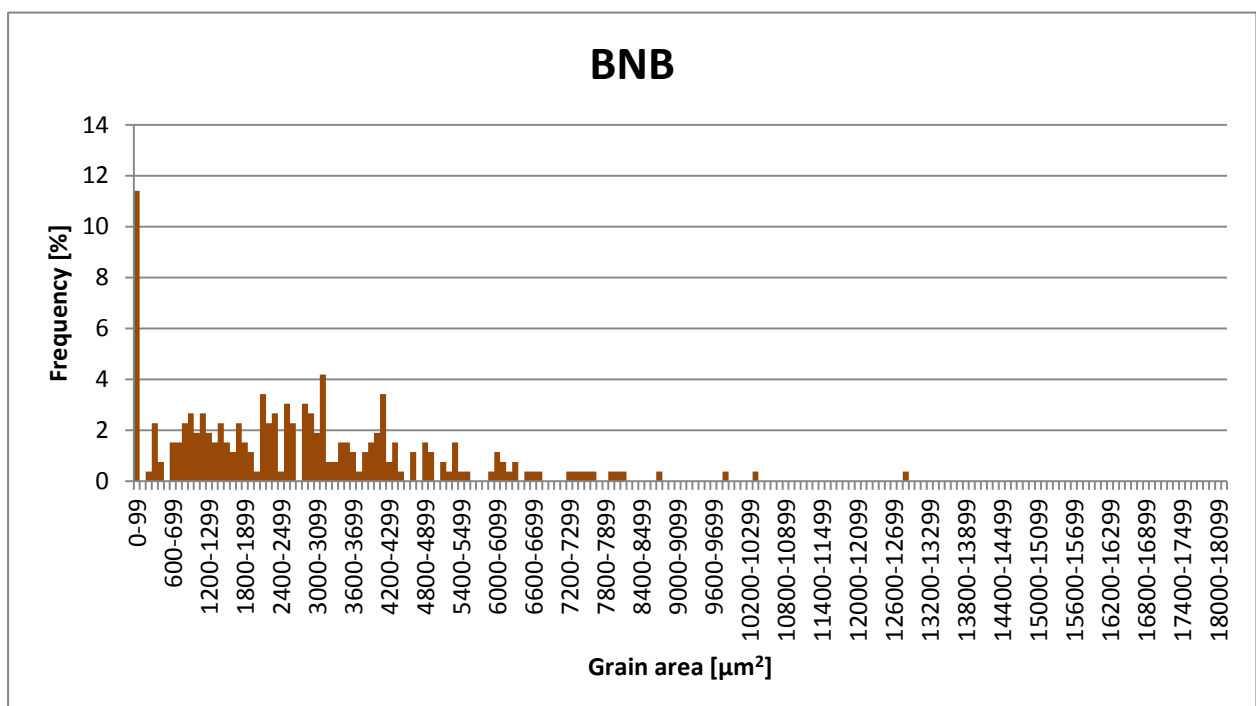
Figure 43: Distribution of grains in sample BNB in percentage
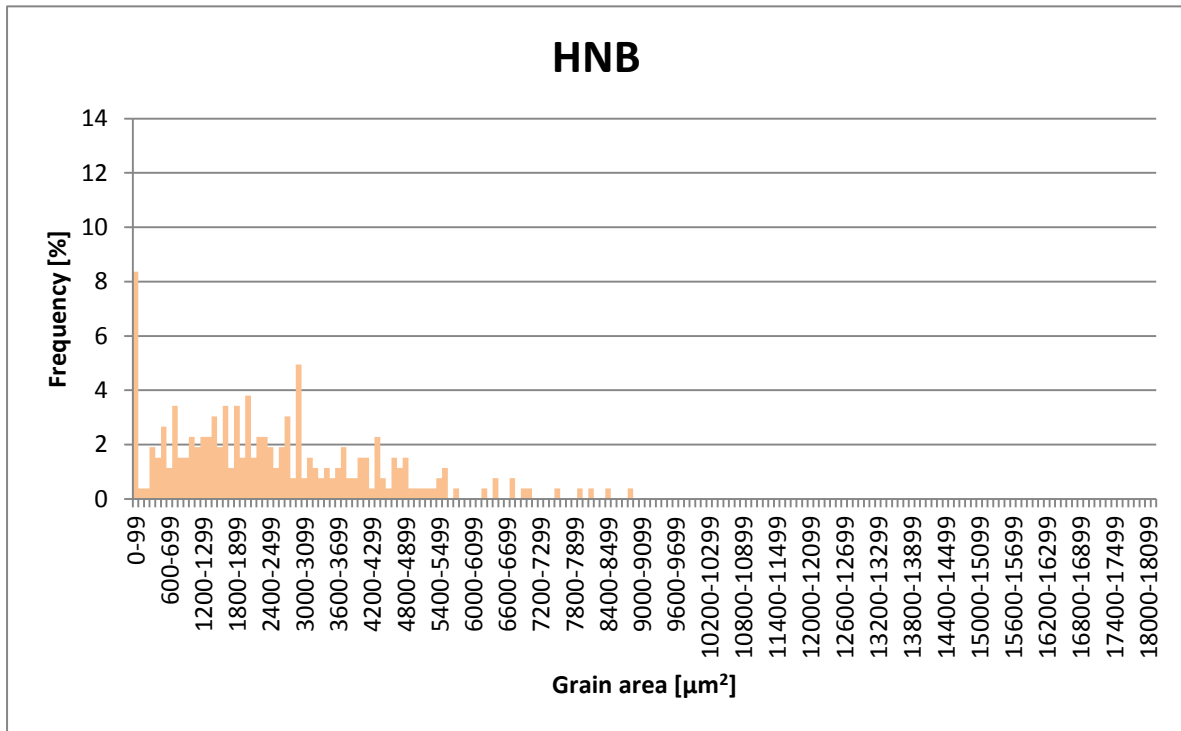
Figure 44: Distribution of grains in sample HNB in percentage.
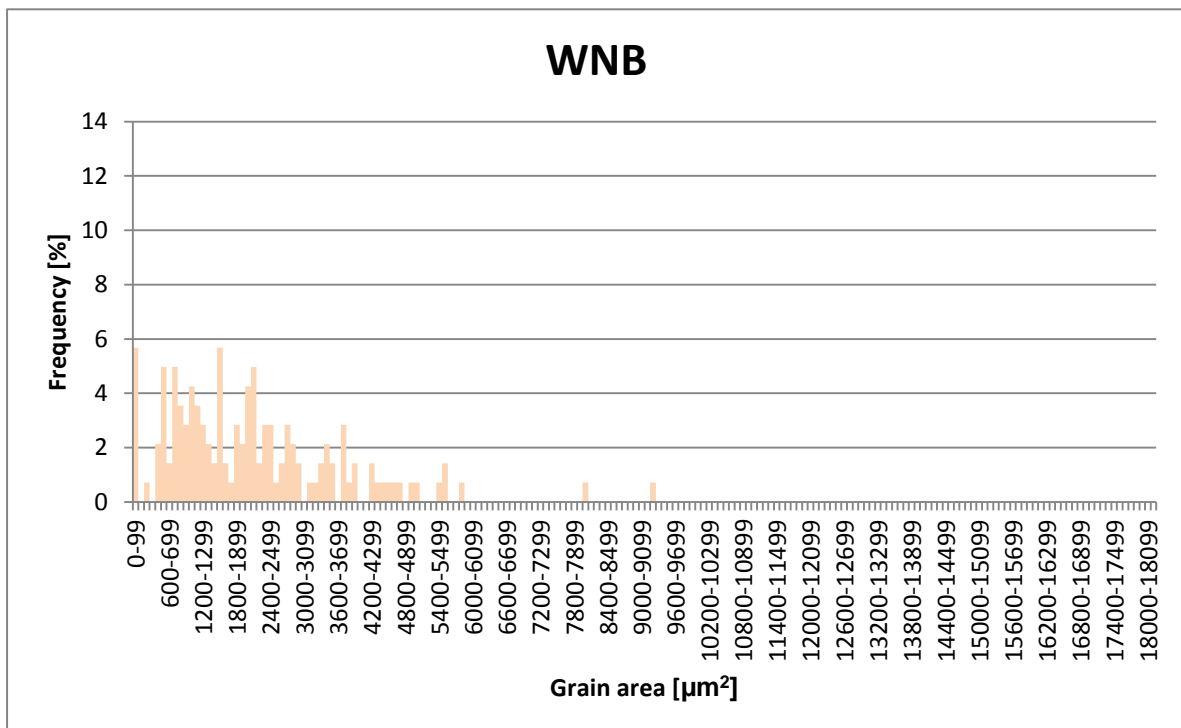
Figure 45: Distribution of grains in sample WNB in percentage.

3.3 Composition analysis of the weld zone and HAZ

The SEM with EDS detector was used to determine the composition of the sections. The results are shown below with BSE images left and the corresponding EDS measurements right. The first measurements were taken from the heated base material section of the weld without backing gas. Measurements were taken from inside the pipe wall, so not close to the surface. The BSE image can be seen in Figure 46. This area was used with the EDS detector and a line of measurements was taken randomly in the grey area.
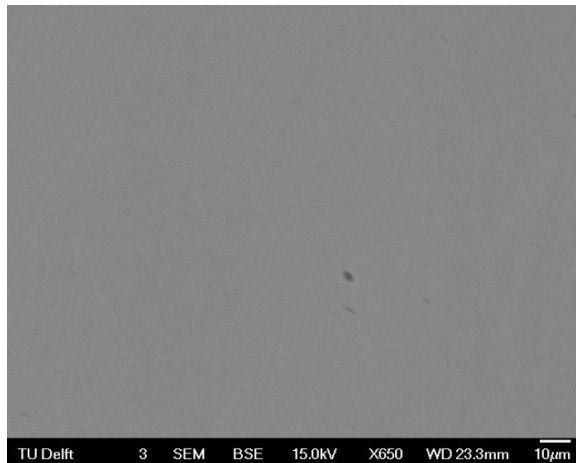
Figure 46: BSE image from area away from the surface of the heated base material welded without backing gas. The image is mostly grey since not much definition is seen between copper, nickel and iron. The spot on the surface was contamination and not embedded into the material.
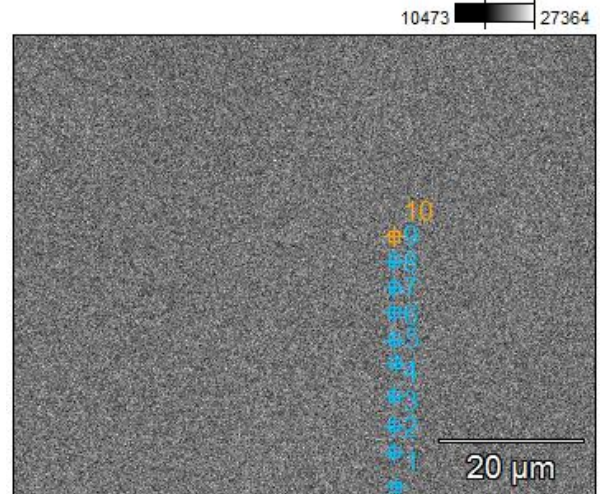
Figure 47: Image used to identify spots of EDS measurements. 10 measurements were taken at a line randomly in the grey area.

Table 12: Weight percent of found elements(with weight error) for the 10 measurements

	C-K	Mn-K	Fe-K	Ni-K	Cu-K
1	0.88±0.05	0.93±0.13	1.84±0.15	9.96±0.60	86.39±1.33
2	0.84±0.06	1.10±0.14	1.63±027	10.35±0.62	86.07±1.34
3	0.88±0.06	0.97±0.14	1.59±0.15	11.26±0.62	85.30±1.36
4	0.73±0.06	0.92±0.13	1.30±0.26	10.31±0.59	86.74±1.31
5	0.81±0.06	1.08±0.13	1.79±0.26	11.12±0.35	85.21±1.29
6	0.84±0.06		1.92±0.27	10.51±0.60	86.73±1.34
7	0.88±0.06	0.90±0.13	1.35±0.15	9.80±0.60	87.07±1.34
8	0.82±0.05	0.87±0.13	2.01±0.27	11.25±0.35	85.06±1.29
9	0.84±0.06	0.82±0.13	1.70±0.15	11.66±0.36	84.97±1.31
10	0.82±0.06	0.79±0.13	1.34±0.26	10.02±0.59	87.03±1.32

Full scale counts: 6886   startHAZ(3)_pt8
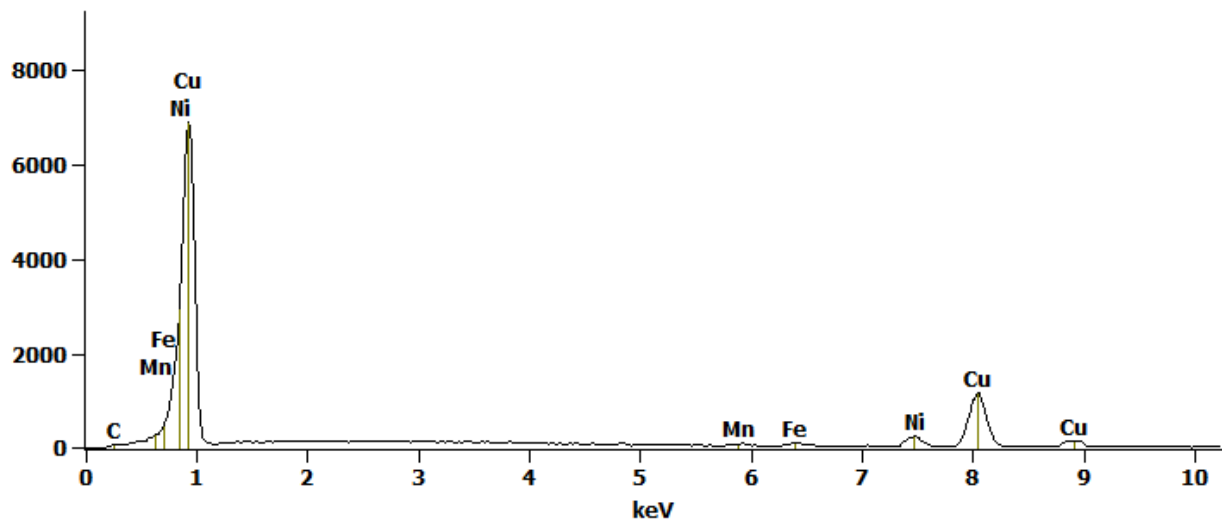
Figure 48: Measurement 8, all measurements on this sample looked very much alike. The first peak of copper and nickel are very similar, with just before that peak iron is identified.

Closer to the surface on the same section other measurements were taken. The results of these measurements are shown in Figure 50 and Figure 49. The measurements were taken from interesting features found in the sample. Point 1 refers to a particle with oxygen and copper as main constituents. This particle is found close to the inner pipe surface. Point 2 mainly consists of carbon and oxygen, while the third particle has a composition close to the weld filler material, even though it was found away from the weld.
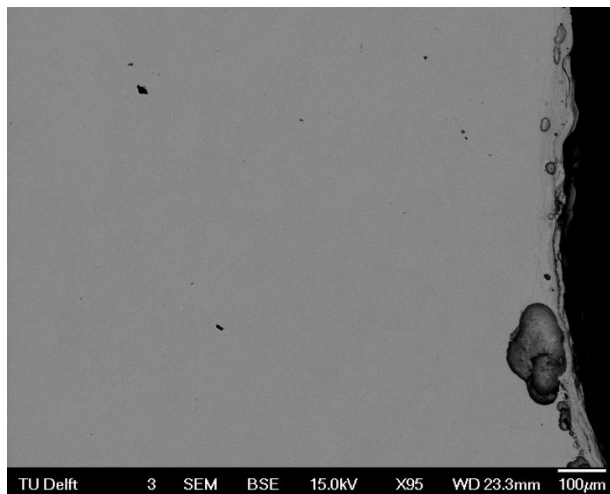
Figure 50: BSE image from area close to the surface (right side) of the heated base material welded without backing gas.
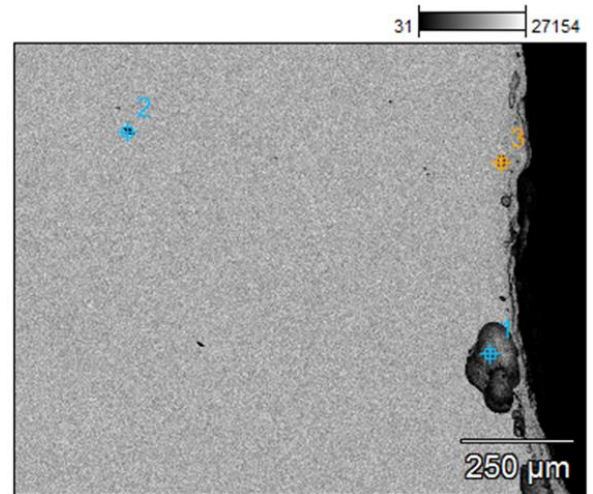
Figure 49: Image used to identify spots of EDS measurements. 3 measurements were taken. The first in the dark grey figure just at the surface, the second point was a dark spot at the left. The third point was taken at the surface of the material.

Table 13: Weight percent of the found elements (with weight error) for the three measurements.

	C-K	O-K	Al-K	S-K	Cl-K	Ca-K	Mn-K	Fe-K	Ni-K	Cu-K
1	4.18±0.45	17.03±0.86	1.13±0.27					7.12±1.04	16.56±2.02	53.99±6.19
2	59.67±0.40	22.43±0.53		2.75±0.17	0.64±0.09	1.28±0.11				13.23±0.84
3	0.58±0.06	1.28±0.09	0.14±0.04				2.29±0.21	6.41±0.52	28.99±1.28	60.32±2.08

The last set of measurements showed similar results indicating that the composition varies little over the different sections and areas. In the weld area macro segregations can be seen were nickel rich and copper rich areas alternate. For the weld without backing gas this is shown in Figure 51 and Figure 52. The nickel rich areas are denoted by numbers 1, 5, and 8, while the copper rich areas are shown at 2, 4, 6, and 7. The nickel rich areas are dark grey in the image, while the copper rich areas are lighter. This segregation was found on the rough weld surface on the inside of the pipe.
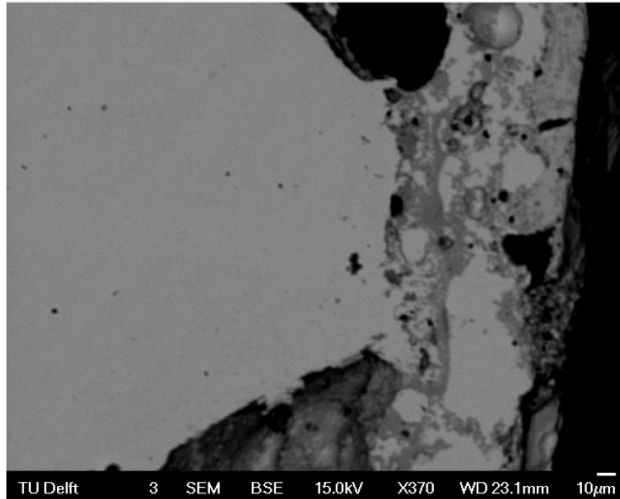
Figure 51: Image used to identify spots of EDS measurements. 8 measurements were taken in different areas close to the surface.
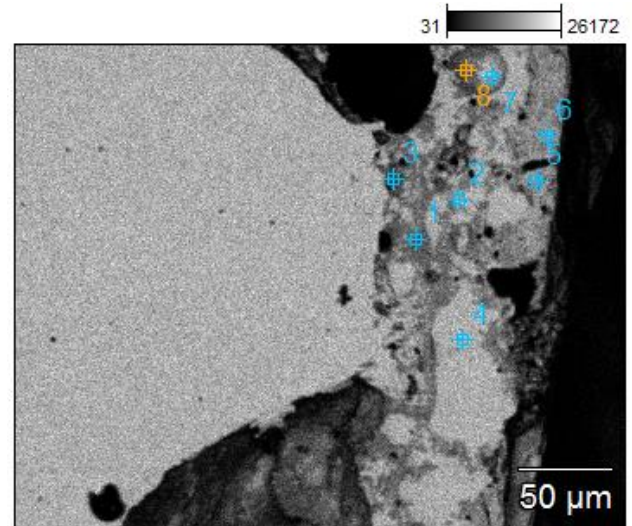
Figure 52: BSE image from the weld area near the surface. Areas of less and more intensity alternate in the top layer.

Table 14: Weight percent of the found elements (with weight error) for the eight measurements.

	C-K	O-K	F-K	Al-K	Mn-K	Fe-K	Ni-K	Cu-K
1	0.86±0.07	19.09±0.27			8.59±0.39	17.11±0.49	54.35±0.99	
2	2.37±0.09	0.07±0.08		0.12±0.04		0.76±0.13	1.82±0.24	94.86±1.30
3	1.34±0.06	19.53±0.29	1.13±0.88		24.30±0.54	40.31±0.69	6.66±±0.33	6.73±0.42
4	1.58±0.08	0.37±0.08						98.04±1.33
5	1.19±0.08	13.29±0.21					54.07±0.98	31.45±1.23
6	1.72±0.07	8.31±0.19					1.76±0.24	88.21±1.31
7	2.90±0.10	2.46±0.19					2.54±0.25	92.10±1.28
8	2.47±0.11	0.77±0.07		0.12±0.03		1.37±0.19	81.11±1.58	14.16±1.61

3.4 Surface potential over the weld, HAZ and base metal

The differences in surface potential of the four samples are represented in graphs (Figure 55 to Figure 58) below. A SKP measurement was taken every 0.7 mm. For all graphs the x-axis states the location of the measurement on the sample. As reference is taken the middle of the weld as 0 and the positive direction is as shown in Figure 53. For all samples discoloration of the sample as a result of welding occurred until approximately 40 mm away from the middle of the weld. Measurements stopped at approximately 70 mm away from the weld due to restraints in the SKP set-up. The graphs in the following figures represent the position on the sample along the x-axis. The surface potential as measured by the SKP is shown on the y-axis.
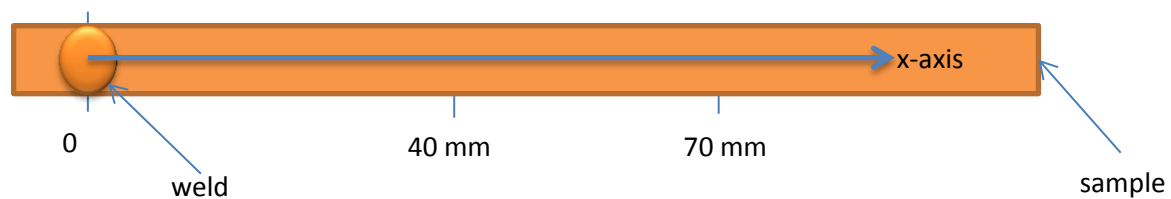
Figure 53: Schematic of reference axis and approximate sizing. The x-axis has its origin at the centre of the weld. Discoloration of the surface is present up to 40 mm away from the weld. Measurements continued to 70 mm away from the centre of the weld.
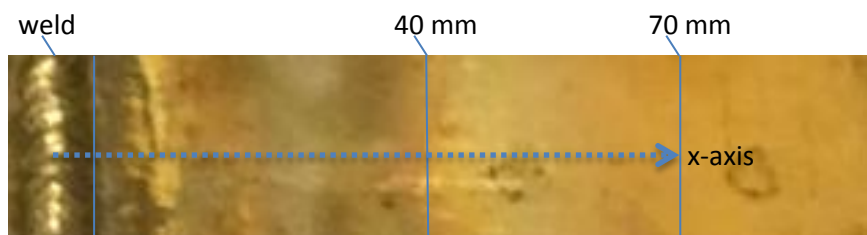
Figure 54: photo of weld and discoloration. Weld shown at left side of sample, discoloration can be seen up to 40 mm away from the middle of the weld.

The samples are designated as follows:
B: welded with backing gas, no SDMC treatment (Figure 55);
BS: welded with backing gas, with SDMC treatment (Figure 56);
NB: welded without backing gas, no SDMC treatment (Figure 57);
NBS: Welded without backing gas, with SDMC treatment (Figure 58).
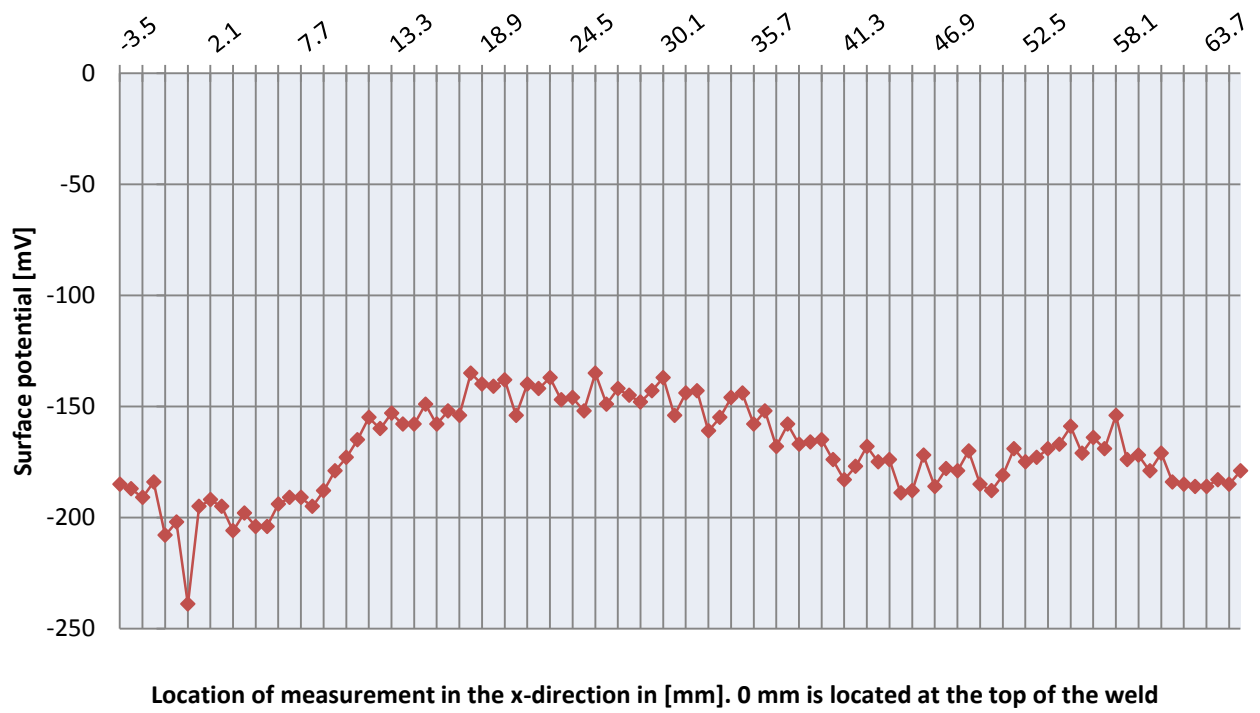
Figure 55: Work function over the surface of sample B
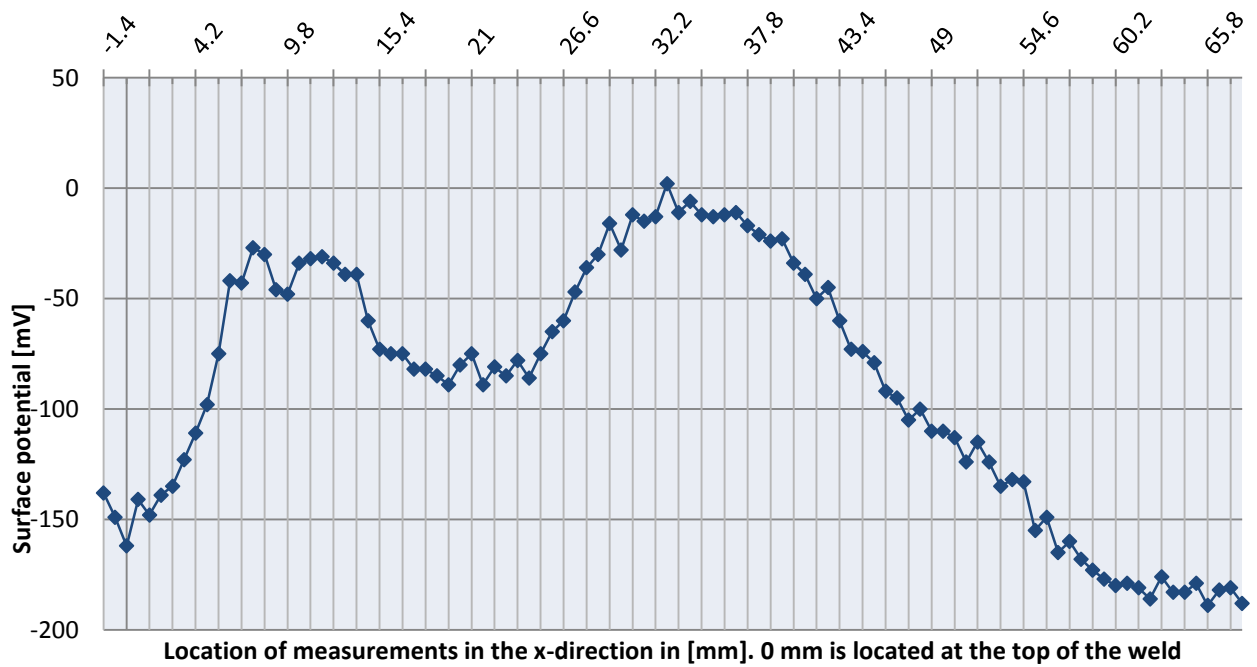
Figure 56: Work function over the surface of sample BS
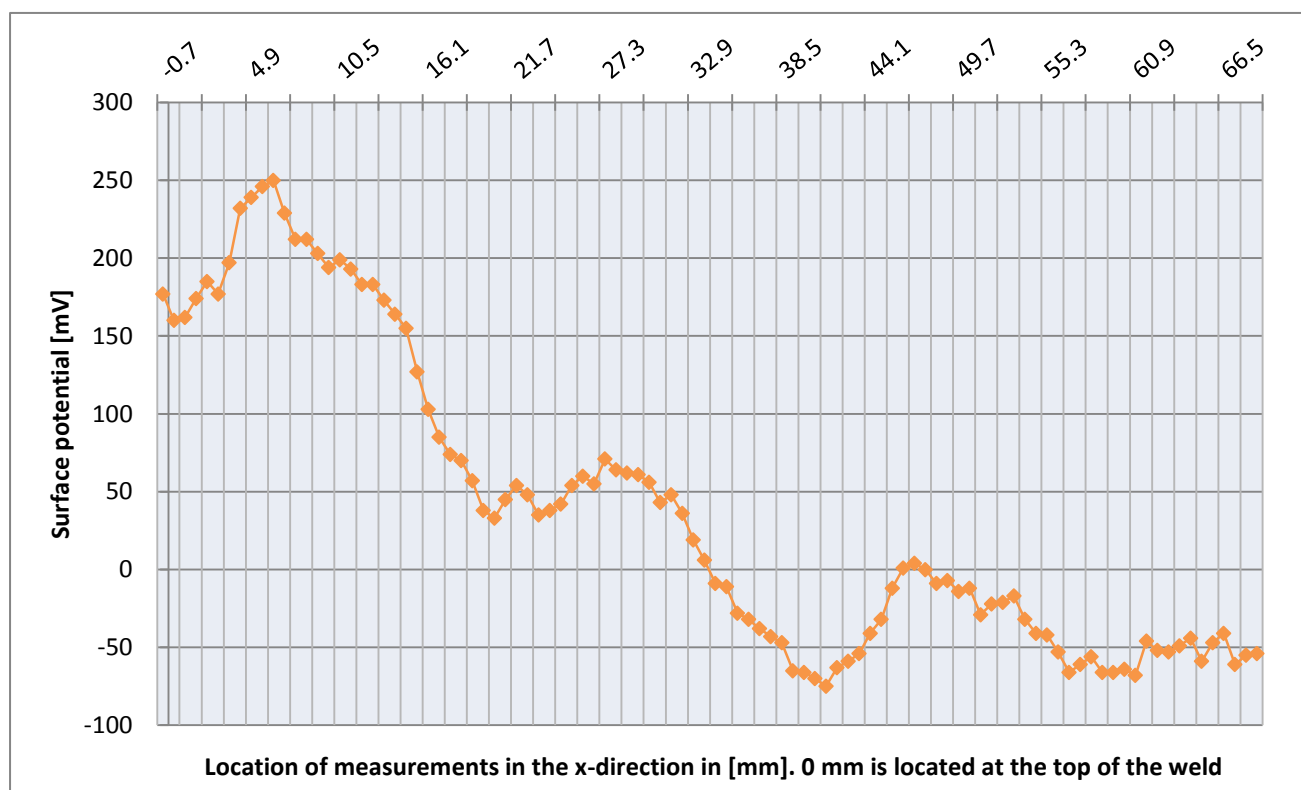
Figure 57: Work function over the surface of sample NB
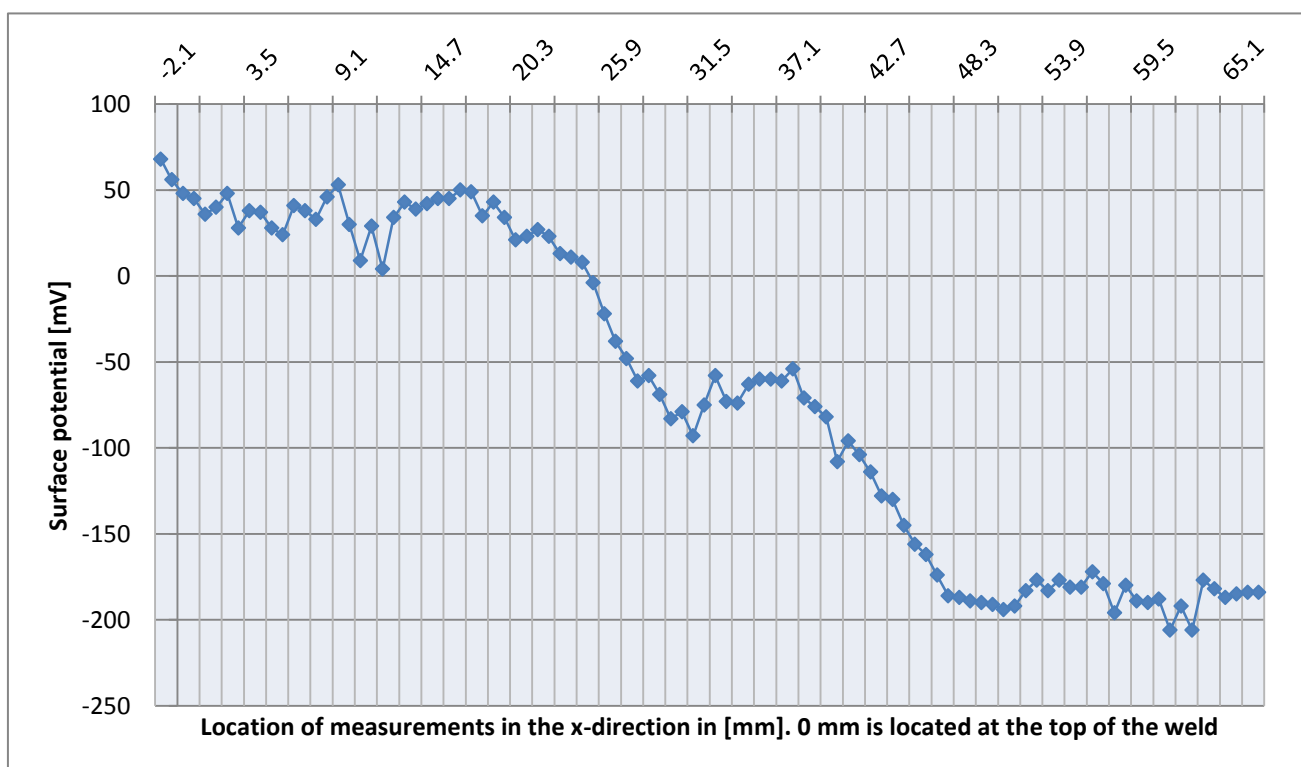
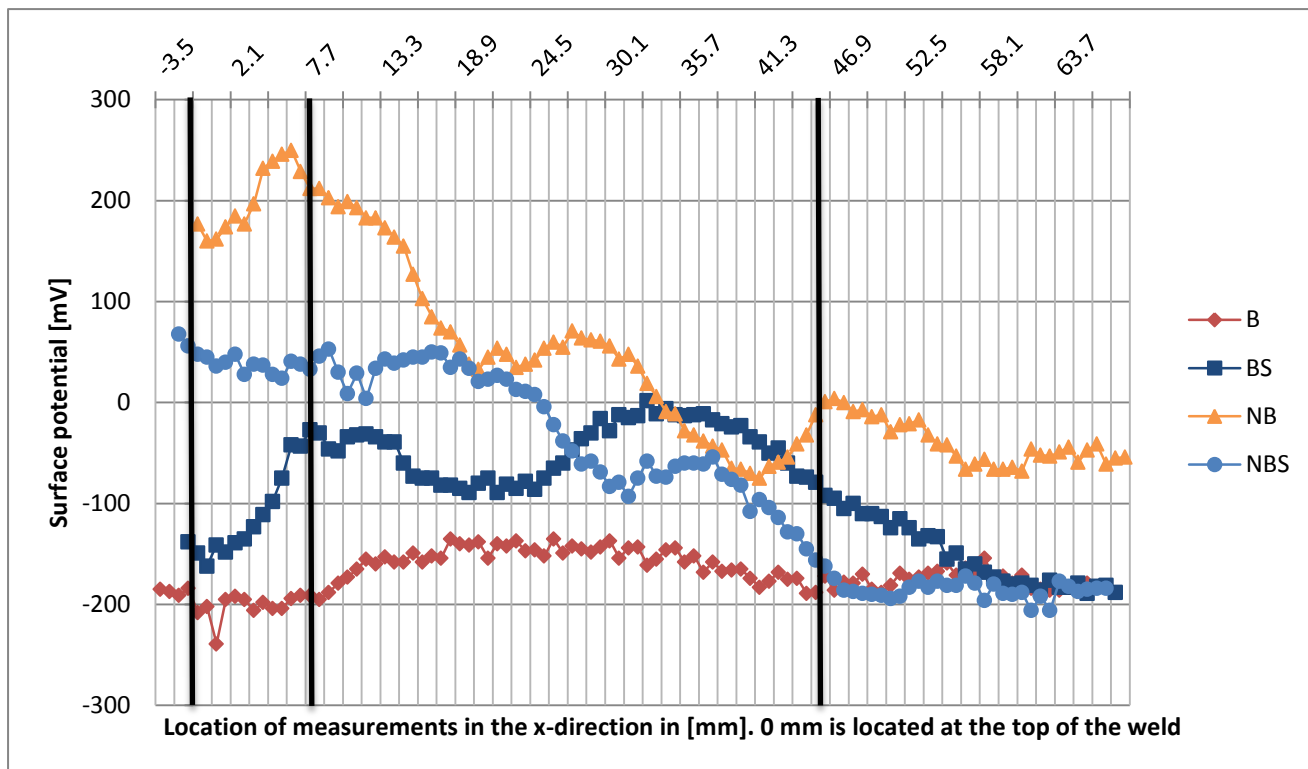Figure 58: Work function over the surface of sample NBS

Figure 59: Combined graph of the four potential measurements. From 8 mm away from the weld the measurements are more precise due to height differences in the weld area. After 45 mm no discolorations are found on the samples anymore.
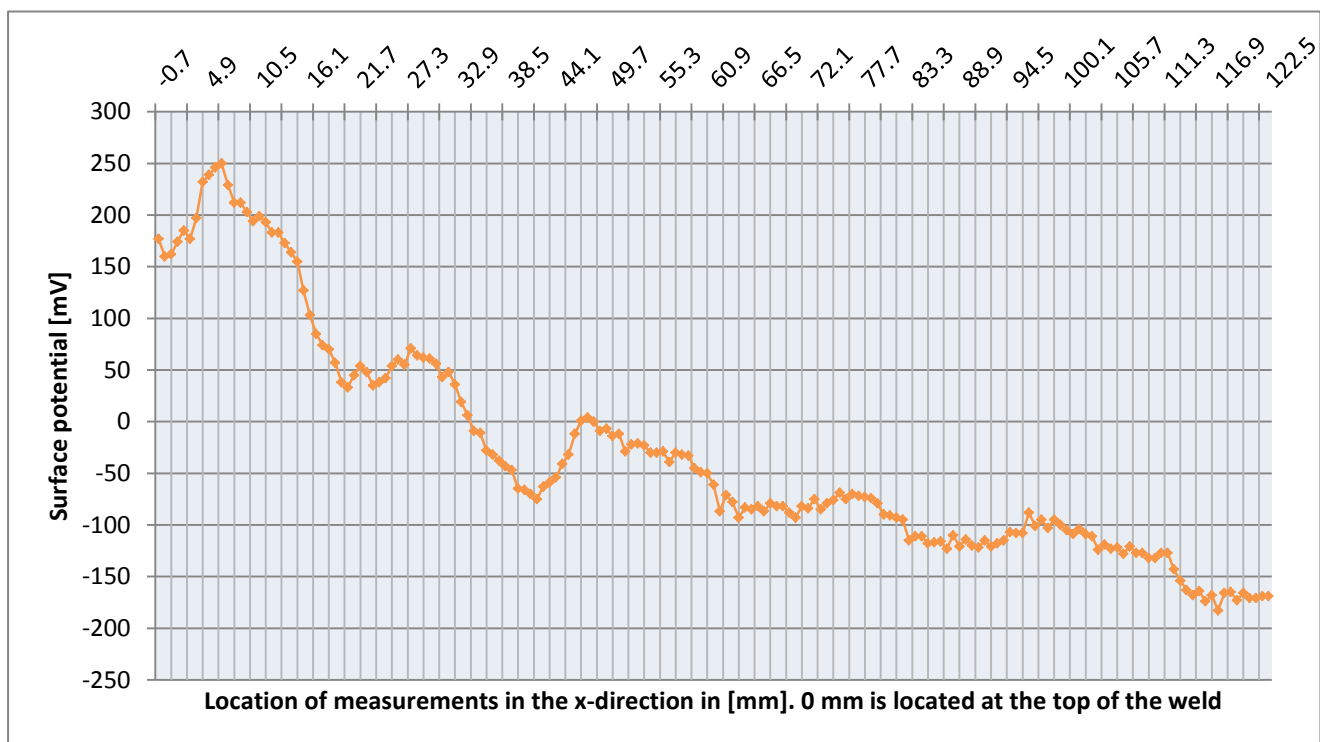
55

Figure 60: Surface potential over the surface of sample NB, combination of 2 measurements.

The sample welded with backing gas (B) displays values between -200 and -150 mV of the work function. The sample welded without backing gas (NB) starts around +250 and goes down to -50 mV at 70 mm away from the weld region. Further investigation (shown in Figure 60) revealed that for this sample eventually a stable value between -200 and -150 mV is reached. The sample welded with backing gas and protected with SDMC (BS) shows more variation in the work function compared to its counterpart without SDMC protection, but results in a relative stable part between -150 and -200 mV. The fourth sample, welded without backing gas and protected by SDMC (NBS) reveals a steady diminishing work function which becomes stable around -150 to -200 mV. The combined graph in Figure 59 shows all four measurements at once. The first black line is set at 0 mm, the centre of the weld. The second black line is located at 8 mm away from the weld and the last black line at 45 mm way from the weld, in the region between the weld and that line there was discoloration present on the surface (visual HAZ). Sample NB was investigated going further along the x-axis to investigate whether the work function eventually also would go down to between -150 and -200 mV. As can be seen in Figure 61 it appears that also this sample eventually reaches the same work function value as the other samples. Figure 61 is acquired by combining the first measurement and a second measurement of again 100 steps of 0.7 mm starting at 61.6 mm away from the weld.

The measurements of the potential are dependent on the distance between the probe and the surface. Since these are inversely proportional to the potential gradient, this gradient is a measure of the distance between probe and surface. As stated before the gradient was set at 299, but it can vary during the measurements due to changes in the height of the sample. Especially in the weld area the height changes were difficult to compensate and as can be seen in Figure 61 the gradient varied in the first 8 mm from the centre of the weld. This results in the first 8 mm of the potential measurements to be less accurate, since comparisons of measured potentials can only be made if the distance from probe to surface was equal. The rest however shows a steady gradient since here there were no more height differences. In the graph 8 mm from the centre of the weld is indicated with a black line for clarification.
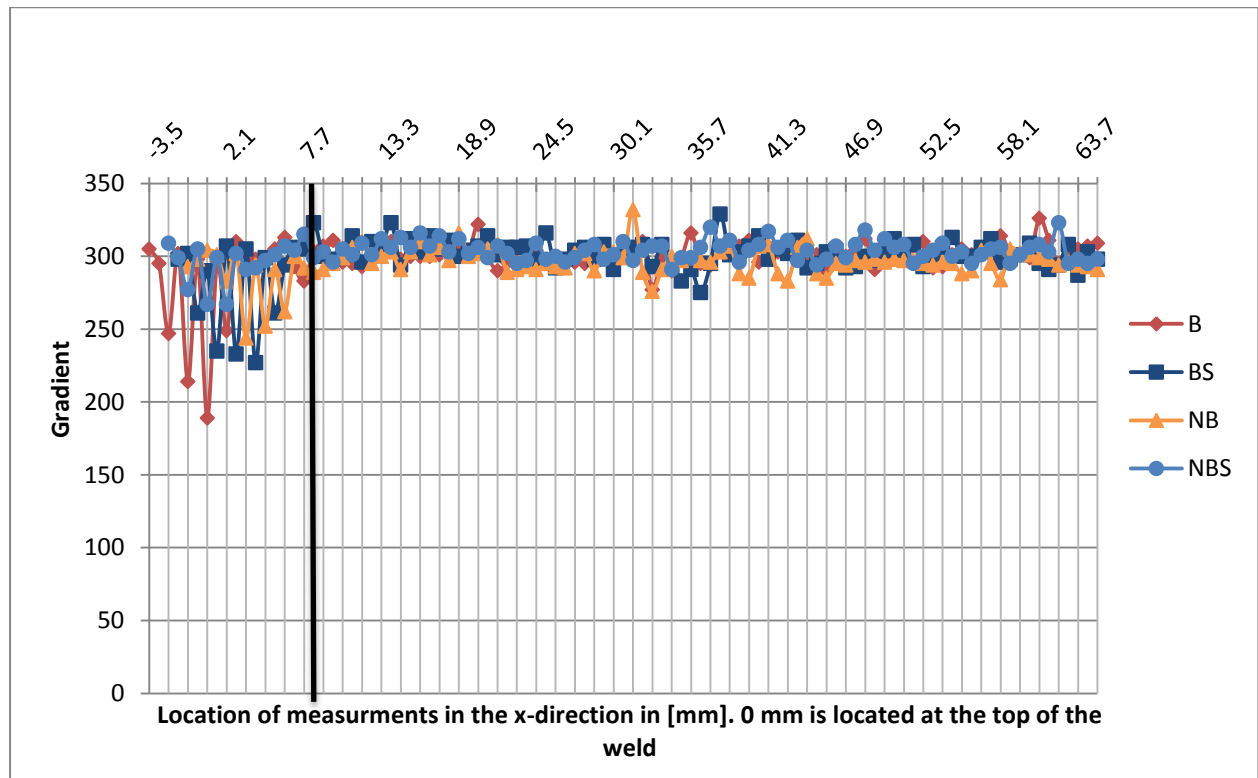
Figure 61: Combined graph of the four gradient measurements. Up to 8 mm away from the weld the gradient varies. This is due to the height differences in the weld which could not be compensated completely by the system.

3.5 Natural degradation of the CuNi10Fe samples

3.5.1 Immersion test in 3.4 wt% NaCl
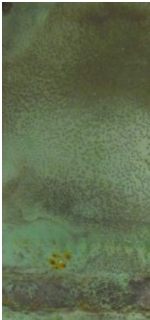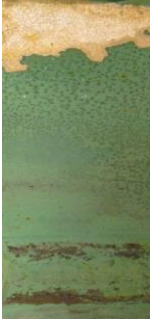
The immersion test in 3.4 wt% NaCl took 5 weeks. Already after one day green corrosion products started to accumulate in the pores of the weld without backing gas. On a lesser extent this was also 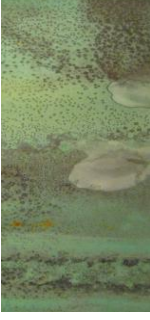the case for the sample also welded without backing gas, but protected by SDMC. Both samples with backing gas showed no sign of corrosion. After two days the samples welded without backing gas were covered with green residue at some places near the discoloration and base material. The results after 2, 10, 28 and 36 days of immersion are shown in Table 15.

After six days also the samples welded with backing gas showed green discoloration. For the sample protected with SDMC the green residue was mainly present in the HAZ, for the unprotected sample the discoloration was more present at the base material. Also orange dots started to appear in the HAZ. The orange dots are best visible after 28 days of immersion for the samples protected with SDMC.

After ten days of immersion the samples were taken out and dried a little to see how attached to the surface the green residue was. This revealed also that areas that appeared not attacked in the solution did show discoloration when dried. Even after 28 days a band was visible where fewer corrosion products formed about 10 mm away from the weld. This band was less apparent with the samples welded without backing gas. The sample welded without backing gas with SDMC protection was scratched at one of the orange spots. The orange spots were not loosely attached, but firmly remained on the surface when scratched.

After 36 days the test was stopped. The samples were taken out of the solution again, rinsed with demi water and dried. The bands were still visible and the green corrosion layer was thickened. While rinsing some of the green corrosion on the sample welded without backing gas and SDMC came off, revealing a fresh surface.

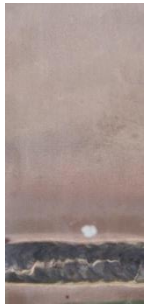**Table 15: Overview of immersion results for the four samples after 2, 10, 28, and 36 days of immersion.**
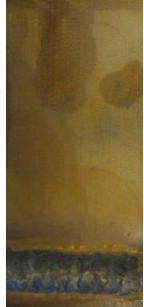
	2 days of immersion	10 days of immersion	28 days of immersion	36 days of immersion
Backing gas, no SDMC				
Backing gas, SDMC				
No backing gas, no SDMC				
No backing gas, SDMC				

3.5.2 Immersion tests in sulphide containing 3.4 wt% NaCl

Both tests in contaminated water revealed a shiny surface after one day, including the samples with the SDMC coating. Especially the area right next to the weld became very reflective. After two days the solution with the samples welded without backing gas turned green. Due to time restraints the samples in the second series were removed from the solution after 4 days. After rinsing and drying the samples still exhibited a metallic shine right next to the welds in all samples. Also in the HAZ of the sample welded without backing gas, coated with SDMC appeared some green corrosion product.

After 6 days of immersion, corrosion products appeared on all samples. An overview of the samples after immersion for 1, 4, and 6 days is shown in Table 16.

Table 16: Overview of immersion results for the four samples after 1, 4 and 6 days of immersion.

	1 days of immersion	4 days of immersion	6 days of immersion
Backing gas, no SDMC			
Backing gas, SDMC			
No backing gas, no SDMC			
No backing gas, SDMC			

3.6 Electrochemical characterisation of CuNi10Fe samples in 3.4 wt% NaCl solution

Electrochemical polarization test were performed to be able to compare the initial current densities of the different samples. Polarization curves were made for all samples. Representable polarization curves for each experiment are shown in Figure 62 to Figure 65. For clarity labels on the x and y axis are not shown. On the x axis the current density i_{corr} is shown in [A/cm^2], on the y axis the potential is shown in [V] (versus SCE).
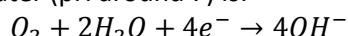
A polarization curve can be divided in different regions. At the point with the lowest i_{corr} the natural occurring E_{corr}, the steady state corrosion potential, can be found, for this material typically around -0.2 V. The bottom curve depicts the cathodic reaction where oxygen is reduced. The predominant reduction reaction in aerated seawater (pH around 7) is:
$$O_2 + 2H_2O + 4e^- \rightarrow 4OH^-$$
The pH of the solution was measured before experimenting and a neutral pH of 7 was confirmed. The shape of the cathodic part of the polarization curve is determined by the oxygen concentration. A lack of oxygen means that the reaction cannot occur any faster and would result in a straight line down at a constant i_{corr}. An abundance of oxygen would result in the ideal curves seen in section *2.6 Electrochemical polarization tests.* The curves seen in the figures show a combination. The part just below steady state corrosion potential shows the i_{corr} when the concentration of oxygen is still sufficient. However the steep part following shows the behaviour typical for a reduction reaction with not enough oxygen present close to the surface of the metal to follow up the reaction. The first part is used in determining the combined i_{corr}.

In the anodic part the dependency on concentration should not be a problem. In this reaction the metal is oxidized. The anodic part of the curve shows two regions. The first region shows the active dissolution of copper. In this region the tangent is drawn to determine the steady state current density. The second region is the passivation region. Around 0 V a sudden reduction in current density is found as can be seen in the polarization curves. 0 V vs SCE therefore is the primary passive potential Epp. Above Epp the passive film becomes stable and protects the metal. This can be seen in the plot because here the current density does not increase anymore. The current density at Epp for all plots falls around 10^{-3} A/cm^2.

Figure 62: Whole region polarization curves for the four different experiments in 3.4 wt% NaCl. For each type of sample one representative curve is shown.
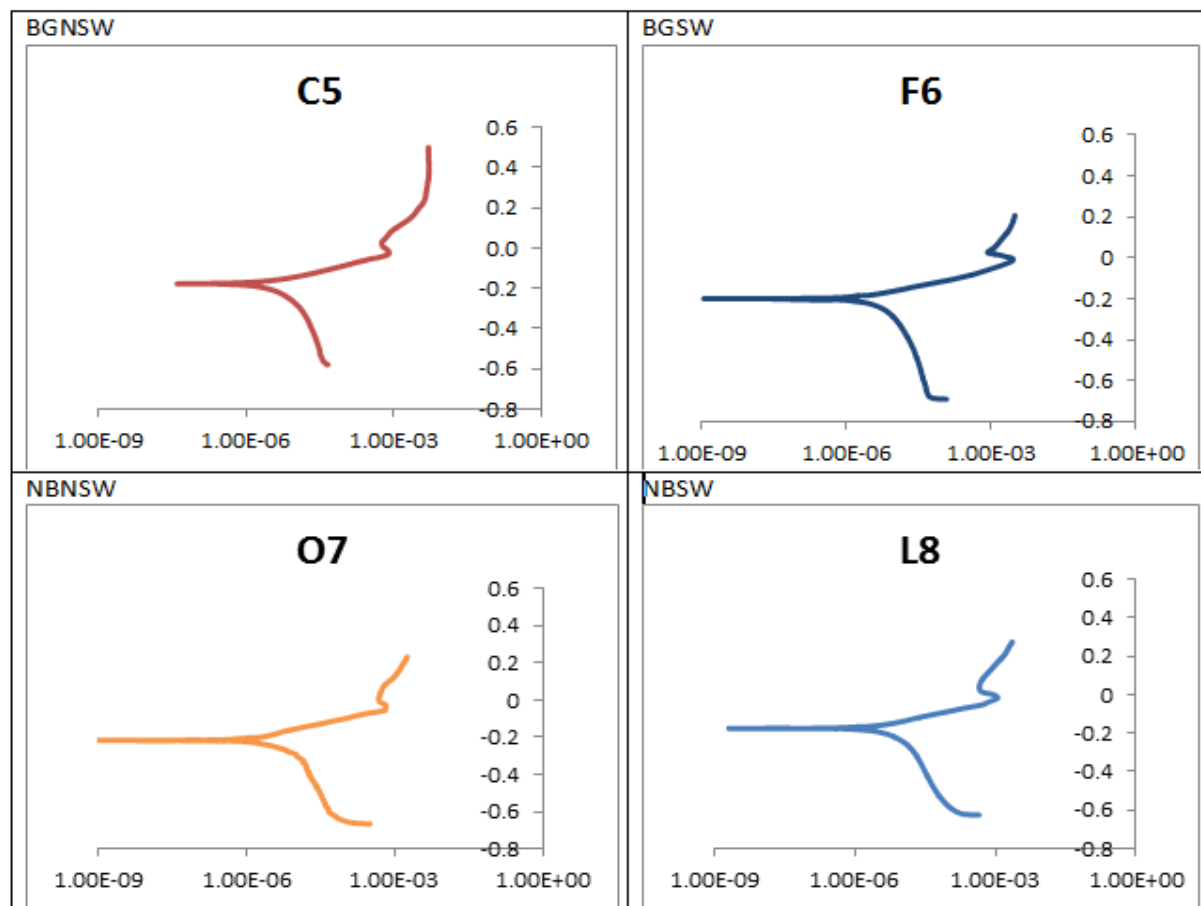
Figure 63: Weld zone polarization curves for the four different experiments in 3.4 wt% NaCl. For each type of sample one representative curve is shown.

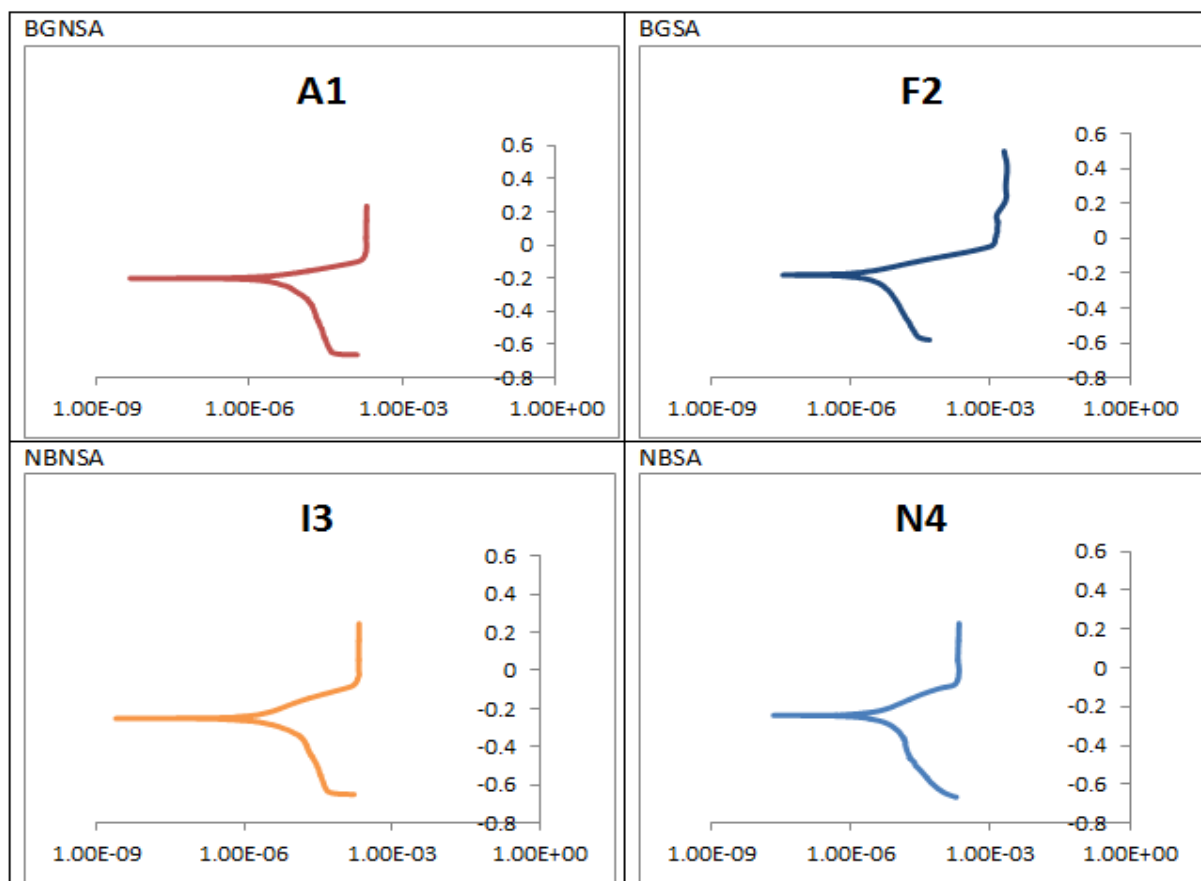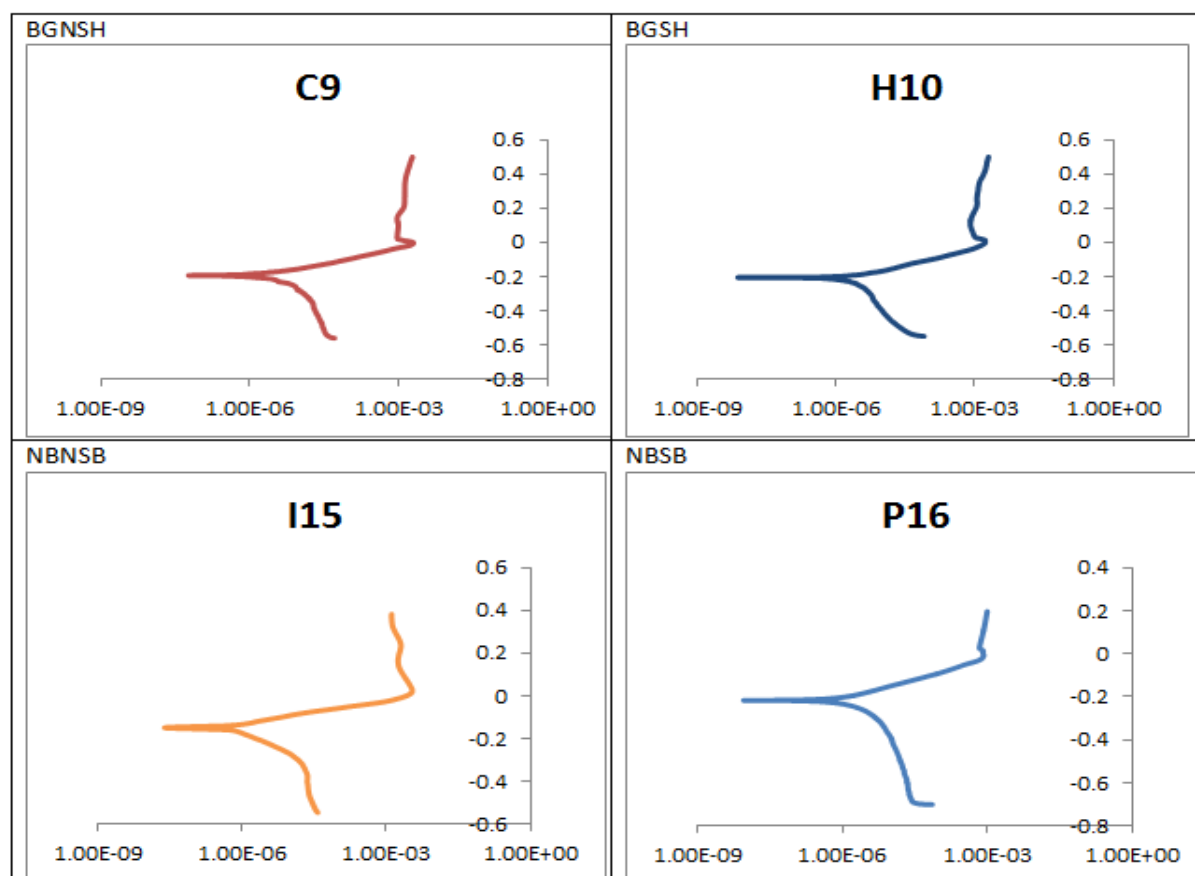**Figure 64: HAZ polarization curves for the four different experiments in 3.4 wt% NaCl. For each type of sample one representative curve is shown.**
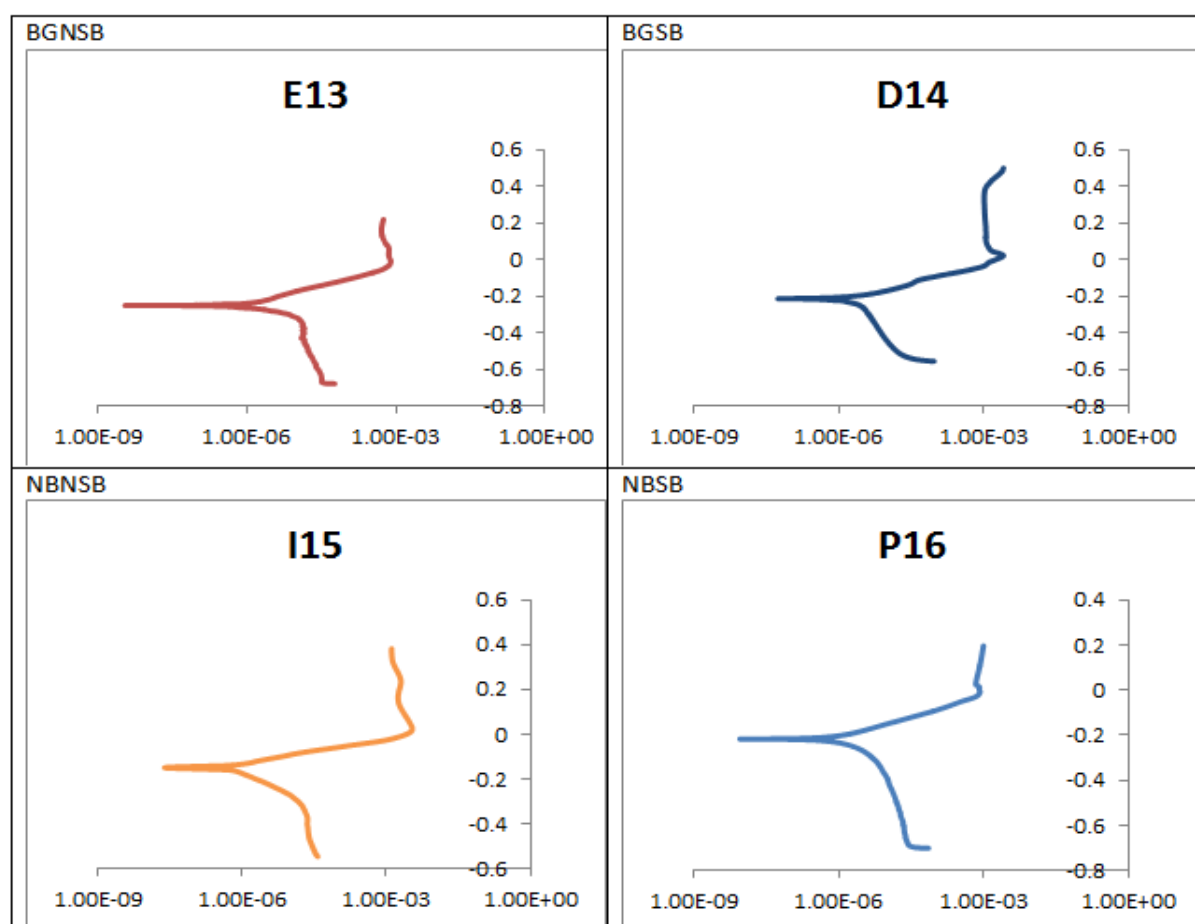
Figure 65: Base metal polarization curves for the four different experiments in 3.4 wt% NaCl. For each type of sample one representative curve is shown.

The polarization tests with 3.4 wt% NaCl each resulted in a graph of the current versus the potential (see Figure 66. The graphs were corrected for the measured surface area to get the current density (in A/cm^2). From this graph the i_{corr} and E_{corr} were calculated. This was done by expanding the apparent Tafel region at the anodic part of the curve and drawing a tangent on the cathodic part. At the cross section of both lines the i_{corr} and E_{corr} were determined. This was repeated for all samples. Since every kind of experiment was repeated four times the average was determined for the i_{corr} and E_{corr} per type of experiment. The different types of experiments are shown in Table 17.

Table 17: List of experiment designations for the polarization tests

	Backing gas/No backing gas	Treatment	Region
BGNSA	Backing gas	No SDMC	Whole region
BGNSB	Backing gas	No SDMC	Base material
BGNSH	Backing gas	No SDMC	HAZ
BGNSW	Backing gas	No SDMC	Weld zone
BGSA	Backing gas	SDMC	Whole region
BGSB	Backing gas	SDMC	Base material
BGSH	Backing gas	SDMC	HAZ
BGSW	Backing gas	SDMC	Weld zone
NBNSA	No backing gas	No SDMC	Whole region
NBNSB	No backing gas	No SDMC	Base material
NBNSH	No backing gas	No SDMC	HAZ
NBNSW	No backing gas	No SDMC	Weld zone
NBSA	No backing gas	SDMC	Whole region
NBSB	No backing gas	SDMC	Base material
NBSH	No backing gas	SDMC	HAZ
NBSW	No backing gas	SDMC	Weld zone
BGNSP	Backing gas	No SDMC	Polished
NBNSP	No backing gas	No SDMC	Polished

Figure 66: One of the polarization graphs (from sample P.4.4) with the tangent lines used to determine i_{corr} and E_{corr}. In red the tangent lines are drawn and the determination of the current density and corrosion potential is shown.
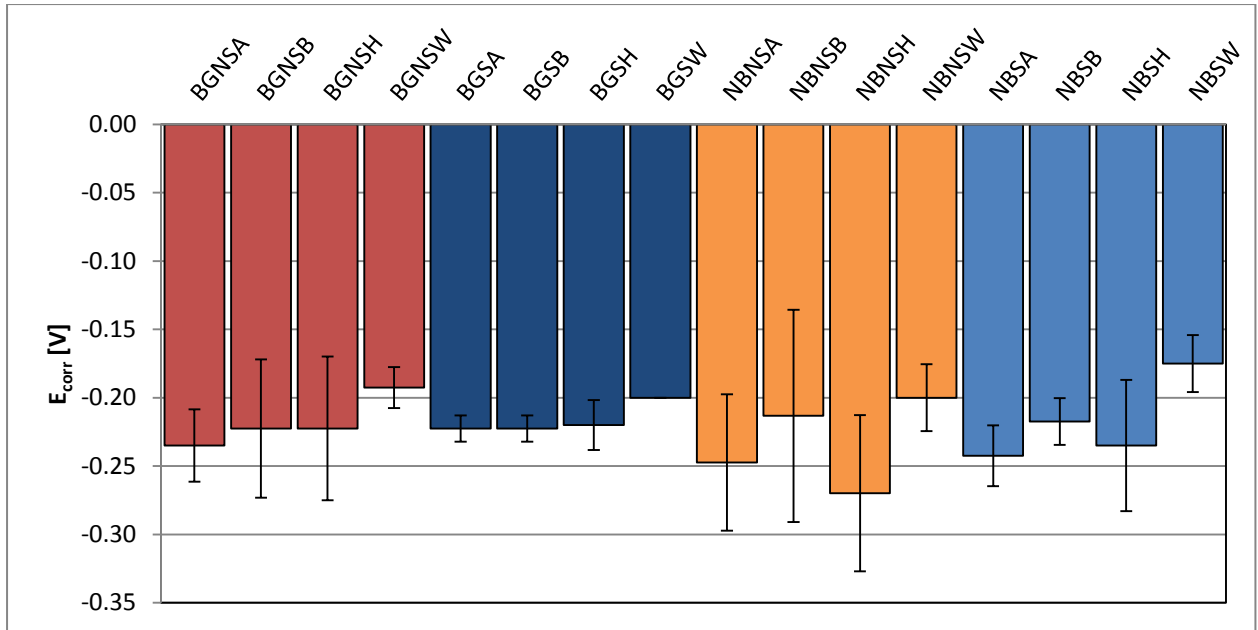
Figure 67: E$_{corr}$ per type of experiment. The values are the averages of four repetitions over different pipe segments. No significant variation is seen.

The E$_{corr}$ calculated for all the experiments varied little as can be seen in Figure 67. The E$_{corr}$ values for all experiments fall between 0.18 and 0.27 V. The average i$_{corr}$ values per type of experiment are shown in Figure 68 .

Figure 68: i$_{corr}$ values per experiment type. The values are the average of four repetitions over different pipe segments. The current density increases from the base material to the weld zone. The standard deviation is shown in black error bars.

Experiment	i_{corr} [A/cm2]	$\sigma(i_{corr})$	E_{corr} [V]	$\sigma(E_{corr})$
BGNSA	1.66E-6	4.45E-7	-0.24	2.65E-2
BSNSB	8.03E-7	4.14E-8	-0.22	5.06E-2
BGNSH	1.20E-6	6.54E-7	-0.22	5.25E-2
BGNSW	1.44E-6	6.36E-7	-0.19	1.50E-2
BGSA	1.69E-6	4.65E-7	-0.22	9.57E-3
BGSB	1.05E-6	3.9E-7	-0.22	9.57E-3
BGSH	2.08E-6	3.11E-7	-0.22	1.83E-2
BGSW	1.77E-6	8.99E-7	-0.20	3.40E-17
NBNSA	1.59E-6	6.74E-7	-0.25	4.99E-2
NBNSB	7.86E-7	2.45E-7	-0.21	7.77E-2
NBNSH	1.38E-6	5.13E-7	-0.27	5.72E-2
NBNSW	1.73E-6	8.46E-7	-0.20	2.45E-2
NBSA	2.02E-6	8.77E-7	-0.24	2.22E-2
NBSB	8.72E-7	2.69E-7	-0.22	1.71E-2
NBSH	1.24E-6	3.54E-7	-0.24	4.80E-2
NBSW	1.68E-6	2.07E-7	-0.18	2.08E-2

Overall it can be concluded that polarization of fresh samples in 3.4 wt% NaCl increase in current density towards the weld, but that all values fall in the same order of magnitude (-6). The overall current density generally is little different in value as the current density found in polarizing the weld material.

65

All samples from Table 18 were tested without cleaning or polishing. Commonly in electrochemical tests a clean uniform surface is tested. In this case however it was necessary to test the surfaces in the situation as close to the application as possible. To justify this decision also 2 pipe segments were tested with a cleaned and polished surface. Pipe segment Q3 (welded without bac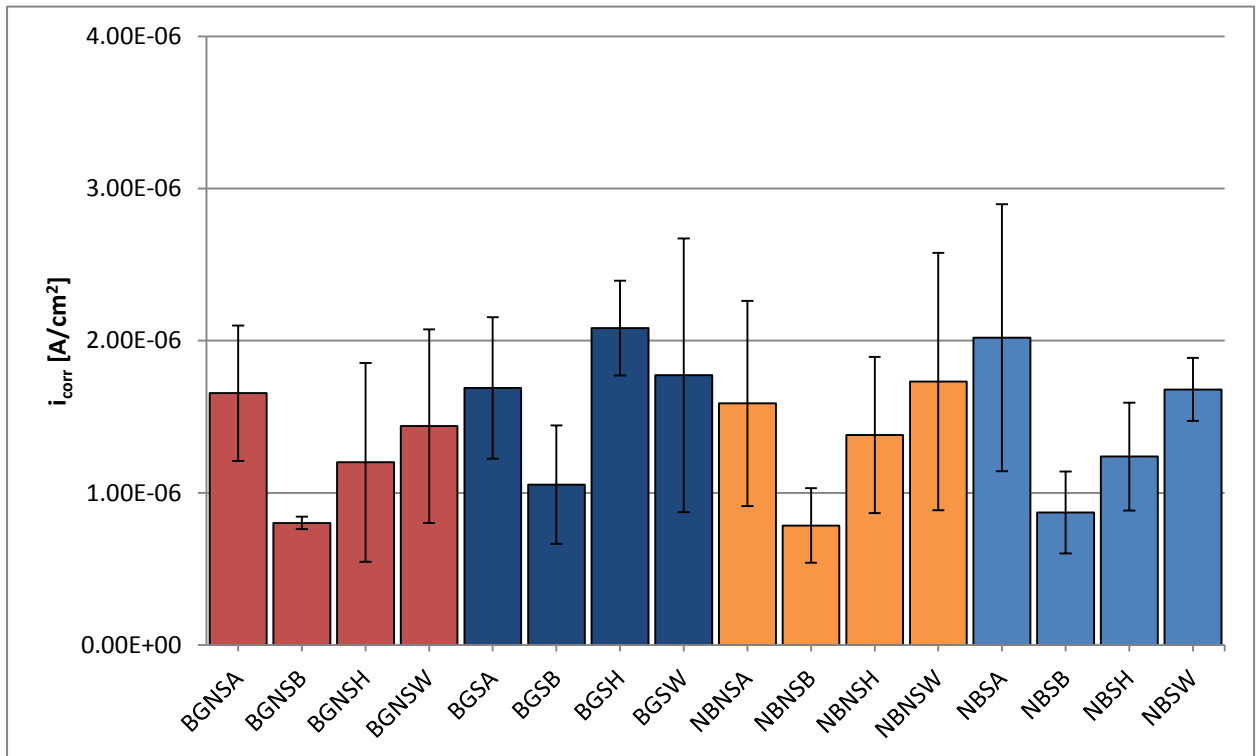king gas) and pipe segment S2 (welded with backing gas) were polished with Scotch-Brite and cleaned with ethanol before the cylinders for the polarization tests were attached. For each pipe segment base, HAZ, and weld zone tests were performed in the same manner as the tests with an unpolished surface. The results are shown in Table 19. The average i_{corr} for the three zones, base, HAZ, and weld, of the unpolished samples is $1.22*10^{-6}$ A/cm^2 ± 3.74E*10^{-7}. The average i_{corr} for the cleaned samples is $2.39*10^{-6}$ A/cm^2 ± 7.93*10^{-7}. The differences between the cleaned and uncleaned samples are shown in Figure 69 where the results are shown for each zone. BG and NBG again stand for backing gas and no backing gas respectively. The W following this stands for weld; the H for HAZ; and the B for base material.

Table 19: i_{corr} and E_{corr} results of the polished samples

Experiment	i_{corr} [A/cm2]	E_{corr} [V]
S.2.BASE	3.39E-6	-0.28
S.2.HAZ	1.82E-6	-0.32
S.2.WELD	2.66E-6	-0.20
Q.3.BASE	1.75E-6	-0.22
Q.3.HAZ	1.53E-6	-0.34
Q.3.WELD	3.16E-6	-0.23
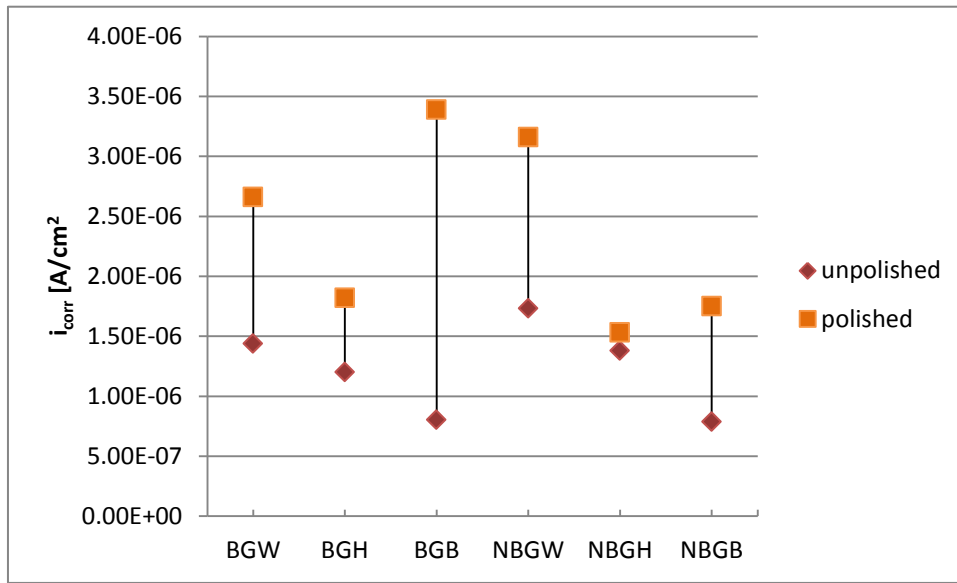
Figure 69: i$_{corr}$ values compared between unpolished samples and polished samples. The polished samples (orange) exhibited higher corrosion rates.

3.7 Electrochemical characterisation of CuNi10Fe samples in sulphide containing 3.4 wt% NaCl solution

Polarization curves were also made for all samples tested in sulphide containing 3.4 wt% NaCl solution. Representable polarization curves for each experiment are shown in Figure 70 to Figure 73. For clarity labels on the x and y axis are not shown. On the x axis the current density i$_{corr}$ is shown in [A/cm^2], on the y axis the potential is shown in [V] (versus SCE). Again two regions can be identified in the anodic part of the curve. The first region again shows the active dissolution of the metal. There is more variation found in the current densities of the samples compared to the samples in 3.4 wt% NaCl solution. Especially the curve for the weld zone without backing gas (orange line in Figure 71) shows the steady state current density to be greater than for the other curves. The second region shows the passive behaviour. Again this region appears around 0 V vs SCE (Epp). The shape of this region however is different with an increase in the current density for higher potentials. This is related to a less passive layer formed in sulphide containing solutions.
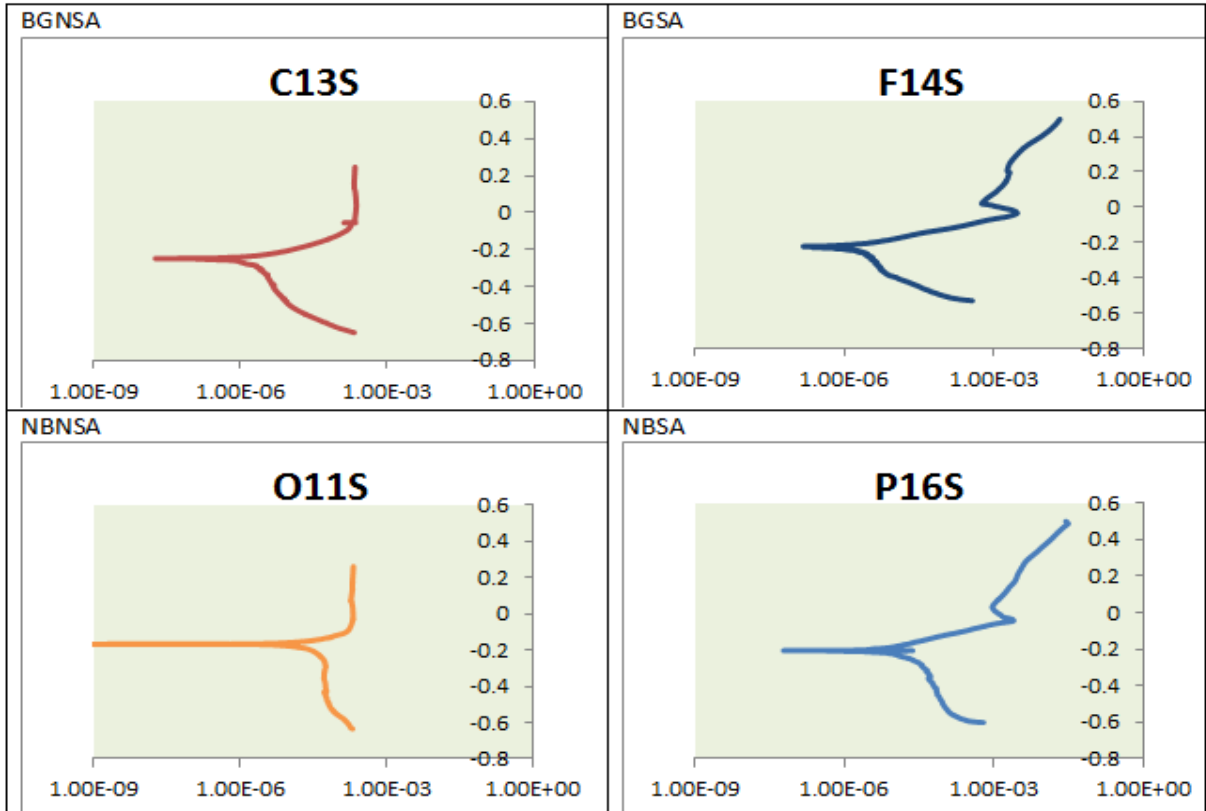
Figure 70: Whole region polarization curves for the four different experiments in sulphide containing 3.4 wt% NaCl. For each type of sample one representative curve is shown.
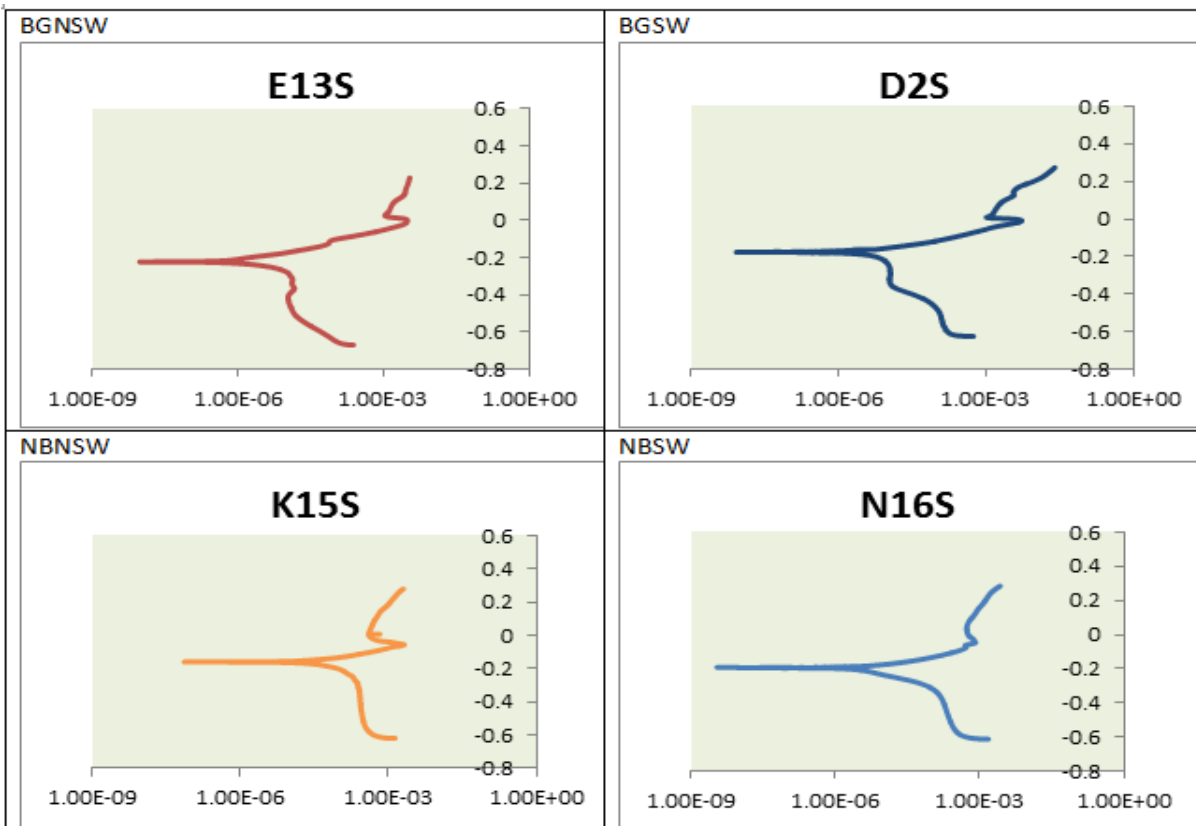
Figure 71: Weld zone polarization curves for the four different experiments in sulphide containing 3.4 wt% NaCl. For each type of sample one representative curve is shown.
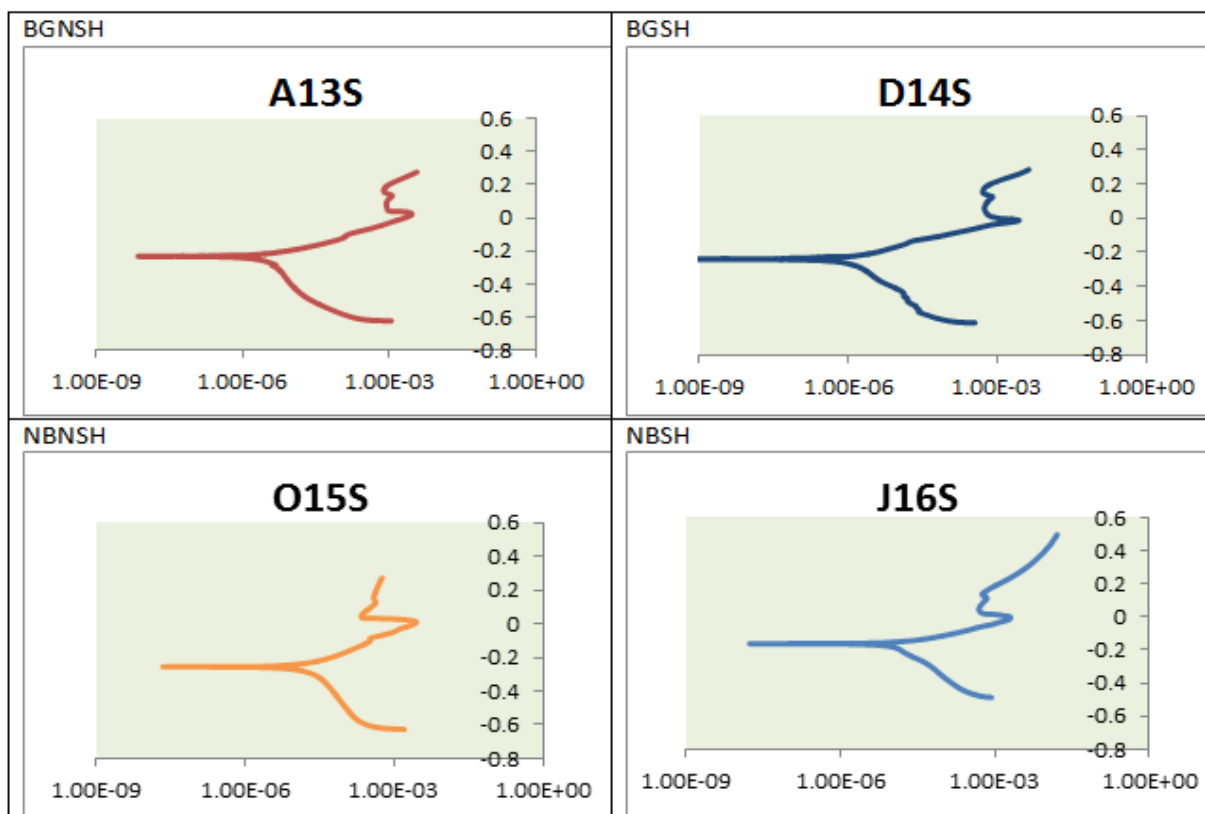
Figure 73: HAZ polarization curves for the four different experiments in sulphide containing 3.4 wt% NaCl. For each type of sample one representative curve is shown.
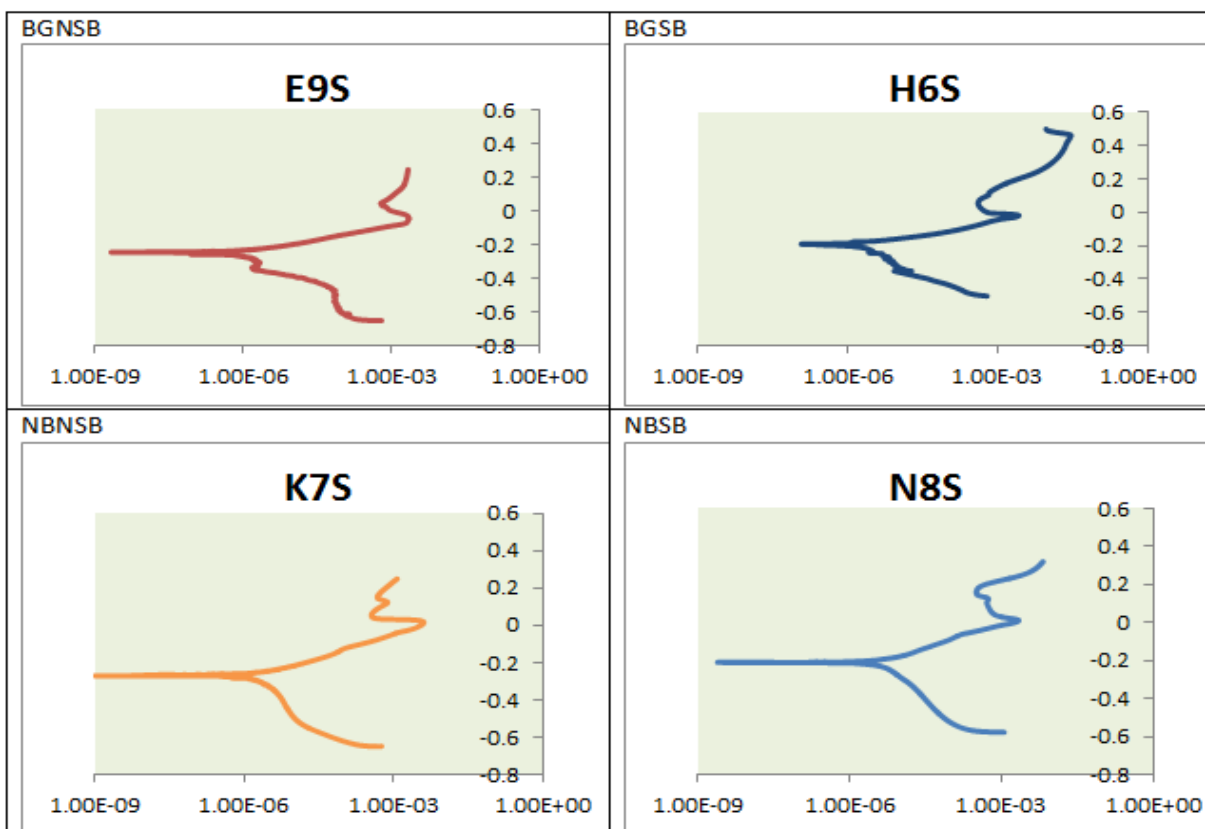
Figure 72: Base metal polarization curves for the four different experiments in sulphide containing 3.4 wt% NaCl. For each type of sample one representative curve is shown.

The results for the calculations of E_{corr} and i_{corr} in contaminated solution are shown in Figure 74 (E_{corr}) and Figure 75(i_{corr}).
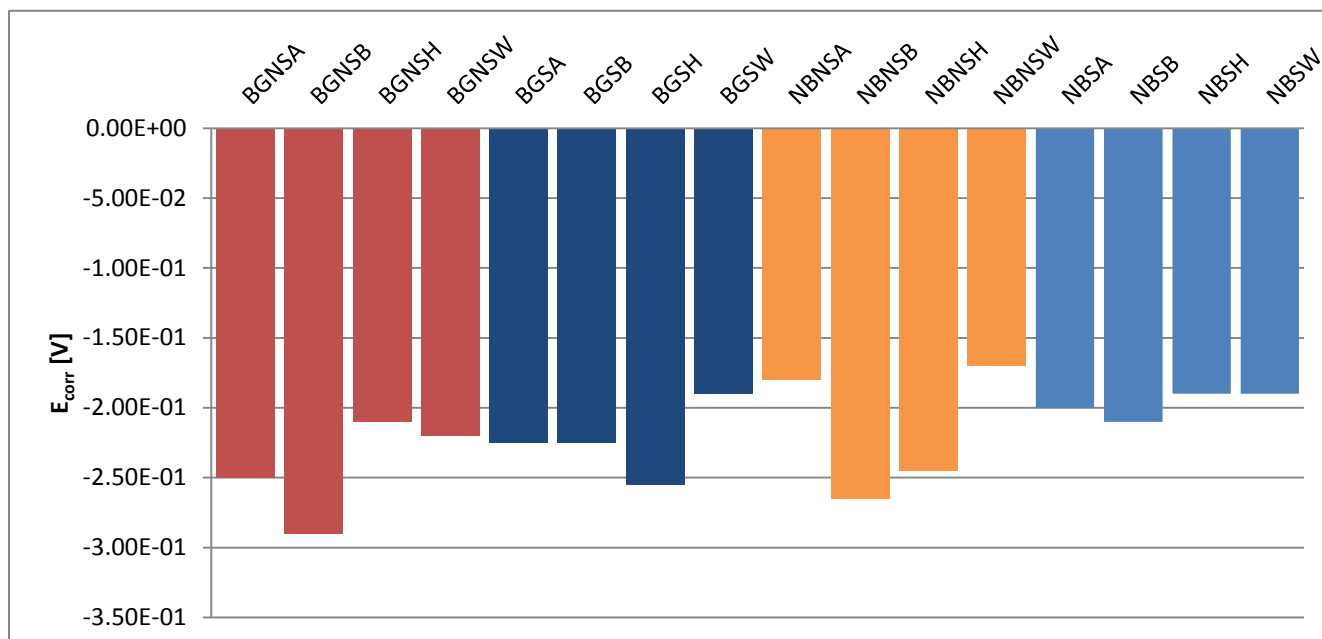
Figure 74: E_{corr} values per experiment type. The values are the average of four repetitions over different pipe segments. Again the differences are not significant.

The values are obtained in the same manner as described for the polarization tests before. E_{corr} values are measured between -0.17 and -0.29 V. For the i_{corr} values especially the samples welded without backing gas and without protection from a SDMC treatment show very high current density in the weld zone and HAZ. The samples with treatment (blue in the graphs) generally resulted in lower current densities compared to their non-protected counterparts (red and orange in the graphs). The standard deviations for these experiments were not calculated since there were two repetitions. From the previous experiments in electrolyte without sulphides it was already concluded that the standard deviations were not large. The same was observed in these experiments.
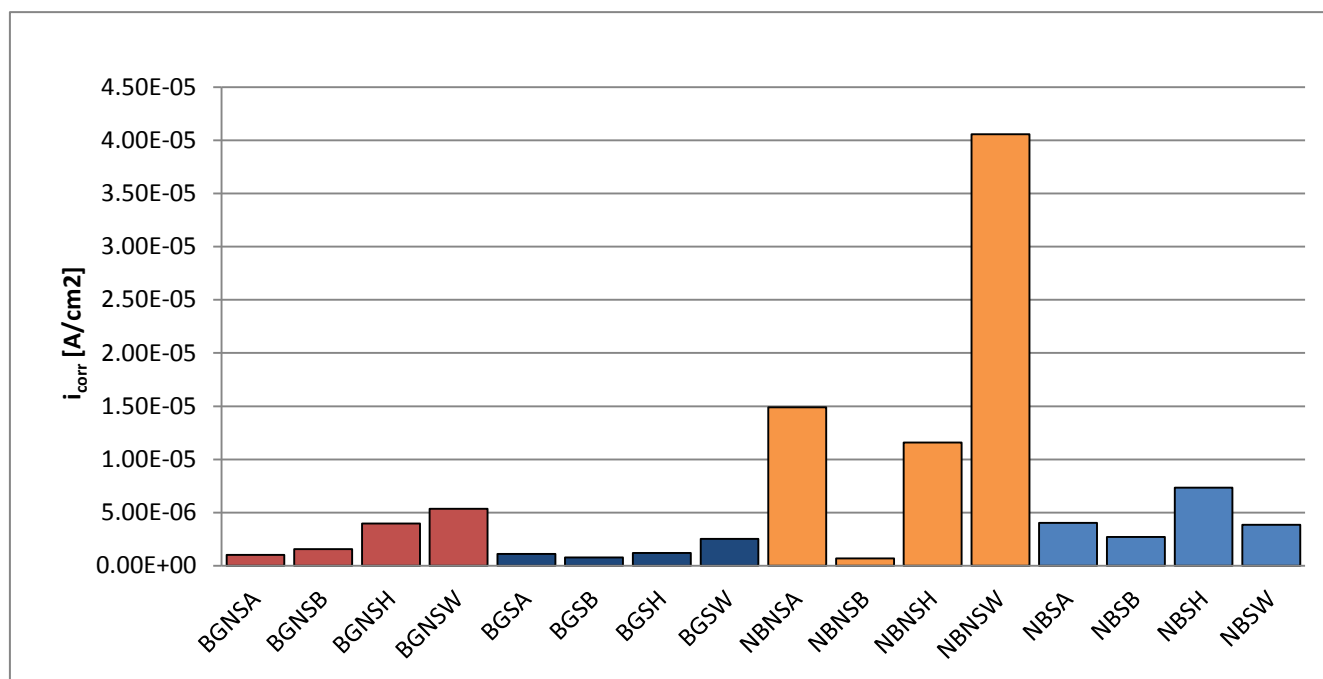
Figure 75: i_{corr} values per experiment type. The values are the average of four repetitions over different pipe segments. The highest current density is found for the sample welded without backing gas (orange). Protection of this sample with SDMC leads to lower current densities.

Table 20: numerical values of the average i_{corr} and E_{corr} values with the standard deviations obtained from the polarization curves

Experiment	i_{corr} [A/cm²]	E_{corr} [V]
BGNSA s	1.04E-6	-0.25
BSNSB s	2.54E-7	-0.29
BGNSH s	3.97E-6	-0.21
BGNSW s	4.54E-6	-0.22
BGSA s	1.11E-6	-0.23
BGSB s	8.94E-7	-0.23
BGSH s	5.44E-7	-0.26
BGSW s	2.52E-6	-0.19
NBNSA s	1.49E-5	-0.18
NBNSB s	7.11E-7	-0.27
NBNSH s	1.34E-5	-0.25
NBNSW s	4.06E-5	-0.17
NBSA s	4.05E-6	-0.20
NBSB s	2.72E-6	-0.21
NBSH s	6.65E-6	-0.19
NBSW s	3.87E-6	-0.19

The overall corrosion rates measured in the contaminated situation are much lower than measured over the weld. Another significant detail is the high current densities seen for the samples welded without backing gas and protection. For the heated base material and weld zone, as well as for the overall situation, the current densities are an order of magnitude larger than the current densities measured in the other samples.

With the results for both electrolytes Figure 76 was created in which the two results for the different zones are represented in one graph. In red the results for the sulphide containing 3.4 wt% NaCl tests can be seen, while in blue the results are shown for 3.4 wt% NaCl. The differences in corrosion rates can be so seen for each zone separately.
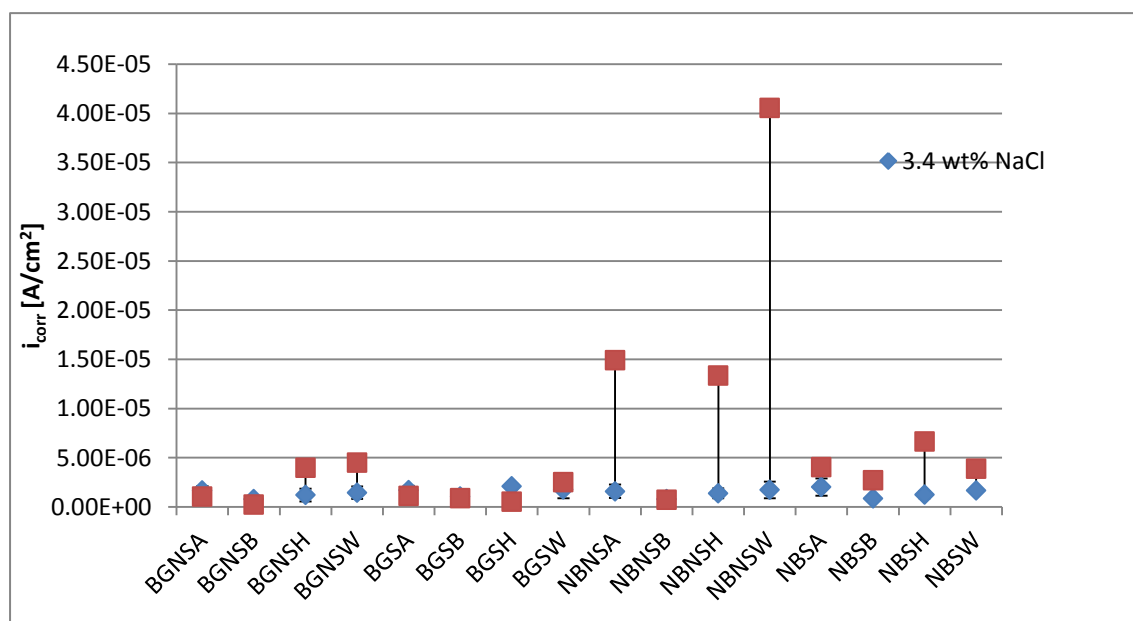
Figure 76: Comparison of the current densities found in 3.4 wt% NaCl and in sulphide containing 3.4 wt% NaCl.

Chapter 4: Discussion

4.1 Microstructural differences

The first detail of interest is whether there are differences in the microstructure over the different areas that can be identified. Differences in microstructure could lead to significant differences in corrosion properties. Research done by Schielab showed the average grain size as ASTM nr 6-7 for a CuNi10Fe piece of pipe (Schielab, 2012). This pipe came from the same manufacturer as the pipe tested now, with a similar composition (same werkstoff number). The average grain area found in this research was around 2000 μm^2. Comparing this to the ASTM standard grain sizes (ASTM, 2012) gives a similar ASTM number as the research done by Schielab. ASTM nr 6 is equal to an average grain area of 0.00202 mm^2 [2020 μm^2] while ASTM nr 7 equals an average grain area of 0.00101 mm^2 [1010 μm^2]. The grain areas found in the 6 sections therefore appears to be consistent and comparable to the material used in practice, with the exception of the grain sizes measured in the HB section. The frequency distribution plots show that the base and weld section of the sample with backing gas, as well as the base, weld, and heated base material sections of the sample welded without backing gas, have a similar distribution of grain areas with the majority of grains between 1 and 4800 μm^2. The distribution of the grains of the heated base material section welded with backing gas shows a distribution that is more spread out with larger grains being more present than in the other sections. The highest percentage consists however of grains with an area of 1-99 μm^2, just as in all the other sections.

One reason grain growth could occur is when sufficient heat is present. However for the sections researched here (pipe section Q and S) the heat input is 0.7 and 0.69 kJ/mm respectively. This difference is not large enough to explain the differences in grain area distribution between the heated base material of sections S (HB) and Q (NHB). Both however are on the higher end of heat input seen over all the pipes. But a higher heat input would have influenced also the grain area distribution in the other sections of the same pipe segment. The obvious difference found between the sections is welding with and without backing gas. However to be more precise it is recommended to investigate the grain areas in the heated base material further, preferably on cross sections from different samples.

The structure in the weld zone is very different. The structure that forms depends on the propagation speed of the solidification front (which is related to the travel speed of the torch) and the amount of alloying elements. In this case there are significant alloying elements, which would lead to a dendritic or cellular structure. For these welds a combination is seen with a cellular-dendritic structure.

The pores visible on the welds without backing gas are the result of oxidation, where oxygen and volatile element bubbles disturb the surface, leaving craters behind. These craters are the starting points of corrosion as shown by the immersion tests where green corrosion products started to appear in this region. The pores form secluded areas where ions can accumulate to increase corrosion. Cunifer alloys generally are resistant against pitting, but in the presence of sulphides higher corrosion rates are experienced, depending on the sulphide concentration. This concentration can increase due to the enclosement, leading to higher corrosion rates. Sulphide producing bacteria are normally removed due to the water velocity, but it is likely that in these pores bacteria may find a safe spot to reside and thereby further increase the sulphide concentration.

The border between the weld zone and these uniform crystals (the microstructural HAZ) is an area of interest, since here the grains transform from long dendrites to more rounded crystals. Especially in the standing tests with contaminated 3.4 wt% NaCl solution this area showed a shiny appearance,

indicating some corrosion activity. This zone was equal in microstructure on the samples welded with and without backing gas. However as could be seen visually in the samples welded without backing gas this was the area where the loosely adherent black layer was present. Beneath this layer already an orange coloured line can be seen just under and above the weld. On the sample welded with backing gas this line is less pronounced or absent (see *section 3.1*). After the standing tests the visual HAZ is covered with a different corrosion product structure than away from the weld. This can be seen in Figure 77 where an overview is showed of the weld and surrounding area of the sample welded without backing gas (unprotected with SDMC) after 28 days of immersion, and Figure 78 of the same sample, but this time under the microscope with 250x magnification. Again this is a stitched image to be able to make a larger area visible. The HAZ can be clearly identified on these images since there corrosion is not as profound as in other areas. As can be seen in Figure 79 also on the samples welded with backing gas a difference between the base material, weld material, and HAZ can be identified.

Figure 77: Detail of sample welded without backing gas after 28 days of immersion. On both sides of the weld the zones can be seen where the corrosion product is different.

Figure 78: Stitched image from the microscope (250x magnification). Same sample as above. Left the weld area, then the HAZ with the different corrosion product and right the heated base material.

Figure 79: Detail of sample welded with backing gas after 28 days of immersion. On the left side de weld (greyer area) can be seen. The HAZ in this case is darker green which completely covers the surface.

4.2 Compositional differences

Table 21: Summary of compositions from supplier certificates and EDS measurements as given before.

	Cu	Ni	Fe	Mn	C	Pb	Si	Ti	S	Zn	P	Zr
Pipe	86.98	10.29	1.61	0.80	0.0004	0.004			0.004	0.008	0.0033	0.01
EDS base	86.4	9.9	1.8	0.9	0.9							

The pipe used in this research had the composition tested by the manufacturer. The result of this test is summarized in Table 21. Since all pipe sections came from one pipe that was extruded the overall composition is showed in the table at *pipe.* The EDS results of the 10 points in a line gave a similar composition as given by the pipe certificate as can be seen in the table at *EDS base* were the results of point 1 are recaptured. A big difference can be seen in the carbon content. However it must be noted that EDS detection of lighter elements such as carbon can be difficult and prone to error. The K line of carbon is of a low energy, only carbon from the surface can be detected. As there is also noise that overlaps the small carbon peak the sensitivity to carbon is low (Rolland, Carlino, & Vane, 2004). Overall the SEM images show an equal intensity over the cross sections, indicating a consistent composition. Since the iron K line lies close to the K lines of nickel and copper small regions of iron precipitates cannot be detected with the used methods and settings. Research indicates however that below 2 wt% Fe no precipitates should form and following the compositions this is not reached in the sections.

However on top of the welds segregation of copper and nickel rich areas were found in the top 80 μm of the samples, similar as found in research on welds in cunifer alloys (Lee, Jacobus, & Little, 1991) (Savage, Nippes, & Miller, 1976). As discussed before this can lead to a loosely adherent Cu_2O layer which can break off easily in flowing water. When this protective layer breaks off the metal underneath is freshly exposed and will start to corrode again with corrosion rates equal to those for fresh surface cunifer. The Cu_2O layer is usually protected against erosion and dissolution by a corrosion layer formed on top of the Cu_2O layer. This overlying layer can consists of different complex copper-containing oxides, depending on the solution present. It is expected that this layer, if sufficiently thick over the weld area, will protect the parts of Cu_2O at the nickel rich area from erosion.

4.3 Surface potential differences

 From the SKP graphs it is clear that welding without backing gas has an influence on the surface potential. The sample welded with backing gas, not protected with SDMC shows a more or less constant potential, this weld was well protected with shielding gas to prevent high temperature oxidation. The weld without backing gas exhibits a more varying potential over the weld and visual HAZ. Away from the weld this sample reaches the same potential as the other samples. The weld without backing gas can be expected to have experienced oxidation; the loose black layer is a sign of burned residues. Oxidation as a result of welding in stainless steels also leads to an increase in potentials measured by SKP (Bäck, Nazarov, & Thierry, 2005). The change in potential depended there on the thickness of the oxidation layer, where an increase in thickness leads to a higher potential. A similar mechanism can be expected here with the higher potential values varying over the area around the weld. The thickness of the oxide layer is usually depended on the temperature gradient, which is decreasing away from the weld.

Differences can also be seen between the treated and untreated samples. The SDMC treatment for the sample with backing gas led to higher potentials, with more variation in the visual HAZ. Since the SDMC is a self-assembling layer this could be explained by differences in thickness of the layer and orientation of the molecules. Also for the sample welded without backing gas the treatment alters the potential, where the steady state value is reached closer to the weld than for the non-treated sample. The current densities in sulphide containing water are for the HAZ higher than for the weld zone, something not seen for the sample welded with backing gas. An explanation can be found in the oxides that form when welding without backing gas; the visual HAZ was heated high enough for different oxides to form and this could hinder the effectiveness of the treatment. This is indicated by the SKP results which are higher for the treated sample welded without backing gas than for the treated sample welded with backing gas.

Visually there are differences seen with the loosely adherent black layer and the porosity in the weld. The visual HAZ extends to about 45 mm away from the centre of the weld. The biggest changes in the SKP values are present in this region for the welds, most notably for the NBS sample. Here a sudden drop to the stable work function value occurs at 48 mm from the centre of the weld. This sample is treated with SDMC. A similar decline is seen for sample BS, also protected by SDMC. The values of the work function are higher in de first 50 mm after the weld than for the sample not protected by SDMC (B). This behaviour suggests that the treatment protects different in the visual HAZ than on the base material. The visual HAZ has different surface characteristics which can alter the method of which the SDMC assembles itself on the surface.

The differences found in the work functions of the samples are especially important since there are no such differences found in the microstructure to explain corrosion differences. The SKP measurements focusses on the surface, any differences in this surface, such as a discoloration of the surface or a treatment, alter the work function. If the surface is thus altered, for example by polishing or grinding the surface layer, the work function also alters, and the research no longer matches the practical situation. It was therefore important not to polish the surface, which would be normal procedure for the polarization tests, but to test the samples in the surface condition as they would be in practice.

These differences show the importance of the surface layer in regard to the corrosion properties and the differences between the zones.

4.4 Corrosion behaviour differences

The polarization tests indicate differences in corrosion rate between the different regions. The polarization curve shows the corrosion behaviour occurring during the polarization. The polarization curves in 3.4 wt% NaCl solution overall exhibit a better passive layer than the samples tested in sulphide containing 3.4 wt% NaCl solution. This can be seen in the region above Epp where for the samples in 3.4 wt% NaCl the current density does not increase as much as for the samples in sulphide containing 3.4 wt% NaCl. This relates to the idea found commonly in literature that the sulphides hinder the formation of a truly protective Cu_2O layer (Schrader, 1982) (Syrret, 1981).

Polarization of the samples did not result in crevice corrosion or pits. Both were also not observed in the standing tests. The calculated current densities show some interesting trends. For the samples tested in 3.4 wt% NaCl it is evident that testing only on the base material leads to the lowest current density. For most samples the heated base material has higher current density while the weld material exhibits the highest current density. An exception is seen for the samples welded with backing gas and SDMC protection, where the highest current density is found for the heated base material. However the weld zone for this sample has a larger variance. Research in standing, quiet water showed that CuNi30Fe exhibits higher current rates than CuNi10Fe. This is thus consistent with this research where the weld material is CuNi30Fe and the base material CuNi10Fe (Powell & Michels, 2000).

The weld area exhibits the largest current density, which can be explained by the rough surface due to welding without backing gas. Here a lot of pores show and as could be seen in the standing tests this area starts almost immediately to show signs of corrosion attack. The pores are also good at containing the corrosion products, such that corrosion can increase. Other research focussed on the influence of sulphides on the corrosion properties of CuNi10Fe and CuNi30Fe (Al-Haji & Reda, 1993). Similar as in the present study an increased corrosion rate was found in the presence of dissolved sulphides. An increase in the concentration of sulphides led to an increase in the corrosion rates and it was concluded that the sulphide acts as a catalyst.

Martinez and Metikos-Hukovic stated that they found a shift in the steady-state corrosion potential of about 30 mV between unprotected and protected CuNi10 (Martinez & Metikos-Hukovic, 2006). The researchers created CuNi10 from pure copper and nickel constituents, polished the samples and then covered half of them with SDMC. This shift of corrosion potential was not found in this research, where no trends where noticed in the variation of the steady-state corrosion potential. Research by Aljinovic et al. on commercial grade CuNi10Fe with SDMC protection showed also no shift in steady-state corrosion potential when polarization tests were done in seawater (Aljinovic, Gudic, & Smith, 2000). Corrosion rates found in literature were of the same order of magnitude as found for the base metal in 3.4 wt% NaCl tested in this study. The shift in the E_{corr} values appears to be dependent on the circumstances wherein the polarization test has been performed and the composition of the metal.

The electrochemical polarization results tell something about the protection mechanism of the SDMC treatment. As can be seen in section *3.4 Electrochemical characterisation of the CuNi10Fe samples* the E_{corr} values for protected and unprotected samples show no significant differences. This indicates that protection does not work by changing the potential of the reaction, but more likely prevents corrosion by limiting access to the metal surface. The result is that i_{corr} of samples protected by SDMC are lower, most notably in the sulphide containing 3.4wt% NaCl solution.

The overall corrosion rate for freshly exposed surfaces was calculated according to Faraday's law as explained in section *2.6 Electrochemical polarization tests.* In this case the calculation has been done for the tests on all three zones at once, since this is the closest approximation for the whole pipe system. The results of the tests in 3.4 wt% NaCl are shown in Table 22. It is decided to give the results for the mean plus/minus two times the standard deviation. Herein 95% of possible outcomes of the tests should fall. The calculated corrosion rates of the samples tested in 3.4 wt% NaCl with sulphides are shown in Table 23. In this case only two repetitions were made, so no reliable standard deviation could be calculated. Therefore here the corrosion rate of the mean value is given. For calculation one electron is expected to take part in the process.

$$r[\frac{cm}{y}] = \frac{ia}{nF} = \frac{i\left[\frac{A}{cm^2}\right] * 7.1\left[\frac{cm^3}{mol}\right]}{1 * 96500\left[\frac{C}{mol}\right]}$$

Table 22: corrosion rates calculated for the experiments over base, heated base and weld metal together in 3.4 wt% NaCl

Experiment	i_{corr} [A/cm²]	r [mm/year]	Life expectancy 2 mm thick pipe [yr]
BGNSA	7.70E-7 - 2.55E-6	1.78E-2 - 5.91E-2	34-112
BGSA	7.60E-7 - 2.62E-6	1.76E-2 - 6.07E-2	33-114
NBNSA	2.42E-7 - 2.94E-6	5.61E-3 - 6.81E-2	29-366
NBSA	2.66E-7 - 3.77E-6	6.17E-3 - 8.75E-2	23-324

Table 23: corrosion rates calculated for the experiments over base, heated base and weld metal together in sulphide containing 3.4 wt% NaCl

Experiment	i_{corr} [A/cm^2]	r [mm/year]	Life expectancy 2 mm thick pipe [yr]
BGNSA s	1.04E-6	2.41E-2	82
BGSA s	1.11E-6	2.58E-2	77
NBNSA s	1.49E-5	34.6E-2	5
NBSA s	4.05E-6	9.40E-2	21

A review of research on CuNi10Fe listed values of 0.01-0.24 mm per year (Kear, Barker, Stokes, & Walsh, 2004). The corrosion rates thus found correspond with the corrosion rates found in literature. To calculate the expected lifespan a wall thickness of 2 mm was considered. The pipe is expected to be at the end of its life when the wall thickness is reduced to 1 mm in this calculation. The found life expectancies are shown in the tables. This calculated life expectancy however should not be taken for granted. During the lifespan of the system different situations can occur that influence the corrosion rate. In the case without sulphides a protective corrosion layer forms that will lower the current density and therefore the corrosion rate. With sulphides this will most likely not be the case. Other influences are the flow velocity as well as changes in sulphide concentrations and temperature depending on the whereabouts of the vessel.

It is also possible to calculate the worst case scenarios, thus for the situations where the highest current density is found. For the case in 3.4 wt% NaCl the overall reactions display the highest corrosion rates, the highest is found in the case of welded without backing gas, protected by SDMC which could show a corrosion rate of 3.77 *10^{-6} A/cm^2 (median plus two times the standard deviation, wherein 95% of samples should fall). This is different in the case of sulphide containing 3.4 wt% NaCl, where the highest current densities were not found for the overall reactions, but instead for the weld zones. Especially the weld zones of the samples welded without backing gas are of interest. Here the average current density found was 4.06*10^{-5} A/cm^2 which gives a life expectancy of only 2 years in sulphide containing water. During build-up the vessel can be present in sulphide containing water for 1.5 years or longer. It is therefore advised to avoid welding without backing gas, and to protect the cunifer alloy with a SDMC treatment.

The corrosion rates tested with this method are approximations for a situation where no protective oxidation layer has yet formed on the CuNi10Fe and the CuNi10Fe is present in a standing solution. In practice the CuNi10Fe will be subjected to a flow of seawater. Flow will increase the corrosion rate, and above a critical flow velocity the corrosion product will be physically removed as concluded by Efird and Anderson (1975), reproduced by Francis (Francis, Corrosion of Copper and its Alloys - A practical guide for Engineers, 2010). The SDMC protected samples will also corrode faster when under the influence of fluid flow (Martinez & Metikos-Hukovic, 2006). This will thus destroy the protective layer and increase the corrosion rate. Another contributing factor that could lead to accelerated attack is the dissolution of the protective layer because of the continuous supply of chloride ions (Kear, Barker, Stokes, & Walsh, 2004). The chloride ions react with the cuprous oxide to become soluble $CuCl_2^-$. In a fully developed film the cuprous oxide film is protected by copper oxides that are more difficult to dissolve. If this layer is stripped away by the fluid flow the underlying cuprous oxide layer is subject to solubility. Design limits for CuNi10Fe are usually set at 3.5 m/s for systems with continuous flow.

Another important difference between the tests and the practical situation is the electrolyte. In the test a 3.4 wt% NaCl solution is used instead of natural seawater. Large differences exist between corrosion in seawater and in artificial solutions (Parvizi, Aladjem, & Castle, 1988). Seawater consists

of a combination of a large number of salts and other constituents including biological compounds. Differences in corrosion products formed can already be found between tests with natural seawater in practice and with natural seawater in a laboratory. Seawater can be more aggressive than 3.4 wt% NaCl, so this should be taken into account when predicting a life expectancy from results of this research. Since there are many differences in seawater itself (location and depth influence the composition) it was decided to use 3.4 wt% NaCl as solution to compare the results with each other. Therefore the corrosion rate should not be taken for granted, but the relative differences between the experiments and the specific influence of sulphide contamination are of importance here.

The corrosion products commonly formed are first a layer of Cu_2O with then the formation of $Cu_2Cl(OH)_3$. Other copper corrosion products can be formed, depending on temperature and electrolyte composition, but the protective layer of Cu_2O is found in many researches. Cu_2O forms a reddish/brown layer, similar to CuNi10Fe normal appearance. $Cu_2Cl(OH)_3$ appears green and can form a thick layer. The corrosion layer protects the surface by inhibiting the cathodic process (reduction of oxygen) by preventing the electrons to reach the solid/liquid interface (Francis, Corrosion of Copper and its Alloys - A practical guide for Engineers, 2010). The oxide layer formed in the standing test with (contaminated) 3.4 wt% NaCl is of similar colour as $Cu_2Cl(OH)_3$ found elsewhere (Krougman & Ijsseling, 1976). Under de microscope an open structure can be seen as shown in Figure 81. The orange spots found in the samples with SDMC protection exhibit a similar structure, only the colour is different as can be seen in Figure 80.
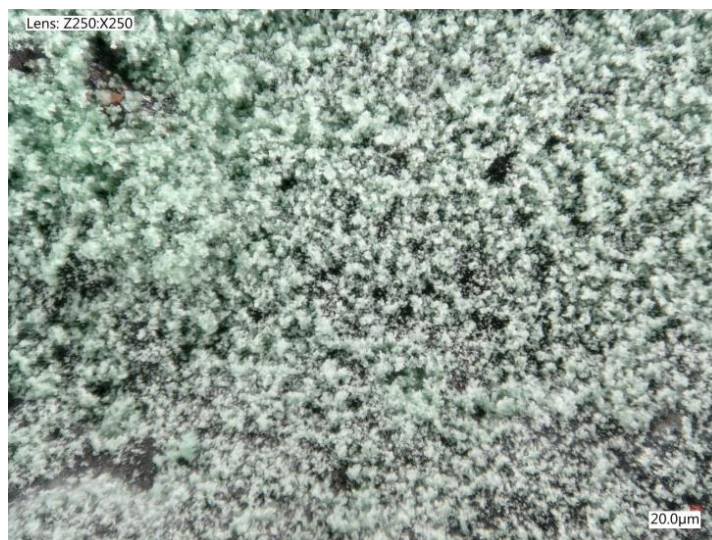
Figure 81: Corrosion layer after 28 days of immersion. Similar for all samples in 3.4 wt% NaCl. The porous structure resembles $Cu_2Cl(OH)_3$ strongly.

Figure 80: Corrosion layer after 28 days of immersion. Orange spots as observed on SDMC protected samples.

4.5 General discussion

Corrosion rate differences were found between the different zones (weld, HAZ, and base material). The differences are found in the immersion tests where visually different corrosion products formed as well as in the polarization tests where differences could be seen in the current densities. From this study it was found that large differences in microstructure are not seen over the HAZ and the base material. The structure of the weld area is also similar for the weld with and without backing gas; both reveal a columnar-dendritic structure with micro-segregation. The grain areas found are similar as found in earlier research. On the inside of the pipe in the weld area (backside of the weld) macro segregation was seen with the EDS. This macro segregation influences the corrosion properties over time since the protective corrosion layer adheres not as well on the nickel rich areas in the segregation area. Since the microstructure does not explain the differences in current densities found over the different zones in the electrochemical polarization tests another aspect was researched. Via SKP the influence of the surface condition was determined. These measurements showed differences in surface potential between the different samples, as well as over the surface of the samples itself. The region with visual HAZ (discoloration) showed higher surface potentials than the region of the base material. Since the samples all come to the same surface potential away from the weld, it can be concluded that the welding procedure influences the surface condition and thereby influences the corrosion properties. Another corrosion influence on the surface, present only for the welds welded without backing gas, is the rough surface at the weld root. Sulphide creating bacteria will not be flushed away from these pores but can multiply and produce more sulphide. This can result in high corrosion rates locally.

The influence of sulphides in the solution was most notable for the samples welded without backing gas. However in the immersion tests all samples showed visual signs of corrosion activities earlier in the sulphide containing solution. Sulphides increase the corrosion rate and hinder the formation of a stable passive layer. This could be seen also in the polarization curves where above the passivation potential the current density often increased instead of remaining constant. The protection layer of SDMC reduced the current density in sulphide containing solution significantly, indicating it provides protection by limiting the access to the metal surface.

Conclusions

In this section the results presented before are discussed. The research focusses on the question whether there are differences in corrosion resistance when CuNi10Fe is welded without backing gas or welded with backing gas. Besides this difference also the protection used (SDMC treatment) is of interest in relation to the corrosion properties. The results show that current density increases significantly when CuNi10Fe is welded without backing gas, especially in the weld zone itself. In the presence of sulphide contamination the SDMC treatment decreases the current density, thereby increasing the lifespan of the pipe system.

Corrosion products start to appear in the crevices formed due to oxidation while welding without backing gas. These crevices or pores are also safe havens for sulphide creating bacteria. Sulphide increases the corrosion rates. Therefore welding without backing gas should be avoided because of the increased corrosion rate.

The protective layer formed in 3.4 wt% NaCl solution consists most likely of Cu_2O, the same layer also forms in natural seawater and offers protection by limiting the electrons to diffuse out. In natural seawater this layer grows and increases in protection for about 3 months. This layer is less protective when sulphides are present, leading to higher current densities which will also be present longer since there is no passive layer growing.

Cunifer alloys can be treated with sodium diethyldithiocarbamate. This treatment forms a monolayer on the cunifer alloy that protects against corrosion by restricting access to the metal surface. This layer is vulnerable and easily removed but the tests show that in the case of sulphide polluted water the treatment reduces the corrosion rates and thereby protects the metal.

Differences in current densities are mainly a result of composition and surface condition and less dependent on microstructure. It was shown that altering the surface condition by polishing changed the current density and therefore could not be used to mimic the practical situation. Electrochemical polarization tests should therefore be performed without polishing or cleaning the surface.

Recommendations

To determine the exact composition of the corrosion layer more research is needed. But as explained the corrosion layers can vary widely when formed in natural seawater or in 3.4 wt% NaCl. Therefore in this research no further investigation has been undertaken to determine the corrosion product composition. It would be beneficial to determine the corrosion products in the real situation, including their protection influences in flowing seawater.

Micro segregation was observed in the weld area. The dendrites that solidify push out the alloying elements to the insides. This difference in composition could also lead to differences in the corrosion properties. With electrochemical microcapillary technique and atomic SKP this could be further investigated, since the techniques used in the present study provide only corrosion data over a relatively large area.

Macro segregation was seen in the weld root. It is known that this influences the adhesion of the corrosion layer to the metal surface. However further investigations are needed to explain how these macro segregations occur and their specific influence on the corrosion behaviour.

The welds without backing gas sometimes showed bad penetration. This resulted in a crevice between the two pipe segments were no weld filler was present. Crevices can influence the corrosion behaviour, similar as the irregularities on the weld surface as seen in this research. This influence was not noted in this research, but further research noting this specific property of welding without backing gas is needed.

Iron present in up to 2 wt% usually is in solid solution. Higher weight percentages could lead to precipitation of the iron, just as added heat could have the same result. Iron precipitates have a negative influence on the corrosion properties (Popplewell, Hart, & Ford, 1973). Since welding consists of adding heat to the material precipitation could occur when enough iron is present in the alloy. Precipitates are unlikely to form in this case since the expected amount of iron should not exceed 2 wt%. In the immersion tests also no indication was found of iron precipitates corroding. The expected size of the iron precipitates is very small, and none were found in the SEM investigation of the weld areas. With EDS the iron precipitates are difficult to detect since the peak of iron lies close and overlaps partly the peak of copper. Further research may be required if the question should arise whether the iron precipitates are present. This could include measuring a change in magnetic susceptibility, which occurs when iron precipitates have formed.

Works Cited

Agarwal, D., & Bapat, A. (2009). Effect of Ammonia and Sulphide Environment on 90/10 and 70/30 Cupronickel Alloy. *Journal of Failure Analysis and Prevention, 9*, 444-460.

Al-Haji, J., & Reda, M. (1993). The corrosion of copper-nickel alloys in sulfide-polluted seawater: the effect of sulfide concentration. *Corrosion Science, 34*, 163-177.

Aljinovic, L., Gudic, S., & Smith, M. (2000). Inhibition of CuNi10Fe corrosion in seawater by sodium-diethyl-dithiocarbamate: an electrochemical and analytical study. *Journal of Applied Electrochemistry, 30*, 973-979.

Ashby, M., Shercliff, H., & Cebon, D. (2014). *Materials - engineering, science, processing and design.* Elsevier .

ASM International. (2004). Volume 9, Metallography and Microstructures. In A. International, *ASM Handbooks.*

ASTM. (2000). *Annual book of ASTM standards* (Vol. 03.01). American Society for Testing and Materials.

ASTM. (2012). *E112-12 Standard Test Methods for Determining Average Grain Size.* ASTM International.

Bäck, G., Nazarov, A., & Thierry, D. (2005). Localized corrosion of heat-treated and welded stainless steel studied using a scanning kelvin probe. *Corrosion, 61*, 951-960.

Bekkers, B. (2009). *WLSN 101.* Welding Procedure Specification, Damen Schelde Naval Shipbuilding.

Bentiss, F., Jama, C., Mernari, B., Attari, H. E., Kadi, L. E., Lebrini, M., . . . Lagrenee, M. (2009). Corrosion control of mild steel using 3,5-bi(4-methoxyphenyl)-4-amino-1,2,4-triazole in normal hydrochloric acid medium. *Corrosion Science, 51*, 1628-1635.

Berg, P., Kievits, F., & Lange, R. d. (1968). Fundamental and technical studies on the corrosion behaviour of cunifer 10 alloys in seawater. *Proceeding of 2nd International Congress on Marine Corrosion and Fouling*, (pp. 95-105). Athens.

Beverskog, B., & Puigdomenech, I. (1998). *Pourbaix diagrams for the system copper-chlorine at 5-100 °C.* Nyköping: Swedish Nuclear Power Inspectorate.

Birks, N., Meijer, G., & Petit, F. (2006). *Introduction to the High Temperature Oxidation of Metals.* Cambridge University Press.

Copper Development Association. (1964). *Copper and Copper alloys selected microstructures and equilibrium diagrams.* C.D.A.

Copper Development Association. (1982). *Copper-Nickel Alloys, Properties and Applications.* TN30.

Davis, J. (2006). *Corrosion of Weldments.* ASM International.

Dawson, R. (1973). *Fusion Welding and Brazing of Copper and Copper Alloys.* The Butterworth Group.

Deutsches Kupferinstitut. (2005). *CuNi10Fe1Mn.* Werkstoff-Datenblätter.

Drach, A., Tsukrov, I., DeCew, J., Aufrecht, J., Grohbauer, A., & Hofmann, U. (2013). Field studies of corrosion behaviour of copper alloys in natural seawater. *Corrosion Science, 76*, 453-464.

Eiselstein, L., Syrett, B., Wing, S., & Caligiuri, R. (1983). The accelerated corrosion of Cu-Ni alloys in sulphide-polluted seawater: mechanism No. 2. *Corrosion Science, 23*, 223-239.

El Domaity, A., & Alhajji, J. (1997). The Susceptibility of 90Cu-10Ni Alloy to Stress Corrosion Cracking in Seawater Polluted by Sulfide Ions. *Journal of Materials Engineering and Performance, 6*, 534-544.

Evans, U. (1981). *An introduction to metallic corrosion.* Edward Arnold.

Francis, R. (1985). Effect of pollutants on corrosion of copper alloys in sea water. *British Corrosion Journal, 20*(4), 175-182.

Francis, R. (2010). *Corrosion of Copper and its Alloys - A practical guide for Engineers.* NACE International.

Gilbert, P. (1978). Copper alloys for offshore applications (Paper 4). *Copper alloys in the marine environment conference 8-9 february 1978.*

Giuliani, L., & Bombara, G. (1970). An electrochemical study of copper alloys in chloride solutions. *British Corrosion Journal, 5*, 179-183.

Gothelf, K. (2000). Self-assembled monolayers of long-chain xanthic acids on gold studied by voltammetry. *Journal of Electroanalytical Chemistry, 494*, 147-150.

Gudas, J. P., & Hack, H. (1979). Parametric Evaluation of Susceptibility of Cu-Ni Alloys to Sulfide Induced Corrosion in Sea Water. *Corrosion, 35*, 259-264.

Hodgkiess, T., & Vassiliou, G. (2005). Complexities in the erosion corrosion of copper-nickel alloys in saline water. *Desalination, 183*, 235-247.

Ismail, K., Fathi, A., & Badawy, W. (2006). Electrochemical behavior of copper-nickel alloys in acidic chloride solutions. *Corrosion Science, 48*, 1912-1925.

Jian, F., Wang, Z., Bai, Z., You, X., Fun, H., Chinnakali, K., & Razak, I. (1999). The crystal structure, equilibrium and spectroscopic studies of bis(dialkydithiocarbamate) copper(II) complexes [Cu2(R2dtc)4] (dtc=dithiocarbamate). *Polyhedron, 18*, 3401-3406.

Jones, D. (1995). *Principles and prevention of corrosion.* Prentice Hall.

Kato, C., Ateya, B., Castle, J., & Pickering, H. (1980). On the Mechanism of Corrosion of Cu-9.4Ni-1.7Fe Alloy in Air Saturated Aqueous NaCl solution I. Kinetic Investigations. *Electrochemical science and technology*, 1890-1896.

Kear, G., Barker, B., Stokes, K., & Walsh, F. (2004). Electrochemical corrosion behaviour of 90-10 Cu-Ni alloy in chloride-based electrolyte. *Journal of Applied Electrochemistry, 34*, 659-669.

KME Germany GmbH & Co. KG. (2010). *Inspection Certificate 3.1 acc. to DIN EN 10204 Analyse 26644.*

Krätschmer, A., Odnevall Wallinder, I., & Leygraf, C. (2002). The evolution of outdoor copper patina. *Corrosion Science, 44*, 425-450.

Krougman, J., & Ijsseling, F. (1976). The corrosion behaviour of CuNi10Fe in seawater. *Fourth International Congress on Marine Corrosion and Fouling* (pp. 297-312). Boulogne: Centre de Recherches et d'Etudes Oceanographiques.

Lathi, K., & Lukkari, J. (2002). Welding of copper-nickel alloys at Kvaerner Masa-Yards. *Svetsaren*, 9-10.

Lee, R., Jacobus, M., & Little, B. (1991). Compoition Variations in Copper-Nickel butt welds. *Corrosion*, 645-652.

Liao, Q., Yue, Z., Yang, D., Wang, Z., Li, Z., Ge, H., & Li, Y. (2011). Inhibition of copper corrosion in sodium chloride solution by the self-assembled monolayer of sodium diethyldithiocarbamate. *Corrosion Science, 53*, 1999-2005.

Little, B., Wagner, P., & Jacobus, J. (1988). The impact of sulfate-reducing bacteria on welded copper-nickel seawater piping systems. *Materials selection & Design*, 57-61.

Martinez, S., & Metikos-Hukovic, M. (2006). The inhibition of copper-nickel alloy corrosion under controlled hydrodynamic condition in seawater. *Journal of Applied Electrochemistry, 36*, 1311-1315.

Metikoš-Hukovic, M., Babic, R., & Škugor, I. G. (2011). Copper-nickel alloys modified with thin surface films: Corrosion behaviour in the presence of chloride ions. *Corrosion Science, 53*, 347-352.

Millero, F. (1986). The thermodynamics and kinetics of the hydrogen sulfide system in natural waters. *Marine Chemistry*, 121-147.

National Institutes of Health. (1997). ImageJ 1.48. Bethesda.

North, R., & Pryor, M. (1970). The influence of corrosion product structure on the corrosion rate of Cu-Ni alloys. *Corrosion Science, 10*, 297-311.

OHBA laboratory. (2014). *Structure 6*. Retrieved 12 19, 2014, from OHBA lab: http://www.geocities.jp/ohba_lab_ob_page/structure6.html

Ouden, G. d., & Hermans, M. (2009). *Welding technology.* VSSD.

Parvizi, M., Aladjem, A., & Castle, J. (1988). Behaviour of 90-10 cupronickel in sea water. *International Materials Reviews, 33*(4), 169-200.

Popplewell, J., Hart, R., & Ford, J. (1973). The effect of iron on the corrosion characteristics of 90-10 cupro nickel in quiescent 3.4%NaCl solution. *Corrosion Science, 13*, 295 to 309.

Powell, C., & Michels, H. (2000). Review of Seawater Corrosion Resistance and Antifouling. *00627.* Orlando, Florida: NACE.

Radaj, D. (1992). *Heat Effects of Welding.* Springer-Verlag.

Rohwerder, M., & Turcu, F. (2007). High-resolution Kelvin probe microscopy in corrosion science: Scanning Kelvin probe force microscopy (SKPFM) versus classical scanning Kelvin probe (SKP). *Electrochimica Acta, 53*, 290-299.

Rolland, P., Carlino, V., & Vane, R. (2004). Improved Carbon Analysis with Evactron Plasma Cleaning. *Microscopy and Microanalysis.* Savannah.

Rowlands, J. (1965). Corrosion of tube and pipe alloys due to polluted sea-water. *Journal of applied Chemistry*, 57-63.

Sanchez, S. d., & Schiffrin, D. (1982). The flow corrosion mechanism of copper base alloys in sea water in the presence of sulphide contamination. *Corrosion Science*, 585-607.

Savage, W., Nippes, E., & Miller, T. (1976). Microsegregation in 70Cu-30Ni weld metal. *Welding Journal*, 165-s-173-s.

Scheldestromen, W. (2012). *Analyserapport, monstercode: LZE-022152. Meetpunt Kanaal door Walcheren, brug Vlissingen.*

Schielab. (2012). *Onderzoek naar de aard van inwendige aantasting van een cunifer T-stuk.* Schielab BV.

Schleich, W., & Powell, C. (2007). CuNi 90/10: How to avoid typical failures of seawater tubing systems and marine biofouling on structures. In E. F. Publications, *Corrosion behaviour and protection of copper and aluiminium alloys in seawater* (pp. 73-94). Woodhead Publishing and Maney Publishing.

Schrader, M. (1982). Auger electron spectroscopic study of mechanism of sulfide-accelerated corrosion of copper-nickel alloy in seawater. *Appliciations of Surface Science, 10*, 431-445.

SIGMA-ALDRICH. (2015). *Hydrochloric acid*. Retrieved from SIGMA-ALDRICH company website: http://www.sigmaaldrich.com/catalog/product/sial/30721?lang=en&region=NL

SIGMA-ALDRICH. (2015). *Iron(III) chloride hexahydrate*. Retrieved 5 8, 2015, from SIGMA-ALDRICH company pages: http://www.sigmaaldrich.com/catalog/product/sial/f2877?lang=en&region=NL

SIGMA-ALDRICH. (2015). *Sodium metabisulfite*. Retrieved 5 8, 2015, from SIGMA-ALDRICH company site: http://www.sigmaaldrich.com/catalog/product/fluka/08982?lang=en&region=NL

Syrret, B. (1981). The mechanism of accelerated corrosion of copper-nickel alloys in sulphide polluted seawater. *Corrosion Science, 21*(3), 187-209.

Tuthill, A., Todd, B., & Oldfield, J. (1997). Experience with Copper Alloy Tubing, Waterboxes and Piping in MSF Desalination Plants. *Proceedings IDA World Congress on Desalination and Water Reuse*, *1*, p. Session 1 to 3. Madrid, Spain.

TWI global. (1991). *Defects/imperfections in welds - porosity.* Job Knowledge. Retrieved from http://www.twi-global.com/technical-knowledge/job-knowledge/defects-imperfections-in-welds-porosity-042/

TWI global. (n.d.). *Copper-nickel alloys Job Knowledge*. Retrieved 2 5, 2015, from TWI-global: http://www.twi-global.com/technical-knowledge/job-knowledge/copper-nickel-alloys-113/

TWI global. (n.d.). *Equipment for TIG Welding*. Retrieved 2 5, 2015, from TWI global: http://www.twi-global.com/technical-knowledge/job-knowledge/equipment-for-tungsten-inert-gas-tig-gta-welding-017/

UTP. (2010). *UTP A 387.* Regulation. Retrieved from http://www.bohlersoldabrasil.com.br/pesquisa/pt/pdf/separatas/UTP%20A%20387.pdf

VECOM. (2005). *Treatment and maintenance of cunifer Technical Bulletin 2005/05.* vecom-group.

Vetter, K. (1967). *Electrochemical kinetics.* Academic Press Inc. .

Voestalpine. (2013). *Inspection certificate 3.1.*

Voestalpine. (2014). *Inspection certificate 3.1.*

Voestapline. (2014). *Inspection certificate 3.1.*

Wallinder, I. O., Zhang, X., Goidanich, S., Le Bozec, N., Herting, G., & Leygraf, C. (2014). Corrosion and runoff rates of Cu and three Cu-alloys in marine environments with increasing chloride depostion rate. *Science of the Total Environment, 472*, 681-694.

Wang, Y., Beccaria, A., & G.Poggi. (1994). The effect of temperature on the corrosion behaviour of a 70/30 Cu-Ni commercial alloy in seawater. *Corrosion Science, 36*, 1277-1288.

Wood, R., Hutton, S., & Schiffrin, D. (1990). Mass transfer effects of non-cavitating seawater on the corrosion of Cu and 70Cu-30Ni. *Corrosion Science, 30*(12), 1177-1201.

Zarras, P., & Stenger-Smith, J. (2014). Chapter 3: Smart inorganic and organic pretreatment coatings for the inhibition of corrosion on metals/alloys. In A. Tiwari, L. Hihara, & J. Rawlins, *Intelligent Coatings for Corrosion Control* (pp. 59-91). Elsevier Inc.